Modeling and Simulation of Coupling Structures for Quasi-Optical Systems

by

Patrick Lascelles Heron

A thesis submitted to the Graduate Faculty of
North Carolina State University
in partial fulfillment of the
requirements for the Degree of
Doctor of Philosophy

Department of Electrical and Computer Engineering

Raleigh, NC

1993

Approved By:

Chairman of Advisory Committee	Co-Chairman of Advisory Committee
Committee Member	Mathematics Representative

Abstract

Heron, Patrick Lascelles

Modeling and Simulation of Coupling Structures for Quasi-Optical Systems.

Under the direction of Michael B. Steer and James W. Mink

Sponsored research was directed toward developing millimeter wave power sources utilizing quasi-optical techniques. A system consisting of an array of oscillators that radiated into a quasi-optical resonator was analyzed. Each oscillator was comprised of a solid state device and a radiating structure. A dyadic Green's function was developed for a Fabry-Perot resonator which consisted of a metallic planar reflector and a shallow spherical metallic reflector. The Green's function was applied to determine the driving point impedance matrix for an array of electrically small antennas within the resonator. An experimental X-band resonator was designed and fabricated, then one and two-port measurements were used to validate the theoretical calculations. A technique was determined for simulation of antennas that are not electrically small which radiate into the cavity. These techniques are shown to be applicable to coupling structures for quasi-optical systems in general.

Practical considerations regarding the simulation of nonlinear solid state driving elements were addressed. A a technique for efficient Jacobian calculation using the multidimensional fast Fourier transform as well as a technique for simulator time-domain oversampling were developed so that multiple oscillator systems can be efficiently simulated. These simulation techniques were implemented and tested in a harmonic balance circuit simulator.

I wish to dedicate this work to Karen. Without her patience, support, and sacrifice this work would not have been possible. I would like to thank Gregory Monahan for his assistance in design and construction of the experimental apparatus as well as for devising and applying the experimental measurement and de-embedding procedures. Gratitude is also due to Arthur Morris for his useful insights into electromagnetics and microwave systems. Finally, I wish to express my appreciation to the many largemouth bass who have waited patiently for this work to be completed.

Biographical Summary

Patrick L. Heron received the B.S.E.E. degree in 1983 from California State University Sacramento, the M.S.E.E. degree from University of Central Florida in 1987, and the Ph.D. in Electrical Engineering at North Carolina State University in 1993. From 1983 to 1987 he taught the Physics, Electrical Engineering, and Controls subjects at the United States Naval Nuclear Power School in Orlando, Florida. He is presently employed at Geophex Ltd. in Raleigh, NC. His research interests include, instrumentation and measurement, microwave and analog circuits, electromagnetics, and simulation of high speed circuits.

Table of Contents

List of Figures

List of Tables

List of Symbols

A_j - Coefficients for numerical integration.

$\mathbf{A}_M$ - Auxiliary potential function for magnetic source currents.

a - Aperture half width, circular patch radius .

a_e - Effective radius of circular patch antenna, includes effect of fringing fields.

$\mathbf{a}_{mn}$ - Vector coefficient for source field series expansion.

a_x - Rectangular aperture half width in the $\hat{\mathbf{a}}_\mathbf{x}$ direction.

a_y - Rectangular aperture half width in the $\hat{\mathbf{a}}_\mathbf{y}$ direction.

$\hat{\mathbf{a}}_x$, $\hat{\mathbf{a}}_y$, $\hat{\mathbf{a}}_z$ - Directional unit vectors for Cartesian coordinates.

b - Radius of curvature for spherical lens.

$\mathbf{b}_{st}$ - Vector coefficient of the returning test field.

C_D - Discontinuity capacitance for a coaxially fed inverted-L antenna.

C_T - Equivalent capacitance of an open circuited short transmission line.

c - Speed of light, Resonator numerical aperture parameter.

$\mathbf{c}_{st}$ - Vector coefficient of test field mode within the cavity.

c_x, c_y - Equivalent numerical apertures for strip resonators.

D - Resonator reflector spacing.

d - z-location of the plane containing source current.

$E^{\pm}_{p,mn}$ - $E^{\pm}_{mn}$ evaluated at the location of the p th antenna.

$\mathbf{E_S}$ - Resonant cavity vector electric field excited by a source current.

$\mathbf{E}_{T,st}$ - Vector electric modal test field.

$E^{\pm}_{mn}$ - Scalar electric field Hermite-Gaussian traveling wave beam with waist at $z = 0$ propagating in the $\pm\hat{\mathbf{a}}_\mathbf{z}$ direction.

e - Base of natural logarithm.

$F(X)$ - Solution to the resonator separated Huygen's equation.

$F_m(X_\ell)$ - Modal solution to the separated Huygen's equation evaluated at the point X_ℓ.

$\mathbf{F_m}$ - Vector of $F_m(X_\ell)$ each element evaluated at the X_ℓ th point.

F_x - Radius of curvature along the x direction for a spherical reflector .

F_y - Radius of curvature along the y direction for a spherical reflector .

f - Frequency in Hz.

$\mathbf{f}_{mn}$ - Vector coefficient for the source field series expansion.

$G(Y)$ - Solution to the separated Huygen's equation.

$G_n(Y_\ell)$ - Modal solution to the separated Huygen's. equation evaluated at the point Y_ℓ.

$\bar{\mathbf{G}}e_c$ - Complete cavity dyadic Green's function for electric source currents.

$\bar{\mathbf{G}}\mathbf{e}_h$ - Electric current dyadic Green's function for a half space bounded by a perfectly conducting plane.

$\bar{\mathbf{G}}e_r$ - Resonant cavity dyadic Green's function for electric source currents.

$\bar{\mathbf{G}}h_c$ - Complete cavity dyadic Green's function for magnetic source currents.

$\bar{\mathbf{G}}h_h$ - Magnetic current dyadic Green's function for a half space bounded by a perfectly conducting plane.

$\bar{\mathbf{G}}h_r$ - Resonant cavity dyadic Green's function for magnetic source currents.

$\mathbf{g}_{mn}$ - Vector coefficient for the source field series expansion.

$\mathbf{H}$ - Matrix representing sampled integral equation derived using Huygen's theorem applied to a resonator with two spherical reflectors.

$\mathrm{He}_m(X)$ - Hermite polynomial of order m and argument X.

$H^{\pm}_{mn}$ - Magnetic field Hermite-Gaussian traveling wave beam with waist at $z = 0$ propagating in the $\pm\hat{\mathbf{a}}_\mathbf{z}$ direction.

$\mathbf{H}_S$ - Resonant cavity vector magnetic field excited by a source current.

$\mathbf{H}_{T,st}$ - Vector magnetic test field.

h - Interval for numerical integration.

$J_m(x)$ - Bessel function of the first kind and order m.

$\mathbf{J}_q$ - Electric current distribution on the q th antenna.

$\mathbf{J}_S$ - Electric source current density within the resonator.

I_q - Terminal current for the q th antenna in an array.

$\bar{\mathbf{I}}_T$ - Unit transverse dyad.

K - Kernal for Huygen's integral in free space.

$\tilde{k}$ - Complex wave number.

k_0 - Free space wave number.

k_{mn} - Eigenfrequencies for a microstrip patch antenna.

L - Inductance.

$\mathbf{M}_S$ - Magnetic source current density within the resonator.

N - Fresnel number.

$\hat{\mathbf{n}}$ - Unit outward normal vector.

P^- - Power contained in a converging wavebeam.

P^+ - Power contained in a diverging wavebeam.

P_ℓ - Power lost from the resonator/patch antenna system.

Q - Quality factor of antenna or resonator.

q - Longitudinal mode number.

$\mathbf{R}$ - Vector from source point to field point.

R - Resistance.

$R_{0m}^{(1)}$ - Prolate spheroidal radial wave function.

R_{mn} - Reflection coefficient for wave beams having order mn.

R_p - Reflection coefficient for the planar reflector.

R_x - Radius of curvature along the x-axis.

R_y - Radius of curvature along the y-axis.

$\mathbf{r}'$ - Vector from origin of primed coordinate system to source location.

$\mathbf{r}$ - Vector from origin of unprimed coordinate system to field location.

S_1 - Infinite plane including the planar reflector.

S_2 - Infinite plane located at $z > D$.

S_{11}, S_{12} - Scattering parameters for a two port network.

S - Reflector surface on which the field is to be determined .

S' - Reflector surface which acts as a Huygen's source .

S_{0m} - Prolate spheroidal angular wave function.

T_{mn} - Transmission coefficient for wave beams having order mn.

t - Microstrip patch antenna height.

$U_e,\ U_m$ - Time average electric and magnetic energy.

$u(\mathbf{r}')$ - Huygen's' source strength on the reflector S'.

$v(\mathbf{r})$ - Huygen's source strength on the reflector S.

$w(X)$ - Inner product weight function.

w_0 - Gaussian beam radius at waist.

X - Scaled unitless x coordinate.

$\bar{X}$ - Gaussian mode parameter in the $\hat{\mathbf{a}}_\mathbf{x}$ direction.

Y - Scaled unitless y coordinate.

$\bar{Y}$ - Gaussian mode parameter in the $\hat{\mathbf{a}}_\mathbf{y}$ direction.

Z_0 - Reference or normalizing impedance.

$\mathbf{Z}$ - Impedance matrix for an array of small antennas within a resonator.

Z - Impedance.

z_{qp} - Impedance matrix term for an array of small antennas.

γ_{mn} - Single transit gain factor for a mode of transverse order m, n in a resonator with two spherical reflectors.

∇_t - Transverse coordinate Del operator.

Δf_q - Frequency spacing between the TEM_{mnq} mode and the $\text{TEM}_{mn(q+1)}$ mode.

ΔX_p - Effective length of the p th antenna.

δ - Kronecker delta function, Dirac delta distribution.

δ_{eff} - Microstrip patch antenna effective dielectric loss tangent.

ϵ_0 - Permittivity of free space.

ϵ_{eff} - Effective patch dielectric permittivity.

ε_{mn} - Traveling wave component of the source field.

η - Oblate spheroidal coordinate.

θ - Angle between $\hat{\mathbf{n}}$ and $\mathbf{R}$, oblate spheroidal coordinate.

λ - Free space wavelength.

λ_ϵ - Wavelength of a plane wave in a dielectric with permittivity ϵ.

μ_0 - Permeability of free space.

π - (circumference of a circle)/(diameter of a circle).

σ_d - Equivalent conductivity of a lossy dielectric.

Υ_{mn} - Ratio of outgoing to incoming wavebeam strength evaluated at $z = d$.

Φ - Scalar function describing fields under a microstrip patch antenna.

Φ_{mn} - Eigenfunctions for the microstrip patch cavity model.

ϕ - Oblate spheroidal coordinate.

χ_n - One pass transit gain for a mode of order n in an infinite strip resonator.

ψ_{st} - Ratio of intensity of outgoing to incoming wavebeams of mode st at the spherical reflector surface.

$\mathbf{\Omega}$ - Cavity volume.

ω - Radian frequency.

Chapter 1

Introduction

1.1 Motivation For and Objective Of This Study

At present, tube devices comprise the only practical sources for production of moderate to high levels of millimeter wave power [1]. These devices have several undesirable properties including; high cost, limited durability, high voltage power supply requirements, large size and weight. Oscillators employing solid state devices provide an alternative as sources for millimeter and submillimeter wave power and avoid many of the shortcomings of tubes. Due to the small size of solid state devices required for high frequency operation, a single device can produce only a very limited quantity of power. Power from numerous solid state oscillators must be combined to attain desired levels of power. An array of active devices along with auxiliary passive devices can be fabricated monolithically providing a high density of active devices at a modest cost.

A suitable method for the combining of power from the elements of the oscillator array must be determined. This method should be amenable to integrated circuit technology which will allow for a high density of oscillators and reduced system cost. Methods used at lower frequencies include waveguide or closed cavity combiners or microstrip hybrid combiners. At millimeter wave frequencies, combining power from a large number of sources inside a waveguide or cavity is impractical due to small waveguide transverse dimensions as well as the prohibitively large conductor losses. Closed cavities having dimensions significantly larger than a wavelength cannot be

used due to over–moding. Microstrip power combiners also suffer from high losses at and above millimeter wave frequencies. Optical techniques used at millimeter wave frequencies, termed quasi–optics, have been suggested for this application. Systems have been proposed in which the power from multiple solid state oscillators is combined in free space, phase locking is achieved through either direct radiation or by coupling though planar circuit structures. In an alternate approach, an open cavity type power combiner utilizes a quasi–optical resonator or *etalon* to accomplish the power combining. Open cavities have a much lower spectral mode density than closed cavities and do not suffer from side wall conductor losses.

A cavity type quasi–optical power combiner consists of an oscillator array with biasing circuitry, and two or more reflectors which comprise the cavity. The transverse dimensions can be much larger than a wavelength, thus permitting room for a large number of active devices. Over–moding does not occur because spectral mode density is not a function of frequency. If correctly designed, a source array will coherently oscillate when placed inside a quasi-optical cavity. Phase locking and power combination is achieved through field interactions involving the cavity mode structure. The resonant modes in such devices are orthogonal, so output power is maximized if single-mode operation is achieved. The design of an optimal source array is a formidable nonlinear problem. An array of antennae must be designed to properly couple into the cavity and each antenna must be impedance matched to its solid state source. The desired antenna parameters are a function of each antenna's location within the cavity and must include the effect of simultaneous oscillation of all other antennas. Coupling of each antenna into resonator modal fields, radiated fields, and non–modal reactive fields must be considered. The complexity of this system suggests that design should be accomplished using a simulation tool such as a harmonic balance oscillator analysis program. Simulation of this system places

some specific requirements upon the simulator capability.

There has been a significant amount of recent work on quasi–optical power combining of millimeter wave solid–state oscillators. Microstrip circuit type combiners can be analyzed and designed using existing planar circuit techniques. Free space combiners have been analyzed using antenna array and coupled oscillator theory. The absence of rigorous techniques for use in simulation and design of open cavity type power combiners is evident.

At present, much of the design of cavity-type quasi-optical power combiners has either been heuristic or has required highly simplified models. System performance using simplified design methods has been unsatisfactory, resulting in experimental combiners which demonstrate efficiencies an order of magnitude below theoretical predictions. The objective of this research is the development of simulation techniques that can be applied to the analysis and design of cavity type quasi-optical power combiners. The techniques must be sufficiently rigorous for optimal design of power combining systems. In this work, both model development and simulator development are considered. While this dissertation focuses specifically on cavity-type combiners, the techniques are applicable to the simpler free–space combiner if a simple half-space Green's function is used in place of the cavity Green's function. The results can also be applied to the study of antenna arrays which radiate into or extract energy from Gaussian optics systems. This provides a bridge to interface circuit theory with the theory of Gaussian optics. For example, antenna array coupling to Gaussian optical systems may offer an alternative to the expensive corrugated horn feed systems that are presently used [38].

1.2 Thesis Overview

Chapter 2 presents a review of the previous work done on quasi–optical power combiners. Various power combining techniques as well as analysis techniques are critically examined. The relative merits and shortcomings of the different combining techniques are discussed as well as the applicability of the analysis techniques which have been used to further power combiner design.

In chapter 3 a method is introduced and applied to determine a Green's function which relates a source electric current density to the cavity modal fields. Next additional terms are included in the Green's function which account for direct radiation and near-field effects. Derivation of an alternate Green's function for magnetic source currents is discussed.

In chapter 4, the theoretical work of chapter 3 is applied. The multiport impedance is derived for an antenna array radiating into a cavity. This predicted impedance is compared with two port measurements of small antennas radiating into an experimental X–band cavity. An iterative technique for simulating resonant sized antennas in the cavity is presented. Simulator requirements for power combiner design are introduced. This motivates the material found in the appendices.

Chapter 5 provides a brief summary of the dissertation, identifies areas where improvements can be made, and suggest possible directions for future work in this topic. Some general comments are made regarding resonator coupled power combiners.

Background for, and recent work in harmonic balance simulation techniques are presented in the appendices. The capabilities of harmonic balance techniques for simulation of quasi-optical power combiner systems are critically examined. Harmonic balance techniques are presented that provide for efficient simulation of res-

onant antennas in a cavity. The advantage of time domain oversampling and of multidimensional fast transform techniques are discussed. Methods for implementing these techniques are determined and simulator performance improvements are examined.

1.3 Original Contributions

The original contributions made by this dissertation are;

- A dyadic expression is derived for the Green's function of an open cavity. The method used by Mink [3] is extended for cases with arbitrary reflector spacing and excitation frequency. Coupling to nonresonant field components is included as well as diffraction and reflector losses. Diffraction losses are calculated by adapting the method of Soohoo [53] to a plano-bicylindrical resonator with rectangular apertures. Green's functions are determined for both electric and magnetic source currents [4], [5].

- The cavity Green's function is applied to determine an impedance matrix of an array of small antennas which radiate into a quasi-optical cavity. The results of this calculation are verified experimentally [4], [5].

- A method is devised for simulating resonant sized radiating structures within a quasi-optical resonator. Antennas or apertures which are not electrically small are simulated by using an iterative procedure in which the Q of the radiating structure is perturbed to account for power loss.

- A method is devised for the computation of the frequency domain analytic derivatives of a nonlinear device using the device time domain derivatives and

the multidimensional fast Fourier transform [71]. This method is necessary for efficient simulation when time domain models are used for multiple solid state oscillators located in a quasi–optical resonator.

- The affects of aliasing are examined in the context of harmonic balance circuit simulation. It is determined that a dual frequency set analysis scheme can provide accurate simulation results while reducing the number of frequencies needed for linear circuit evaluation and solution optimization. This technique reduces the number of costly cavity model evaluations needed during simulation and reduces the dimension of the error function [72].

1.4 Publications

The work associated with this dissertation resulted in the following publications;
refereed journal articles

P. L. Heron, G. P. Monahan, J. W. Mink, F. W. Schwering, and M. B. Steer, " Impedance matrix of an antenna array in a quasi-optical resonator," accepted for publication in *IEEE Trans on Microwave Theory and Tech.* Oct. 1993.

P. L. Heron, F. W. Schwering, G. P. Monahan, J. W. Mink, and M. B. Steer, "A dyadic Green's function for the plano-concave quasi-optical resonator," submitted for review to *IEEE Microwave and Guided Wave Letters.*

P.L. Heron and M.B. Steer, "Jacobian calculation using the multidimensional fast Fourier transform in the harmonic balance analysis of nonlinear circuits," *IEEE Trans on Microwave Theory and Tech,* pp. 429-431, Vol. 38, no. 4, April 1990.

C. R. Chang, P. L. Heron, and M. B. Steer, "Harmonic balance simulation of nonlinear microwave circuits using the block Newton method," *IEEE Trans on Microwave Theory and Tech,* pp. 431-434, Vol. 38, no. 4, April 1990.

S. Ziesberg, A. Schuenemann, G. P. Monahan, P. L. Heron, M. B. Steer, J. W. Mink, and F. K. Schwering, "Experimental investigation of a quasi-optical slab resonator," Accepted for publication by *IEEE Microwave and Guided Wave Letters.*

published proceedings

P. L. Heron, G. P. Monahan, J. E. Byrd, M. B. Steer, F. W. Schwering, and J. .W. Mink, "Circuit level modeling of quasi-optical power combining open cavities," accepted for presentation and publication by the *1993 IEEE Symposium on Microwave Theory and Tech.*

P. L. Heron C. R. Chang and M. B. Steer, "Control of aliasing in the harmonic balance simulation of nonlinear microwave circuits," *IEEE MTT-S International Microwave Symposium Digest*, 1989, pp. 355-358.

C. R. Chang, P. L. Heron, M. B. Steer, G. W. Rhyne, D. O. Riddle and R. S. Gyurcsick, "Simulation of nonlinear RF and microwave circuits," *Proceedings RF Expo East*, pp. 333-342, 1988.

Chapter 2

Literature Review

2.1 Background

All quasi–optical power combiners have in common the feature that multiple radiating structures couple energy into space where power is combined. The different types of combiners will be identified by the method which is used to achieve oscillator synchronization. Three common techniques have been utilized to phase lock the multiple solid state oscillators which comprise the power combining array. Direct radiation (DR) coupled combiners are synchronized by mutual field interactions between between an array of antennas. Microstrip patch antennas, being amenable to integrated circuit fabrication techniques, are often used. Fig. 2.1 depicts a DR combiner in which the radiating edges of adjacent patches are placed near one another to insure coupling.

Microstrip circuit (MC) coupled combiners are synchronized by providing locking through transmission lines or other microstrip circuit components. Some of the output power from each oscillator is transmitted through a microstrip circuit to provide locking for other oscillators. A transmission line MC coupled power combiner is shown in Fig. 2.2. Coupling between oscillators due to direct radiation is considered to be an undesirable parasitic effect, so the radiating edges of adjacent patches are often isolated as much as possible.

Quasi-optical resonator (QR) coupling is achieved by placing an active antenna array in a quasi–optical cavity. Fig. 2.3 depicts an example of a QR combiner. The

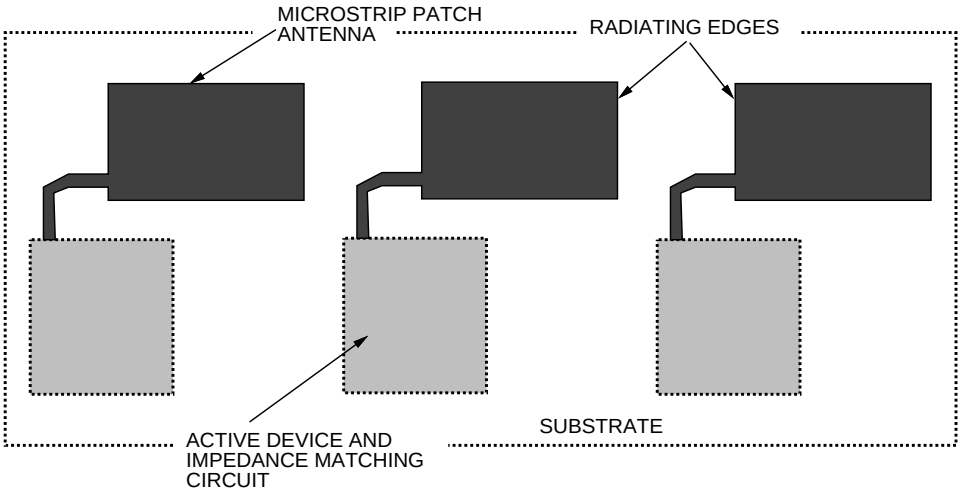

Figure 2.1: A Direct Radiation Coupled Quasi-Optical Power Combining Array

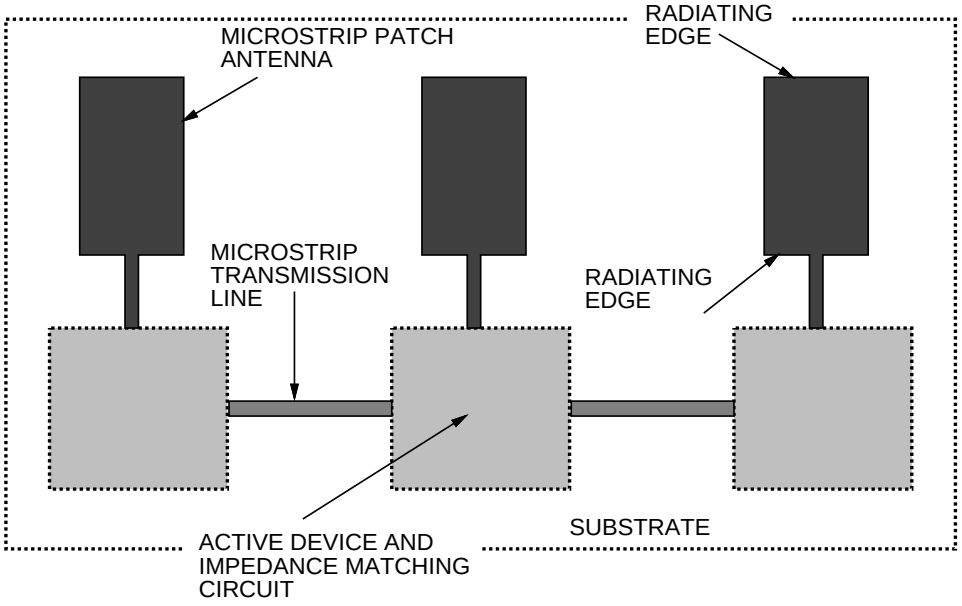

Figure 2.2: A Microstrip Transmission Line Coupled Quasi-Optical Power Combining Array.

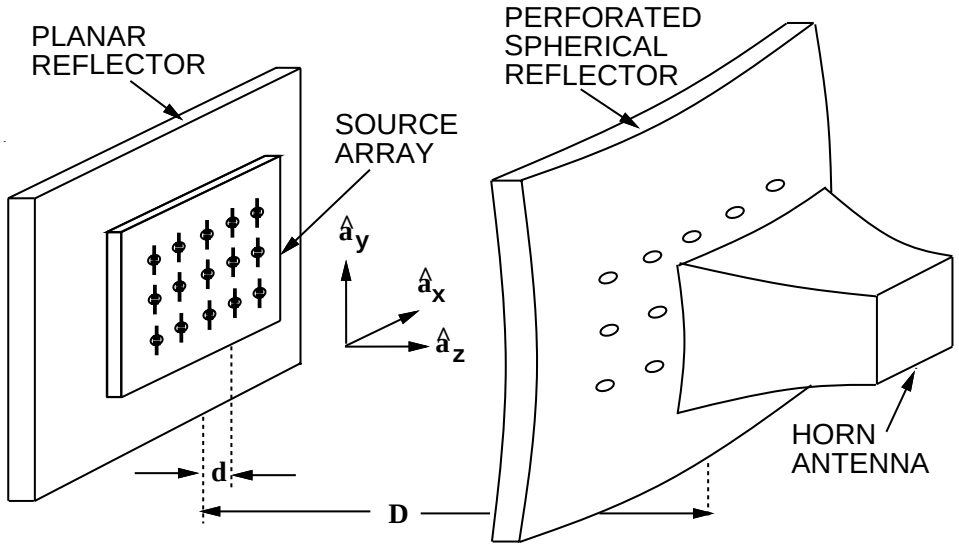

Figure 2.3: A Resonator Coupled Quasi-Optical Power Combiner Combining Array

cavity can be formed by two or more planar reflectors, two or more curved reflectors, or a combination of curved and planar reflectors. Each reflector can either have a solid surface, or may be of gridded construction. Power can be coupled out by use of dielectric reflectors, perforated metal reflectors, by aperture coupling to a waveguide, or by antenna coupling. Oscillators synchronize through the mode structure of the cavity. Coupling due to direct radiation is considered to be parasitic.

Results from prior quasi–optical power combiner work will be compared to assess the relative weaknesses and strengths of the three combining schemes. Some of the factors (many are interrelated) which should be considered when examining various power combiner designs are:

1. Suitability for array power combining; The first prototypes of most types of combiners have involved a small number of oscillators in a linear array. Some of the techniques do not easily lend themselves to use in two dimensional arrays or to integrated circuit technology.

2. Robustness; It is desirable that system performance degrade gracefully if one or more oscillators fail. A system should also tolerate statistical variations in circuit component values.

3. Efficiency; The combining scheme must efficiently combine the power of individual oscillators.

4. Simplicity; Circuits should be as simple to fabricate as possible. The system should allow close spacing of oscillators to achieve high source densities.

5. Radiation pattern; Since quasi–optical combiners use free space to combine the power from many oscillators, the output is a beam of radiation. As much power as possible should be in the main radiation lobe, directivity should be as high as possible.

6. Spectral purity and bandwidth; For autonomous systems, phase noise and spectral line width must be acceptable. These aspects as well as locking bandwidth are important for systems using external injection locking.

The analysis methods of the previous work will also be examined to determine if they can be applied to design improvement of quasi–optical power combiners. For design, an analysis method must be able to address the important system performance factors listed above. Examination of these previous efforts will provide context and motivation for this work.

2.2 Quasi-Optical Power Combiner Review

2.2.1 Direct Radiation Coupling.

York and Compton have studied the theory of weakly coupled oscillators [33]. Individual oscillators were characterized by their free running frequency, free running oscillation amplitude, and the oscillator external Q. Starting with an equation similar to Adler's equation, an expression was derived from which the array oscillation frequency and phase distribution could be numerically determined. It was assumed that the individual oscillators coupled weakly, and consequently that during the mutual interaction the amplitude of each individual oscillator was unchanged from its autonomous free running amplitude. Frequency locking dynamics were studied based upon the oscillator phases alone (independent of amplitude). The stability of various phase distributions was studied. The equations were first simplified by assuming nearest neighbor coupling only. Results of this analysis indicated that array end effects contribute significantly to the behavior of the system, particularly for small arrays. A simplified example of four identical oscillators was analyzed and it was concluded, for free space coupling, that the oscillators must be separated by distances equal to multiples of one wavelength so that array broadside radiation could be produced. This spacing is, in general, unsatisfactory as it produces radiation pattern grating lobes and at lower frequencies it can preclude a high area density of oscillators. Experiments were conducted using 4×4 arrays of Gunn diodes and MESFET's with rectangular microstrip patch antennas. An EIRP of 22 W was calculated for the Gunn diode array. Synchronization using free–space coupling could not be achieved. An open, low–Q rectangular cavity was required (one planar metallic and one planar dielectric reflector) to achieve oscillator synchronization. It

is unlikely that the assumption of weak coupling, and of nearest neighbor coupling are valid for the cavity coupled array. As a result, the study of the experimental power combiners bore little relationship to the previous theory. Reformulation of the theory to include the effect of the resonator may be possible. The experiments that were conducted provide an example which illustrates the difficulty commonly encountered in achieving array phase locking using direct radiation coupling.

Hummer and Chang [35] have demonstrated combining efficiency of 80% for two GUNN diode rectangular active patch antennas at 10 GHz. This is one of the earliest reports of successful synchronization of oscillators through direct radiation. A three IMPATT oscillator power combiner has been reported by Dinger in which each diode drives a microstrip patch antenna and the center diode was fed an external injection signal. Combining efficiency of 86% and locking range of less than 1% were reported at 10.2 GHz.

Stephan and Young [23] have modeled the mode selection and frequency pulling of two Gunn diode oscillators which were coupled through direct radiation. During an experiment at 10 GHz, the oscillator's slot antennas were aligned for maximum coupling, and then the phase of each oscillator was studied as a function of separation distance. Reasonable agreement was achieved between theory and measurement. The experimental antenna alignment that was used is impractical for power combining as co-planar oscillators would have a much weaker coupling. Shillue and Stephan [26] have studied the reactive coupling between two coupled IMPATT oscillators. The value of X_{12} was determined for two identical oscillators which where coupled by direct radiation. Simple circuit models were optimized to describe the behavior of a single oscillator. An expression was derived relating X_{12} to the separation distance between the oscillators and the oscillation frequency shift. A single oscillator was placed near a ground plane. From image theory this emulated two

oscillators locked in an odd mode regime and effectively provided a pair of exactly matched oscillators. A plot of values of X_{12} v.s. separation distance had the same behavior as was predicted by theory. This work provides a theoretical basis for the design of oscillators in arrays, but it does not address the important topic of non–identical oscillators.

Birkeland and Itoh [20] have constructed oscillators comprised of a patch antenna driven by two FET's which were locked in an odd oscillation mode by a microstrip line. The microstrip line also served as the radiating element. Four such oscillators have been phase locked by direct radiation when spaced approximately $3\lambda_0/4$ apart in a linear array. Very high combining efficiency and an EIRP of 31.7dBm were reported at 6 GHz. A four MESFET patch oscillator was also constructed. The element spacing was selected to produce desired coupling levels and the radiation pattern suffered somewhat at this spacing.

2.2.2 Microstrip Circuit Coupling

Stephan has used an analysis similar to Kurakawa's to derive a set of time domain differential equations which describe the behavior of a network of lumped element coupled oscillators [22]. The nonlinear equations were solved numerically assuming that the active devices and coupling mechanism were purely conductive. Qualitative agreement was attained by locking three VHF oscillators which were coupled through conductors. The results were not extended to distributed circuits. This work contains one of the first references to the concept of "inter–injection locking" of oscillators and suggests that this technique may be useful for quasi-optical power combining.

Camilleri and Bayraktaroglu [36] have achieved injection locking of a linear ar-

ray of three IMPATT oscillators at 43GHz. Each oscillator was monolithically constructed and used two IMPATT diodes and a resonant patch antenna. Planar circuit theory was used to derive a simple model for each oscillator. Phase locking was achieved by coupling through microstrip transmission lines so the coupling levels could be modified by varying the microstrip line impedance. The individual oscillators were biased in series using the transmission lines. The high ϵ_r of the GaAs substrate allowed the oscillators to be separated by one guide wavelength along the transmission line while being separated by about $\lambda_0/3$ in space. Broadside radiation without grating lobes was produced. Microstrip coupling on a high ϵ_r substrate permits higher oscillator surface density than does direct radiation coupling. Use of multiple active devices for each resonant patch antenna also allows increased device area density which can result in higher power levels. The feasibility of millimeter wave power combining using monolithically constructed source arrays was demonstrated.

Birkeland and Itoh [19] have constructed two port FET oscillators. Each oscillator consists of a common source MESFET, matching circuitry at the gate and drain, and a microstrip coupler which provides feedback between the drain and the gate. The coupler's two additional ports provide connections for an external injection input and as well as an output port which was connected to a load (antenna). A single oscillator was studied to determine the condition for oscillation assuming unilateral matched amplifiers and small signal conditions. Expressions for the single oscillator Q and locking bandwidth were determined. A five element linear array was constructed and studied at 6 GHz. The output from each oscillator was coupled to the injection port of the next oscillator in the chain. The first oscillator in the chain was fed by an external locking signal. Patch antennas were fabricated on a separate substrate which was placed at a right–angle to the oscillator substrate.

This scheme isolated the coupling structures from the antenna radiation, but two dimensional oscillator arrays would require longer antenna feeds which would be lossy. Free space power combining was achieved with an observed locking bandwidth of about 9% at 6 GHz. The direction of the radiation pattern main lobe was observed to vary significantly with change in oscillation frequency. Results of the single oscillator analysis were not applied to the array. This work validates the use of microstrip elements other than transmission lines to facilitate oscillator coupling.

Birkeland and Itoh later used the same type of microstrip directional coupler feedback FET oscillator in a 4×4 injection locked power combining array [21]. In this case, the individual oscillators were injection locked by an external signal which fed through a 16 way power dividing network comprised of 15 Wilkinson power dividers. Antennas were fabricated on a double sided substrate opposite the oscillators. The array output power was seen to be 150% of the sum of the individual oscillator powers. By coupling to an external injection signal only, this configuration eliminates the problem of limited bandwidth due to fixed oscillator spacing which occurs when inter–oscillator coupling is used. The reliability problem associated with inter-injection locked oscillators is also avoided. Any parasitic coupling occurring due to antenna interaction is undesirable. This uncoupling of the oscillators makes design easier as it involves not much more than single oscillator design. The disadvantage of this approach is that it requires more complex circuitry.

Microstrip coupling was used by Mortazawi and Itoh [17] in the design and construction of a second harmonic quasi-optical power combiner. Four X-band Gunn diode oscillators were placed periodically along a microstrip transmission line with each carefully designed to produce high levels of second harmonic output power. Each oscillator had an associated patch antenna which was resonant at the oscillator second harmonic frequency. Thus the oscillators were phase locked at the

fundamental frequency through a transmission line, but radiated at the second harmonic frequency. The oscillator spacing was approximately one transmission line wavelength at the second harmonic.

2.2.3 Quasi–Optical Resonator Coupling.

Popović [10] [11] has constructed and modeled a 10x10 MESFET planar grid oscillator. The MESFET's were located at the intersections of a regular rectangular grid of conductors which was supported by a dielectric substrate and had grid spacing of $\lambda_0/8$. Horizontal conductors served as common bias lines, vertical conductors served as antennas which couple the gate and drain of each MESFET to the cavity electromagnetic fields. This grid structure is unique because it does not use a ground plane which permits the grid to be suspended in space to interact with radiation. The grid was placed between a planar metallic reflector and a planar dielectric reflector which formed an open resonator. The characteristics of the unloaded grid were measured quasi–optically and fit to a circuit model. The grid was assumed to be infinite in extent and was assumed to be uniformly illuminated which allowed system analysis by considering a single grid cell. Frequency tuning due to reflector spacing was compared with predictions resulting in good agreement. The predicted oscillation frequency was determined by the length of the resonant cavity plus additional phase shift caused by the the reactance of the loaded grid. The system locking bandwidth was studied by injecting an external quasi-optical signal and improved spectral purity was observed. When used as an amplifier, the grid radiation can be steered by changing the angle of incidence of the input beam. An EIRP of 22 W at 5 GHz was reported. The observed D. C. to R. F. conversion efficiency of 15–20% is significantly below theoretical predictions. Wiekle [16] has correctly suggested

that the infinite grid modeling approach is inaccurate, particularly for small grids, because it ignores grid edge effects. He suggested that the grid be modified by including reactive loading at the edges which would make the infinite grid model more accurate but no empirical method for modifying the grid was given. This approach, however, still ignores the internal field structure of the resonator by incorrectly assuming uniform illumination [54]. This effect may be reduced somewhat by using reflectors having aperture dimensions much larger than that of the grid. If the grid could be constrained to oscillate at the frequency corresponding to a mode of low transverse order, the field would be approximately uniform in the vicinity of the grid. The need for an approach which models the entire grid is suggested. Mink [3] was the first to perform such an analysis for point sources in a cavity.

The experimental grid oscillators of Popović could not be made to oscillate at higher frequencies [16]. This is likely due to the large number of longitudinal cavity modes which caused the oscillators to lock at a low frequency mode where the MESFETs have high gain. Filter grids or other structures can be placed in a quasi-optical system to eliminate undesirable low frequency resonant modes. Lee [37] has demonstrated a cavity configuration which eliminates all but a single longitudinal cavity mode.

Wiekle has constructed a grid oscillator similar to that of Popović [15]. He connected the MESFETs to the grid so that the gate was not directly coupled to the resonator radiation. Rather than coupling through the mode structure of the resonator, coupling was influenced by adjacent oscillators along the grid. This dependence on grid spacing resulted in the cutoff of many lower frequency modes and resulted in a reduction of injection locking bandwidth. It is likely that this type of grid cannot be used as an amplifier with a steerable output beam.

Mink [3] has studied the coupling of an array of point sources to the mode struc-

ture of a plano-concave open resonator. The Lorentz reciprocity theorem was used to find the coupling coefficients between the point source current and the natural short-circuit modes of the cavity. The mode coupling coefficients and radiation resistance were determined for arrays of equal and Gaussian weighted sources. Very high combining efficiencies were predicted. This type of approach overcomes the shortcomings of the infinite grid or plane wave approximation. The calculations were valid for a single resonator spacing. It was assumed that all transverse modes were degenerate, that the element impedances were purely resistive, and coupling into non–resonant fields was not considered.

The resonator was also assumed to be of high Q. The strong field interactions in the cavity also provide for a larger locking bandwidth, so individual oscillator tolerances can be relaxed when compared with a direct radiation coupling scheme. Another advantage open resonators is the production of a highly focused radiation pattern. For example, in the far field the angle between the half power points of a Gaussian beam from a confocal resonator with spacing b is [51]

$$\theta = 360\sqrt{\frac{\lambda \ln 2}{b\pi^3}} \text{ degrees.} \tag{2.1}$$

This beam would be transmitted through a dielectric lens whose inner and outer surfaces have curvatures corresponding to that of the beam phase front at the surface locations. Additional focusing is possible by modifying the curvature of the exterior surface. The Green's function derivation in this dissertation begins by removing as many assumptions from Mink's analysis as possible and also treating the case of distributed sources.

Xue and Wang [27] have used Mink's result to study the effects of the longitudinal location of the source array in an open cavity. They confirm intuition in that the electric field standing wave null locations are low impedance locations, and that

anti-node locations are high impedance locations. Wang [29] has used a computer program and the results of Mink's investigation to find the source spacing in the transverse plane which optimizes either fundamental mode power, or combining efficiency for an array of small dipoles.

Several experimental power combiners using focused open cavities and aperture coupling have been reported. In most of these cases heuristics were used to design a small functional system. Stephan [25] has used an aperture-coupled semi-confocal plano-concave resonator to stabilize a single RTD oscillator at X-band. The RTD shows potential as a millimeter wave source due to its extremely broad bandwidth negative conductance. Nakayama [14] has demonstrated an open cavity power combiner which uses a grooved planar reflector facing a curved reflector. In one experiment up to eighteen Gunn diodes were mounted in the transverse grooves. During a second experiment six FETs were placed on the surfaces between the grooves. Phase locking was achieved in X-band with elements offset by a distance of about $\lambda_0/2$. Oscillation frequency was mechanically tuned by varying reflector spacing, and shown to agree with theory. A perturbation technique was used to measure the transverse field distribution which was shown to be that of the dominant TEM_{00} mode. A 50 GHz single element Gunn diode oscillator was also reported. A Gunn diode power combiner using two curved reflectors was reported by Wang [29]. Each diode was located in a shorted section of full height waveguide. The open waveguide ends faced the cavity through apertures in the surface of one of the reflectors. Phase locking was reported at 100 GHz. A similar configuration was used by Ge [30] at 36 GHz in which two reduced-height Gunn diode oscillators were constructed. Each oscillator combined the power of two packaged diodes which were located side by side in the waveguide. The open end of each waveguide oscillator was coupled into a plano-concave resonator through the planar reflector. The total output power

was less than the sum of the powers from the individual oscillators. Many of these QR combiners have employed techniques that are not amenable to integrated circuit construction. Little theoretical work has been performed to model these power combiners. An aperture coupled QR combiner that can use integrated circuits will be proposed in chapter 5. This system can be analyzed using the techniques of chapter 4.

2.3 Summary

2.3.1 Combiner Configuration

Much of the previous work on quasi–optical power combiners has been at the *proof of concept* level. The systems have usually been small, combining the power of just a few solid state oscillators. Many aspects that are necessary for the design of practical combiners using a large number of oscillators have not yet been addressed. However, some information about the general properties of the three types of combiners can be discovered by studying these small scale experimental systems. At first glance, circuit complexity may appear to be a good criterion for assessing the different coupling techniques. For example, DR and QR coupled designs require the least complicated array circuits. Of these, DR systems appear to be the most simple as no resonator is necessary. MC combiners require additional circuit networks for inter–injection locking, and thus require more complicated topologies. If the surface area of these microstrip networks can be kept sufficiently small, the circuits can be produced monolithically with little difficulty. Practical considerations other than circuit complexity tend to come to the fore when comparing the coupling schemes.

Coupling between DR oscillators appears to be very weak and local in nature.

This leads to two significant problems in designing a large DR coupled combiner. First, experience has shown that experimental linear arrays will synchronize only if the individual oscillators are carefully tuned to have nearly identical free running oscillation frequencies. These tight tolerances may require hand tuning which is undesirable with integrated circuits. Second, all successful experimental DR combiners have consisted of linear arrays, each antenna having its radiating edges next to the radiating edges of the adjacent antennas, as depicted in Fig. 2.1. This alignment provides the strongest possible coupling which aids in synchronization. A practical system would have to consist of a two dimensional array

achieve an acceptable radiation pattern and to attain a high density of oscillators. It is doubtful that coupling between the rows of a two dimensional DR system would be sufficient for synchronization.

Another fundamental problem with DR coupled combiners is an inherently poor radiation pattern (even if synchronization between rows can be achieved in two dimensional arrays). This is because the inter–oscillator spacing determines the relative phase of each oscillator at synchronization, this spacing and phase distribution also determines the array radiation pattern. Since the same spacing influences the oscillators phases as well as the array factor, significant power will be radiated into undesirable side lobes. Finally, it is expected that DR coupled systems will not be robust. Synchronization has only been attained by carefully tuned linear arrays. Due to the required tight tolerances, it is expected that system performance will degrade severely if one or more oscillators fails. Despite the promise of simple circuitry, the DR type combiner faces the greatest number of obstacles before it can be used in practical systems.

Existing microstrip circuit techniques and components can be applied to the design of MC type combiners. An important system design consideration is the

minimization of coupling by direct radiation. Other than this, a system can be designed modularly by considering a single oscillator along with its input and output injection ports. Unlike DR combiners, oscillation frequency of MC combiners can be electronically tuned by placing variable phase shifting elements in the coupling circuitry. Unfortunately, phase shifting or implementation of other functions requires additional circuitry on the source substrate which complicates the design and reduces reliability. Radiation patterns can be much better than those of DR combiners. The phase of each oscillator is determined by the phase shift which occurs through the coupling circuits, not by the free space separation between antennas.

All experimental inter–injection locked MC systems have been linear arrays. A two dimensional array could be formed by folding a long linear array, but reliability problems would ensue. To increase reliability, oscillators with multiple output injection ports, and possibly multiple input injection ports, must be used. Unfortunately, this will further increase the circuit complexity. MC combiners show promise as being the type to be most quickly developed into large systems.

There are several attractive aspects of the QR coupling scheme. Phase locking is truly global in nature, each oscillator couples into the cavity mode structure. If one or more oscillators fails, the system will still remain synchronized. There are no constraints on oscillator spacing because each oscillator will lock to the phase of the cavity mode structure at its location. To reduce the undesirable coupling due to direct radiation, it may be necessary to maintain a minimum spacing between oscillators or to offset alternate rows of the array. QR systems are simple to construct, needing no circuitry for coupling and having fairly relaxed circuit tolerances because the high field strength in the cavity results in strong coupling. Cavity alignment presents no difficulty if one or more of the reflectors is spherical (for planar reflectors alignment is critical). The cavity can present an extremely high Q to the active

devices resulting in tight frequency control. A focused cavity confines energy with little diffraction loss, thus high combining efficiency is possible. As with MC combiners, electronic tuning of oscillation frequency can be achieved by use of phase shifting components. An advantage of the QR scheme is that the phase shifting components can be fabricated in a separate array which is placed inside the cavity [13]. The ability to place phase shifting or other functional circuitry on a substrate separate from the source greatly simplifies design and increases system reliability.

Many of the undesirable features of the QR system center around the resonator. Oscillation frequency is strictly controlled by cavity geometry and so may be susceptible to vibration or temperature variations. The cavity is a cumbersome structure when compared with the planar structures of DR and MC systems. Another problem arises due to the spectral density of modes in the cavity. Higher order transverse modes can easily be eliminated by appropriate cavity design or through use of apertures [47]. Although a QR system frequency can be mechanically tuned by changing the reflector spacing, the range of tunability can be severely limited due to the spectral density of the longitudinal modes. For a cavity having frequency spacing Δf_q between longitudinal modes, the tuning frequency range δf is restricted to $\delta f \approx \Delta f_q/2$. The spacing between reflectors, D, of quasi–optical cavities is usually much larger than a wavelength which results in a small $\Delta f_q = c/(2D)$, and thus limited mechanical tunability. The number of resonant longitudinal modes can be reduced by use of wire grid filters or by using additional resonant structures. Lee reports constructing a high Q cavity having only a single resonant longitudinal mode [37].

2.3.2 Analysis Methods

MC coupled systems can be designed using existing microstrip circuit theory. Commercial simulators in conjunction with an antenna model can be used to design these systems using a modular approach. These existing tools should be applied to development of simple and robust designs.

Much of the study of DR and QR type combiners has required the assumption of identical oscillators placed in a regular grid. While this simplification renders the computations more tractable, it severely limits the usefulness of the analysis. This simplification precludes the ability to study the effects of nonuniform oscillators. Oscillator non-uniformity can arise unintentionally due to circuit fabrication variance, or an inhomogeneous array can be designed intentionally. DR coupled combiners are subject to array edge effects while QR combining arrays are illuminated by nonuniform resonator modal fields. It is likely that an optimal array for these applications will have nonuniform grid spacing, and will not utilize identical oscillators or radiators. Grid inhomogeneity can also be caused by device failure. These important effects can only be studied by using simultaneous analysis of an entire array. This formidable task is possible only through numerical computation. For large arrays, the requirements of this analysis may exceed present day simulation capabilities. It is hoped that insight into power combining array behavior can be gained though the study of small arrays. Study of small systems may suggest appropriate model simplifications or design rules which can be applied to the study and construction of large arrays. Armed with this philosophy, it is the goal of this work to discover techniques which allow sufficiently rigorous analysis of the entire QR oscillator array. These methods may be applied to DR combiners by substituting the simpler half–space Green's function for the complete cavity Green's function

during analysis.

Chapter 3

Green's Function of an Open Resonator

3.1 Introduction

In this chapter a Dyadic Green's function, $\bar{\mathbf{G}}e_c$, is determined by considering a plano–concave cavity. This derivation considers a particular geometry, however the concepts of this chapter are applicable to a much more general group of problems. The techniques that are used here can be applied to open cavities having other types of reflectors simply by using an eigenfunction expansion that is appropriate for the geometry which is being considered. In addition to cavities, the Green's function can be used to find the coupling to a variety of Gaussian optical systems. The properties of a Gaussian optical system referred to the plane $z = D$ (Fig. 2.3) can be substituted into the derivation in place of the curved reflector boundary condition. The resulting Green's function can be used to optimize feeds for Gaussian optical systems. The techniques which are employed here, can therefore function as a bridge between microwave circuits and Gaussian optics.

In this work the Green's function provides a means for determining the field distribution within the cavity, ($\mathbf{E}_c$, $\mathbf{H}_c$), which is excited by a source current density $\mathbf{J}_S$, $\mathbf{M}_S$. The Green's function relates these quantities through the operation

$$\mathbf{E}_c(r) = \int_{\Omega'} [\bar{\mathbf{G}}e_c(r'|r)\cdot\mathbf{J}_S(r') + \bar{\mathbf{G}}h_c(r'|r)\cdot\mathbf{M}_S(r')]dv', \tag{3.1}$$

where the ordinates $r = \{x, y, z\}$, denote the observation coordinate system, $r' = \{x', y', z'\}$, the source coordinate system, and Ω' is a volume which contains the

source current distribution ($\mathbf{J}_S$, $\mathbf{M}_S$).

Physical effects that must be included in $\bar{\mathbf{G}}e_c$ may be determined by considering a single antenna radiating into an open resonator such as shown in Fig. 2.3. A current density $\mathbf{J}_S$ is established on the antenna by an active source. This current will induce electromagnetic fields. Some energy will be stored in fields which are confined within the resonator and will satisfy appropriate boundary conditions on the reflector surfaces. These fields will be termed the cavity modal fields, or the cavity resonant fields. The modal fields will be considered to be comprised of a superposition of traveling wave beam modes. A beam traveling in the $+\hat{\mathbf{a}}_z$ direction interacts with the reflector at $z = D$ and is transformed into a wave beam which travels in the $-\hat{\mathbf{a}}_z$ direction. A beam traveling in the $-\hat{\mathbf{a}}_z$ direction interacts with the reflector at $z = 0$ and transforms into a beam traveling in the $+\hat{\mathbf{a}}_z$ direction. The modal fields will suffer energy loss due to several effects. As each traveling beam traverses the cavity from one reflector to the next, diffraction will cause expansion of the beam. Some of the beam's energy will spill around the edges of the reflector and will be lost as radiation. This mechanism is termed diffraction loss. Some of the wave beam energy that impinges on the reflectors will be lost due to the finite conductivity of metallic reflectors, losses in dielectric reflectors, or can be intentionally coupled out of cavity as useful output power. These mechanisms will be grouped together and termed reflector loss. $\mathbf{J}_S$ will also induce fields which do not couple into cavity modes. Some of this energy will radiate without being confined by the open cavity and will be termed direct radiation loss. Some energy will remain localized close to the antenna and will contribute to the antenna's near field pattern. These three types of fields and their associated losses will be included in $\bar{\mathbf{G}}e_c$. The same mechanisms apply to the interactions between multiple antennae radiating into a resonator. We will see in chapter 4 that including these effects

into the Green's function can give better results than those obtained by using an antenna model in conjunction with a partial Green's function. It is likely that near field coupling and direct radiation coupling between elements will be particularly important when large arrays are located in a cavity as the spacing between radiators will then be very small and the direct radiation field strength can be large.

In this chapter, the eigenfunctions for a plano–concave cavity and the methods that were used to determine these modes will be discussed. A form for the resonant cavity field structure will be proposed when the cavity is excited by an arbitrary source current located in a plane $z = d$. Using the assumed field structure, the Lorentz reciprocity theorem will be applied to determine the coupling between the source current and the modal fields. A dyadic Green's function for the resonant fields, $\bar{\mathbf{G}}e_r$ will be formulated. $\bar{\mathbf{G}}\mathbf{e}_r$ will be used in conjunction with a half space dyadic Green's function to determine the complete cavity Green's function, $\bar{\mathbf{G}}\mathbf{e}_c$. The derivation of a cavity Green's function for magnetic currents, $\bar{\mathbf{G}}\mathbf{h}_c$, will be presented.

3.2 Cavity Field Structure

The microwave frequency properties of Fabry–Perot resonators have been extensively studied. Prior to improved fabrication technology which resulted in the reduction of transistor noise figures, the MASER was considered a likely candidate for microwave signal amplification. Significant work was performed in the early 1960's to determine the field structure and diffraction losses of open resonators [47]–[57].

Fox and Li [54] considered resonators with planar reflectors having both circular and rectangular apertures as well as resonators with confocal spherical reflectors of circular aperture. The method they used for spherical reflector resonator analysis

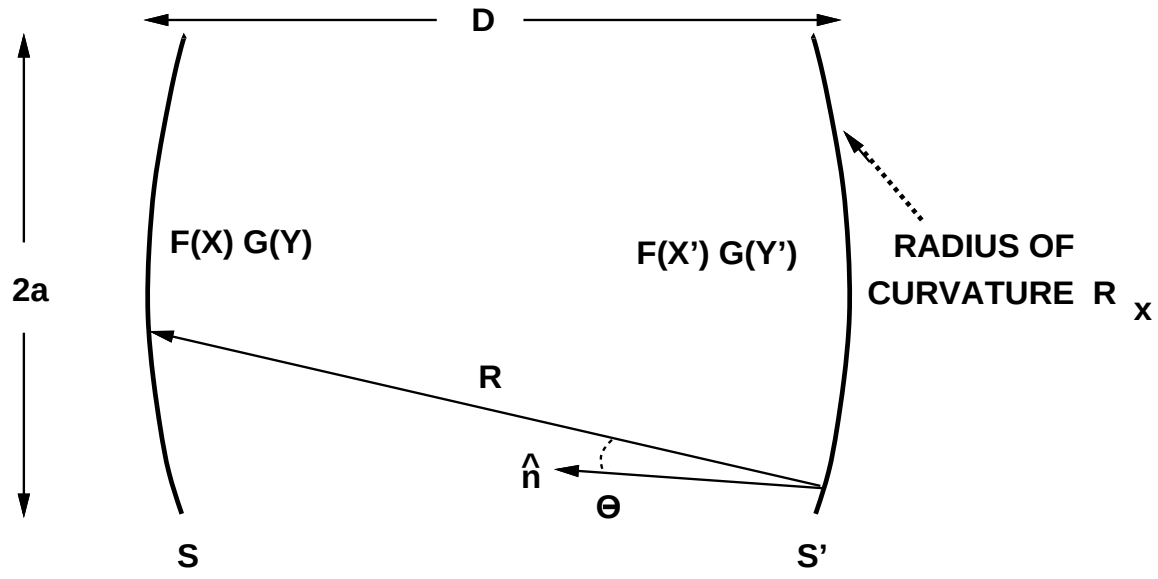

Figure 3.1: Cross Section of a Cavity Having Identical Spherical Reflectors.

can be described by referring to Fig. 3.1 which shows a cross section of the resonator. The term confocal is used to indicate that the reflector focal points coincide at the point on the z axis midway between the reflectors. For shallow spherical reflectors, the focal length is taken to be $1/2$ the radius of curvature of the lenses, so the reflector spacing for confocal spherical reflectors is equal to the radius of curvature. The field structure of the cavity studied in this dissertation having reflector spacing D, Fig. 2.3, is the same for the cavity of Fig. 3.1 with reflector spacing $2D$ if we consider only the even order longitudinal modes. These modes satisfy the boundary condition for a perfectly conducting planar reflector located at $z = 0$, $\hat{\mathbf{a}}_z \times \mathbf{E} = 0$. Integral equations are formulated based upon Huygen's principle which related the field intensity on reflector S to the field distribution on S'.

The field distribution at reflector S', $u(\mathbf{r}')$, is considered to be a distributed Huygen's source which produces a traveling wave beam and results in the the field distribution,

$v(\mathbf{r})$, at the other reflector. The two distributions are related through

$$v(\mathbf{r}) = \int_{S'} K(\mathbf{r}, \mathbf{r}') u(\mathbf{r}') dA' \tag{3.2}$$

where K is the kernal $jk(1+\cos\theta)\exp(-ikR)/(4\pi R)$ which arises from application of Huygen's principle, and θ is the angle between the normal $\hat{\mathbf{n}}$ and $\mathbf{R}$. When the fields are at resonance, the distribution on S and S' are identical except for a complex proportionality constant γ which accounts for a uniform phase shift as well as diffraction losses.

$$u(\mathbf{r}') = \frac{v(\mathbf{r})}{\gamma}. \tag{3.3}$$

The aperture field distribution and diffraction loss are then determined by iteration in the following manner. $u(\mathbf{r}')$ is selected to be uniform, i.e. a plane wave over the aperture, then substituted into the integrand (3.2). Numerical integration is performed to determine $v(\mathbf{r})$ which is substituted back into the integrand. This iterative procedure continues until the value $\gamma = v/u$ is constant from iteration to iteration. Fox and Li's calculation required more than three hundred iterations to acquire a stable solution. This method of determining cavity eigenfunctions and eigenvalues is impractical for use in a simulator. The integral equation formulation is important when more efficient methods are used for its solution.

Implicit in the use of Huygen's principle are the requirements that each reflector is in the far field of the other reflector, that $b >> \lambda$, and that the reflector apertures are much larger than a wavelength $2a >> \lambda$. Further, it was assumed that the curvature of the spherical mirrors was sufficiently small as to approximate parabolic mirrors, and that $(b/a)^2 >> a^2/(b\lambda)$.

Boyd and Gordon [51] also considered a confocal resonator with spherical reflectors. They were able to arrive at an analytic solution for a resonator with square

reflector apertures. Starting with (3.2) they assumed that $\theta \approx 0$ (which is known as the paraxial condition), that $1/R \approx 1/D$ and used the first two terms of a series expansion for R in the phase term of $K(\mathbf{r}, \mathbf{r}')$. Using these simplifications and assuming the form $v(\mathbf{r}) = F(X)G(Y)$, they were able to separate the integral equation into two identical first order integral equations. The dimensionless variables are defined as $X = x\sqrt{c}/a$ and $Y = y\sqrt{c}/a$ and the numerical aperture parameter $c = 2\pi a^2/(D\lambda)$ is related to the Fresnel number. The resulting first order integral equations indicate that the solution of the square aperture confocal spherical resonator problem is the product of two solutions each for an infinite strip cylindrical resonator.

For the case when $D = b$, the solutions to the integral equation were found to be

$$F_m(c, \frac{X}{\sqrt{c}}) \propto S_{0m}(c, \frac{X}{\sqrt{c}}), \tag{3.4}$$

$$G_n(c, \frac{Y}{\sqrt{c}}) \propto S_{0n}(c, \frac{Y}{\sqrt{c}}), \tag{3.5}$$

$$\chi_m = \sqrt{\frac{2c}{\pi}} i^m R^{(1)}_{0m}(c, 1), \quad m = 0, \quad 1, \quad 2, \quad \ldots \tag{3.6}$$

The diffraction loss can be determined from

$$\gamma = \frac{-i \exp(ikD)}{\chi_m \chi_n} \tag{3.7}$$

S_{0m} and $R^{(1)}_{0m}$ are the angular and radial prolate spheroidal wave functions respectively. Unfortunately, there is no straight forward method to calculate S_{0m} and $R^{(1)}_{0m}$ and these functions are tabulated only for discrete values of the parameter c [58] [59]. Also, these results apply only to a semi-confocal spacing of the plano-concave resonator.

Boyd and Gordon observed for values of X, Y such that $X, Y << \sqrt{c}$, i.e. close to the center of the reflector, that the angular wave function could be approximated

by Hermite Gaussian functions

$$F_m(X) \approx \mathrm{He}_m(X) \exp\left(-\frac{X^2}{2}\right) \tag{3.8}$$

Where $\mathrm{He}_m(X)$ are complete polynomials of order m called Hermite polynomials and are generated by

$$He_m(X) = (-1)^m \exp(X^2/2) \frac{d^m}{dX^m} \left(\exp(-X^2/2)\right). \tag{3.9}$$

Hermite polynomials are orthogonal in that they satisfy the relation

$$\int_{-\infty}^{+\infty} He_s(X) He_m(X) w(X) dX = m! \delta_{sm} \sqrt{2\pi} \tag{3.10}$$

where the weight function $w(X) = \exp(-X^2/2)$, and δ_{sm} is the Kronecker delta.

The approximation (3.8) for F and G is better for larger values of c and for smaller values of the transverse mode order m. For many practical systems the approximation is sufficiently accurate. Unfortunately no acceptable approximation exists for calculation of γ. Boyd and Gordon next applied Huygen's principle to derive the traveling wavebeam electric field distribution at an arbitrary plane z_0. A method was also devised to determine the approximate field distribution for arbitrary non–confocal resonator configurations.

Using an alternate method, Weinstein later derived results similar to Boyd and Gordon for spherical reflector resonators in the oblate–spheroidal coordinate system. The cases of circular and rectangular apertures with arbitrary reflector spacing were treated. Assumptions similar to those previously used were made to simplify the Hemholtz equation for the resonator. Next the simplified equation was solved to determine a scalar potential function on the reflector surfaces. Surface current density was derived from this potential function. Potential theory can be used to determine the field components from the reflector current density. An xz plane cross section of

the oblate spheroidal coordinate system is shown in Fig. 3.2. This coordinate system is the natural coordinate system for the spherical resonator problem. It is presented here because several properties of the resonator field structure can be visualized by examining the constant coordinate surfaces.

The oblate spheroidal coordinates are η, θ, and ϕ. The ordinate ϕ indicates rotation about the z axis with the x axis corresponding to $\phi = 0$. The plane of Fig. 3.2 corresponds to the two half planes $\phi = 0$ and $\phi = \pi$. The η = constant surfaces are oblate spheroids which correspond to phase fronts of the traveling wave beams. For restricted values of ϕ and θ the spheroidal caps represent the region of the spherical reflectors. The electric field vector is polarized along the constant–ϕ surfaces which become planes at $z = 0$ and correspond the curvature of the reflectors at their surfaces. In this work we will consider shallow spherical reflectors and sources located near the beam waist so the field is assumed to be linearly polarized in the $\hat{\mathbf{a}}_\mathbf{y}$ or $\hat{\mathbf{a}}_\mathbf{x}$ direction, i.e. TEM. This corresponds to the $z = 0$ region of the oblate–spheroidal coordinate system where the spheroidal phase surfaces are approximately planar. The constant–θ surfaces are hyperboloids of one sheet. The electric field strength is highly concentrated near the z axis, but decays evanescently in a direction normal to the hyperboloids which are termed caustic surfaces. For a constant z, the radius at which the beam field strength drops to $1/e$ of its maximum value is called the beam radius or waist. For all values of z in the resonator, the beam waist corresponds to a particular constant–ϕ surface. As indicated, the beam waist has a minimum value termed w_0 at $z = 0$ and a maximum value at the reflector surfaces.

Soohoo also considered the spherical reflector resonator with square apertures but he considered arbitrary spacing [53]. Starting with (3.2) the same approximations as Boyd and Gordon were used except that three terms were retained in the

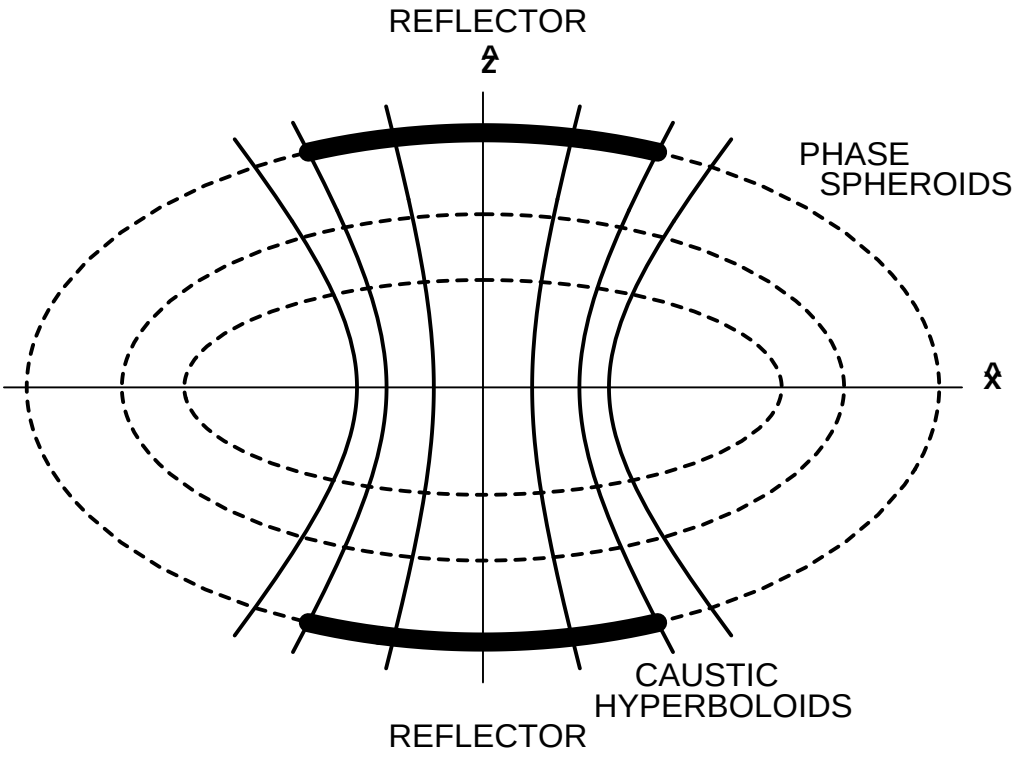

Figure 3.2: Cross Section of Oblate Spheroidal Coordinate System, the $\eta =$ Constant Oblate Spheroids and $\phi =$ Constant Hyperboloids of One Sheet are Generated by Rotation Around the z Axis.

binomial expansion of the exponential phase term of the kernal. The equation was then separated into two identical first order integral equations, each of the form

$$F_m(X) = \frac{1}{\chi_m\sqrt{2\pi}} \int_{-\sqrt{c}}^{+\sqrt{c}} F_m(X') \exp\left(iXX'\right) \exp\left(i(D-R_x)(X^2+X'^2)/(2D)\right) dX' \tag{3.11}$$

which are then solved numerically. Here R_x represents the radius of curvature of the reflector along the x axis. The solution was performed by considering a set of discreet points on S and S' and then approximating the integration in (3.11) by numerical quadrature. The field at the ℓ th point on S is found by considering the contributions from all points on S',

$$F_m(X_\ell) = \frac{h}{\chi_m\sqrt{2\pi}} \sum_{j=0}^{n} \left(A_j \exp\left(iX_\ell X'_j\right) \exp\left(i(D-R_x)(X_\ell^2+X_j'^2)/(2R_x)\right) F_m(X'_j) \right) \tag{3.12}$$

where h is the X interval between the n uniformly distributed points on S', and A_j are the weights associated with the quadrature formula. For example, if Simpson's rule is used, we have

$$A_j = 1/3, \;\; 4/3, \;\; 2/3, \;\; 4/3, \;\; ...2/3, \;\; 4/3, \;\; 1/3.$$

If we form a vector of all the $F_m(X_\ell)$, we can write (3.12) as a matrix equation

$$\sqrt{2\pi}\chi_m \mathbf{F_m} = \mathbf{H}\mathbf{F_m}. \tag{3.13}$$

Equation 3.13 is recognized as an eigenproblem, the square matrix $\mathbf{H}$ is loaded according to (3.12), an eigenproblem solver is then used to determine the n eigenvectors $\mathbf{F_m}$ and the n eigenvalues χ_m. This method provides an accurate and efficient method for determining resonator diffraction losses and is used in this work.

At the same time that MASER resonator work was being conducted, research was being conducted on beam waveguides [42]–[46]. Goubau and Schwering showed that a wavebeam could be guided though space by periodically placing phase transformers along a transmission axis [42]. The relative field amplitude distribution was the same at each transformer, the power of the beam decreased due to diffraction. Solutions of the paraxial wave equation for these systems showed that beam waveguides produce the same field structure as quasi-optical resonators. The iterative beam waveguide problem and the open resonator problem are mathematically identical. In the beam waveguide, a traveling wavebeam is periodically refocused by apertures and transmitted, the field structure is replicated in each waveguide section. In the resonator, a wavebeam is refocused and reflected by lenses, the field structure is replicated each pass through the resonator. In each case, diffraction losses are caused by finite aperture sizes. For both cases the analysis used to derive the fields is only valid if the beams are not focused too tightly, $w_0 \approx 2\lambda$, otherwise the paraxial assumption is violated.

For this work, the resonant modal electric fields within the cavity are considered to be the superposition of a linearly polarized diverging wavebeam traveling in the $\hat{\mathbf{a}}_\mathbf{z}$ direction, $\mathbf{E}^+_{mn}$, and a linearly polarized converging wavebeam traveling in the $-\hat{\mathbf{a}}_\mathbf{z}$ direction, $\mathbf{E}^-_{mn}$. Assuming that all resonator dimensions are large compared with a wavelength, that $D^2/a^2 \gg N$, and that the Fresnel number $N = a^2/(D\lambda)$ is sufficiently large, the traveling wavebeams can be expressed as Hermite-Gaussian functions for a resonator with rectangular apertures. If the spherical reflectors have a radius of curvature $2F_x$ in the $\hat{\mathbf{a}}_\mathbf{x}$ direction , and curvature $2F_y$ in the $\hat{\mathbf{a}}_\mathbf{y}$ direction, we can write the electric field strength as [43]

$$E^{\pm}_{mn}(x,y,z) = \frac{(\mu/\epsilon)^{1/4}}{\sqrt{\pi \bar{X}\bar{Y} m!n!}}(1+u^2)^{-1/4}(1+v^2)^{-1/4} He_m(\sqrt{2}x/x_z) He_n(\sqrt{2}y/y_z)$$

$$\exp\left\{-\frac{1}{2}\left[(x/x_z)^2+(y/y_z)^2\right]\mp\jmath\left[kz+\frac{1}{2}\left(u(x/x_z)^2+v(y/y_z)^2\right)\right.\right.$$
$$\left.\left.-\left(m+\frac{1}{2}\right)\tan^{-1}(u)-\left(n+\frac{1}{2}\right)\tan^{-1}(v)\right]\right\} \tag{3.14}$$

where,

$$u=\frac{z}{k\bar{X}^2},\qquad v=\frac{z}{k\bar{Y}^2}$$
$$x_z^2=\bar{X}^2(1+u^2),\qquad y_z^2=\bar{Y}^2(1+v^2).$$

In the above expressions k is the free space wavenumber and variables $\bar{X}$ and $\bar{Y}$ are called the Gaussian mode parameters and determine the rate at which the field strength decays in the $\hat{\mathbf{a}}_\mathbf{x}$ and $\hat{\mathbf{a}}_\mathbf{y}$ directions respectively. The mode parameters are defined as [43]

$$\bar{X}^2=\frac{1}{k}\sqrt{\left(F_xD\left(2-\frac{D}{F_x}\right)\right)},\quad \bar{Y}^2=\frac{1}{k}\sqrt{\left(F_yD\left(2-\frac{D}{F_y}\right)\right)}.$$

The *vector* electric field is assumed to have transverse polarization (i.e. no $\hat{\mathbf{a}}_\mathbf{z}$ component). This assumption is valid because we have required that the reflector's radius of curvature be very much greater than a wavelength. Thus the oblate spheroidal phase fronts as seen in 3.2 have little curvature. The TEM approximation is particularly appropriate near $z=0$ where the phase front is planar and near the z-axis where the fields are purely transverse. This region is desirable for location of sources in a quasi-optical system.

From our TEM approximation, the magnetic field $\mathbf{H}_{mn}^{\pm}$ is found from the vector electric fields $\mathbf{E}_{mn}^{\pm}$ using

$$\mathbf{H}_{mn}^{\pm}=\pm\sqrt{\frac{\epsilon}{\mu}}\hat{\mathbf{a}}_\mathbf{z}\times\mathbf{E}_{mn}^{\pm}. \tag{3.15}$$

The traveling wave beams, as expressed in (3.14), are normalized so that unit power is carried through any transverse plane and in any constant z transverse plane satisfy the orthogonality condition

$$\int_S \mathbf{E}_{st}^{\pm}\cdot\mathbf{H}^{*\pm}_{mn}ds=\sqrt{\frac{\epsilon}{\mu}}\int_S E_{st}^{\pm}E_{mn}^{\mp}ds=\delta_{sm}\delta_{tn}. \tag{3.16}$$

Boundary conditions can be applied at the reflector surfaces of the resonator in Fig. 2.2 to relate the amplitudes of traveling wave components to the normal modal resonant fields for this structure. The planar reflector is assumed to be perfectly conducting and of infinite extent so that

$$\hat{\mathbf{a}}_z \times \mathbf{E} = 0 \quad \text{at} \quad z = 0. \tag{3.17}$$

The spherical reflector is characterized by its effect on an incident single mode beam. Some of the incident power is reflected and focused to produce a scattered beam having the same mode and beam parameters while the remaining power is transmitted through the lens. The lens is assumed to be reciprocal and that it does not change the polarization state of an incident wavebeam. Thus the reflector is characterized as having a reflection coefficient R_{mn} and transmission coefficient T_{mn} for the mn th Hermite-Gaussian beam mode.

The resonant transverse fields excited by a source current are expressed as a series of these modal fields with the coefficients determined by use of the Lorentz reciprocity theorem and an applied test field. Inspection of the expressions which result from this calculation will yield $\bar{\mathbf{G}} e_r$.

The test field is excited by an incident unit-amplitude, single–mode wavebeam which originates from $z \gg D$ and converges upon the resonator as seen in Fig. 3.3. The incident TEM beam has unit amplitude components of both the $\hat{\mathbf{a}}_\mathbf{x}$ and $\hat{\mathbf{a}}_\mathbf{y}$ polarizations. This incident wavebeam excites fields within the resonator which consist of a wave beam, $\mathbf{c}_{st} E_{st}^-$, traveling in the $-\hat{\mathbf{a}}_\mathbf{z}$ direction, and a beam, $\acute{\mathbf{c}}_{st} E_{st}^+$, traveling in the $+\hat{\mathbf{a}}_\mathbf{z}$ direction. Since $\mathbf{S_1}$ is a perfect conductor, we can apply the boundary condition $\hat{\mathbf{a}}_\mathbf{z} \times (\mathbf{c}_{st} E_{st}^- + \acute{\mathbf{c}}_{st} E_{st}^+) = 0$ at $z = 0$, and find that $\acute{\mathbf{c}}_{st} = -\mathbf{c}_{st}$. The field $0 < z < D$ is a standing wave and is commonly referred to as the TEM_{stq} resonator mode. The subscripts s and t refer to the transverse mode order along

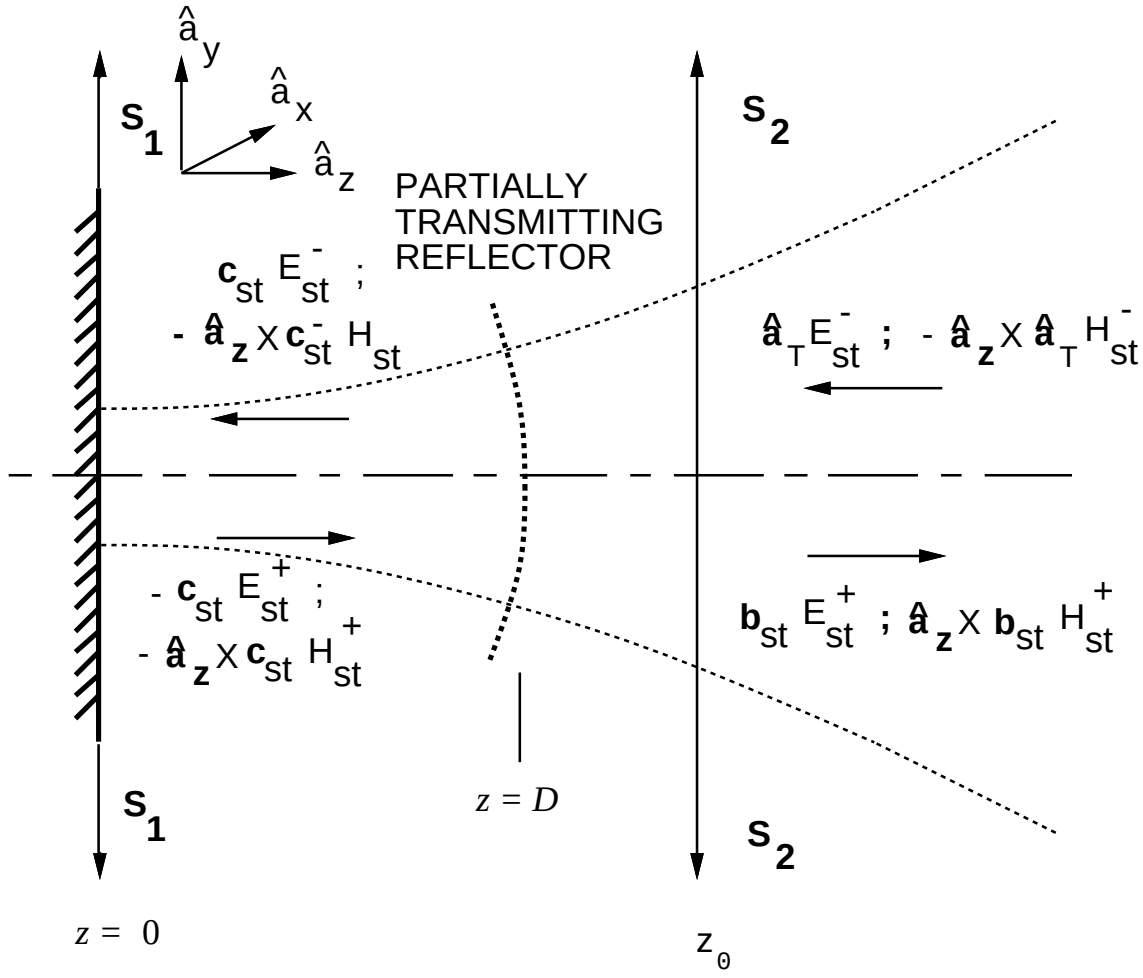

Figure 3.3: Cross-Section of the Quasi-Optical Resonator Showing Modal Test Fields, Where $H_{st}^{\pm} = (\epsilon_0/\mu_0)^{1/2} E_{st}^{\pm}$.

the x- and y-axis , and q is the longitudinal mode number which usually will not be stated explicitly. The incident wavebeam also produces a wave beam traveling in the $+\hat{\mathbf{a}}_\mathbf{z}$ direction for $z > D$. Thus the test field, denoted $\mathbf{E}_{T,st}$, is

$$\mathbf{E}_{T,st} = \begin{cases} \mathbf{c}_{st}(E_{st}^{-} - E_{st}^{+}) & ; \quad 0 < z < D \\ \hat{\mathbf{a}}_T E_{st}^{-} + \mathbf{b}_{st} E_{st}^{+} & ; \quad z > D \end{cases} , \tag{3.18}$$

The coefficient vectors are given by

$$\begin{aligned} \mathbf{c}_{st} &= c_{st}^{(x)}\hat{\mathbf{a}}_{\mathbf{x}} + c_{st}^{(y)}\hat{\mathbf{a}}_{\mathbf{y}} \\ \mathbf{b}_{st} &= b_{st}^{(x)}\hat{\mathbf{a}}_{\mathbf{x}} + b_{st}^{(y)}\hat{\mathbf{a}}_{\mathbf{y}} \\ \hat{\mathbf{a}}_T &= \hat{\mathbf{a}}_{\mathbf{x}} + \hat{\mathbf{a}}_{\mathbf{y}}. \end{aligned} \tag{3.19}$$

The expression for $\mathbf{H}_{T,st}$ can be determined by applying (3.15) to (3.18).

The coefficients $\mathbf{c}_{st}$ and $\mathbf{b}_{st}$ can be determined by application of the boundary conditions at the spherical reflector. Using the transmission and reflection coefficients at the reflector surface,

$$\begin{aligned} \mathbf{c}_{st}E_{st}^{-} &= \hat{\mathbf{a}}_T T_{st} E_{st}^{-} - \mathbf{c}_{st} R_{st} E_{st}^{+} \\ \mathbf{b}_{st}E_{st}^{+} &= \hat{\mathbf{a}}_T R_{st} E_{st}^{-} - \mathbf{c}_{st} T_{st} E_{st}^{+}. \end{aligned} \tag{3.20}$$

Solving for $\mathbf{b}_{st}$ and $\mathbf{c}_{st}$,

$$\mathbf{c}_{st} = \frac{T_{st}\hat{\mathbf{a}}_T}{1 + R_{st}\psi_{st}} \tag{3.21}$$

and

$$\mathbf{b}_{st} = \left(\frac{R_{st}}{\psi_{st}} - \frac{T_{st}^2}{1 + R_{st}\psi_{st}} \right) \hat{\mathbf{a}}_T, \tag{3.22}$$

where $\psi_{st} = E_{st}^{+}/E_{st}^{-}$ is evaluated at the surface of the spherical reflector. Since at $z = D$ the phase fronts of all modes correspond approximately to the surface of the spherical reflector [51], ψ_{st} can be evaluated at $\{x, y, z\} = \{0, 0, D\}$.

Next, the form of the fields $\mathbf{E}_S$ and $\mathbf{H}_S$, which are excited by a source current density $\mathbf{J}_S$, must be specified. For simplification, $\mathbf{J}_S$ is assumed to be contained in the $z = d$ plane and to have transverse components only. The result of this derivation may be applied to any three dimensional current distribution within the cavity provided that the wavebeam phase fronts are approximately planar at the location of $\mathbf{J}_S$. Note that under this approximation, axial components of $\mathbf{J}_S$ cannot

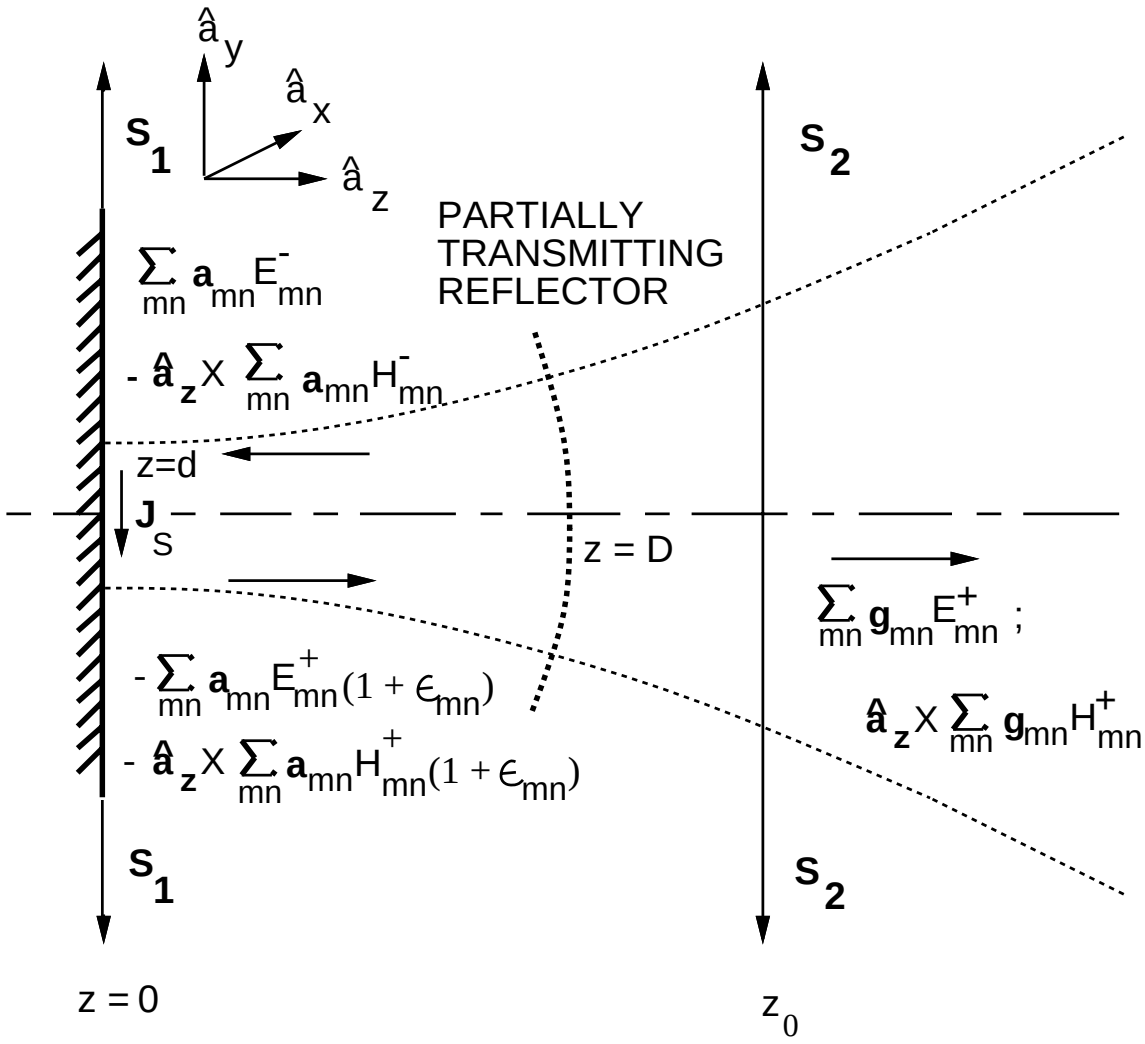

Figure 3.4: Cross-Section of Quasi–Optical Resonator Showing Fields, $\mathbf{E_S}$, Established by the Source Current $\mathbf{J_S}$.

couple into the cavity mode structure. If this approximation is invalid, the oblate-spheroidal coordinate system would be more appropriate than Cartesian coordinates. Since the beam modes form a complete ortho–normal set, we can expand these source fields in terms of beam modes as shown in Fig. 3.4. Due to the boundary condition at $z = 0$, the field must be a standing wave in the region $0 \leq z < d$. The field in the region $d < z \leq D$ is has both a modal standing wave component and a traveling wavebeam component. The $+\hat{\mathbf{a}}_\mathbf{z}$ directed traveling wavebeam component accounts for the power which is transmitted through the spherical reflector and then radiates out into the region $z > D$. The magnetic field is found from the electric field using (3.15). The electric field excited by $\mathbf{J}_S$ is expressed as

$$\mathbf{E}_S = \sum_{mn} \begin{cases} \mathbf{f}_{mn}(E^-_{mn} - E^+_{mn}) & ; \ 0 \leq z < d \\ \mathbf{a}_{mn}(E^-_{mn} - (1+\varepsilon_{mn})E^+_{mn}) & ; \ d < z \leq D \\ \mathbf{g}_{mn}E^+_{mn} & ; \ z > D \end{cases} . \tag{3.23}$$

The coefficient vectors are defined by

$$\begin{aligned} \mathbf{f}_{mn} &= f^{(x)}_{mn}\hat{\mathbf{a}}_x + f^{(y)}_{mn}\hat{\mathbf{a}}_y \\ \mathbf{a}_{mn} &= a^{(x)}_{mn}\hat{\mathbf{a}}_x + a^{(y)}_{mn}\hat{\mathbf{a}}_y \\ \mathbf{g}_{mn} &= g^{(x)}_{mn}\hat{\mathbf{a}}_x + g^{(y)}_{mn}\hat{\mathbf{a}}_y \end{aligned}$$

Using the boundary conditions at the spherical reflector we can write,

$$\begin{aligned} \mathbf{g}_{mn}E^+_{mn} &= -T_{mn}\mathbf{a}_{mn}(1+\varepsilon_{mn})E^+_{mn} \\ E^-_{mn} &= -R_{mn}(1+\varepsilon_{mn})E^+_{mn} \end{aligned} \tag{3.24}$$

Which allows us to express the coefficients $\mathbf{a}_{mn}$ in terms of $\mathbf{g}_{mn}$ and to solve for ε_{mn}.

$$1 + \varepsilon_{mn} = -\frac{1}{\psi_{mn}R_{mn}} \tag{3.25}$$

and

$$\mathbf{a}_{mn} = \mathbf{g}_{mn}\frac{R_{mn}\psi_{mn}}{T_{mn}}. \tag{3.26}$$

The coefficients $\mathbf{f}_{mn}$ can be related to the coefficients $\mathbf{a}_{mn}$ by requiring continuity of the field at $z = d$ on a mode by mode basis.

$$\mathbf{f}_{mn}(E^-_{mn} - E^+_{mn}) = \mathbf{a}_{mn}(E^-_{mn} - (1+\varepsilon_{mn})E^+_{mn})$$

applying (3.25)

$$\begin{aligned}
\mathbf{f}_{mn} &= \mathbf{a}_{mn}\frac{(E^-_{mn} - (1+\varepsilon_{mn})E^+_{mn})}{(E^-_{mn} - E^+_{mn})} \\
&= \mathbf{a}_{mn}\frac{(1 - (1+\varepsilon_{mn})\Upsilon_{mn})}{(1 - \Upsilon_{mn})} \\
&= \mathbf{a}_{mn}\frac{(1 + \Upsilon_{mn}/(R_{mn}\psi_{mn})}{(1 - \Upsilon_{mn})}.
\end{aligned} \tag{3.27}$$

Where the ratio $\Upsilon_{mn} \equiv E^+_{mn}/E^-_{mn}$ is evaluated at the plane $z = d$. Near the surface $z = 0$ the wavebeam phase fronts of E^+_{mn} and E^-_{mn} are nearly planar so, for fixed $z = d$, Υ_{mn} is approximately independent of x and y. This is particularly true for practical QR devices in which it is desirable to couple into the TEM_{00q} modes. In this case the radiating elements are placed near the z axis where the wavebeam phase fronts are transverse. Thus we can approximate Υ_{mn} by evaluating E^+_{mn}/E^-_{mn} at $\{x, y, z\} = \{0, 0, d\}$. The unknown coefficients of (3.23) can now be determined using $\mathbf{E}_{T,st}$ and the Lorentz reciprocity theorem.

3.3 Application of Reciprocity Theorem

The general form of the Lorentz reciprocity condition can be derived by considering the independent source currents $\mathbf{J}_a$, $\mathbf{M}_a$ and $\mathbf{J}_b$, $\mathbf{M}_b$ which produce the fields $\mathbf{E}_a$, $\mathbf{H}_a$ and $\mathbf{E}_b$, $\mathbf{H}_b$ in a region $\mathbf{\Omega}$ which is bounded by the closed surface $\mathbf{S}$. For isotropic

media it can be shown that [62]

$$\oint_S (\mathbf{E}_b \times \mathbf{H}_a - \mathbf{E}_a \times \mathbf{H}_b)\cdot\hat{\mathbf{n}} ds = \int_{\mathbf{\Omega}} (\mathbf{E}_a\cdot\mathbf{J}_b - \mathbf{H}_a\cdot\mathbf{M}_b - \mathbf{E}_b\cdot\mathbf{J}_a + \mathbf{H}_b\cdot\mathbf{M}_a) dv \quad (3.28)$$

which is known as the Lorentz integral, and where $\hat{\mathbf{n}}$ is the unit outward normal on $\mathbf{S}$.

The Lorentz integral is now applied over the volume $\mathbf{\Omega}$ which is bounded by the surface $\mathbf{S} = \mathbf{S_1} + \mathbf{S_2}$ shown in Fig. 3.4. $\mathbf{S_1}$ is the inner surface of the infinite planar reflector while $\mathbf{S_2}$ is a transverse plane located at some $z_0 > D$. The source of the test fields, $\mathbf{J}_{T,st}$, is assumed to be located at some $z > z_0$ so that $\mathbf{J}_{T,st} = 0$ in $\mathbf{\Omega}$. Equation (3.28) is applied by assigning

$$\begin{aligned} &\mathbf{E}_{T,st} = \mathbf{E}_b, \quad \mathbf{H}_{T,st} = \mathbf{H}_b, \quad \mathbf{M}_S = \mathbf{M}_a = 0 \\ &\mathbf{E}_S = \mathbf{E}_a, \qquad \mathbf{H}_S = \mathbf{H}_a, \qquad \mathbf{J}_S = \mathbf{J}_a \\ &\mathbf{J}_T = \mathbf{J}_b, \qquad \mathbf{M}_T = 0, \qquad \mathbf{M}_b = 0 \end{aligned} \quad (3.29)$$

which results in

$$\oint_S (\mathbf{E}_{T,st}\times\mathbf{H}_S - \mathbf{E}_S\times\mathbf{H}_{T,st})\cdot\hat{\mathbf{n}} ds = -\int_{\mathbf{\Omega}} \mathbf{E}_{T,st}\cdot\mathbf{J}_S dv. \quad (3.30)$$

Since $\hat{\mathbf{a}}_z\times\mathbf{E} = 0$ on the perfectly conducting plane, the surface integral on $\mathbf{S_1}$ vanishes. Substituting from (3.18), (3.23), and using (3.15), Eqn. 3.30 can be written

$$\sum_{mn} \int_{\mathbf{S_2}} \left[(\hat{\mathbf{a}}_T E^-_{st} + \mathbf{b}_{st} E^+_{st})\times(E^+_{mn}\hat{\mathbf{a}}_z\times\mathbf{g}_{mn}) + (E^+_{mn}\mathbf{g}_{mn})\times(E^-_{st}\hat{\mathbf{a}}_z\times\hat{\mathbf{a}}_T - E^+_{st}\hat{\mathbf{a}}_z\times\mathbf{b}_{st})\right]\cdot\hat{\mathbf{a}}_z dx\, dy$$

$$= -\sqrt{\frac{\epsilon}{\mu}} \int_{\mathbf{\Omega}} \mathbf{c}_{st}(E^-_{st} - E^+_{st})\cdot\mathbf{J}_S dv. \quad (3.31)$$

Consider the following terms from the left side of (3.31).

$$E^+_{st}E^+_{mn}\mathbf{b}_{st}\times(\hat{\mathbf{a}}_z\times\mathbf{g}_{mn}) - E^+_{mn}E^+_{st}\mathbf{g}_{mn}\times(\hat{\mathbf{a}}_z\times\mathbf{b}_{st})$$

Using the vector identity $\mathbf{A} \times (\mathbf{B} \times \mathbf{C}) = (\mathbf{A} \cdot \mathbf{C})\mathbf{B} - (\mathbf{A} \cdot \mathbf{B})\mathbf{C}$, it is clear that each term is equal to $(\mathbf{b}_{st} \cdot \mathbf{g}_{mn})\hat{\mathbf{a}}_z$ because $\mathbf{b}_{st} \cdot \hat{\mathbf{a}}_z = \mathbf{g}_{mn} \cdot \hat{\mathbf{a}}_z = 0$, thus these terms cancel. The remaining two terms each contain the factor $E^+_{mn} E^-_{st}$ so the orthogonality relation (3.16) can be applied. Using (3.16), (3.21), and the same vector identity, (3.31) simplifies to

$$2\hat{\mathbf{a}}_T \cdot \mathbf{g}_{mn} = -\frac{T_{mn}}{(1 + R_{mn}\psi_{mn})} \int_{\mathbf{\Omega}} (E^-_{mn} - E^+_{mn}) \hat{\mathbf{a}}_T \cdot \mathbf{J}_S dv \tag{3.32}$$

Since the polarization of the modal electric field will be in the same direction as the source current, (3.32) can be rewritten for general three dimensional current distributions as

$$\mathbf{g}_{mn} = \frac{T_{mn}}{2(1 + R_{mn}\psi_{mn})} \int_{\mathbf{\Omega}} (E^+_{mn} - E^-_{mn}) \bar{\mathbf{I}}_T \cdot \mathbf{J}_s dV \tag{3.33}$$

where $\bar{\mathbf{I}}_T = \hat{\mathbf{a}}_x \hat{\mathbf{a}}_x + \hat{\mathbf{a}}_y \hat{\mathbf{a}}_y$.

This fully specifies the coupling between an electric source current density and the cavity modal fields.

3.4 Dyadic Green's Function for Electric Source Currents

3.4.1 Resonant Field Contribution

The cavity resonant fields excited by $\mathbf{J}_S$ are expressed by combining (3.23), (3.24), (3.25), (3.27), and (3.33).

$$\mathbf{E}_S = \sum_{mn} \left[\frac{\int_{\mathbf{\Omega}} (E^+_{mn} - E^-_{mn}) \bar{\mathbf{I}}_T \cdot \mathbf{J}_S dv}{2(1 + R_{mn}\psi_{mn})} \left\{ \begin{array}{ll} \frac{R_{mn}\psi_{mn} + \Upsilon_{mn}}{1 - \Upsilon_{mn}} (E^-_{mn} - E^+_{mn}), & 0 \le z < d \\ (\psi_{mn} R_{mn} E^-_{mn} + E^+_{mn}), & d < z \le D \\ T_{mn} E^+_{mn}, & D < z \end{array} \right. \right] \tag{3.34}$$

The dyadic resonant Green's function can be written by comparing (3.1) and (3.34)

$$\bar{\mathbf{G}} e_r = \sum_{mn} \left[\frac{(\acute{E}^+_{mn} - \acute{E}^-_{mn}) \bar{\mathbf{I}}_T}{2(1 + R_{mn}\psi_{mn})} \left\{ \begin{array}{ll} \frac{R_{mn}\psi_{mn} + \Upsilon_{mn}}{1 - \Upsilon_{mn}} (E^-_{mn} - E^+_{mn}), & 0 \le z \le d \\ (\psi_{mn} R_{mn} E^-_{mn} + E^+_{mn}), & d < z \le D \\ T_{mn} E^+_{mn}, & D < z \end{array} \right. \right] \tag{3.35}$$

where $\acute{E}^{\pm}_{mn}$ is a function of the source coordinate system $\acute{\mathbf{r}} = \{\acute{x}, \acute{y}, \acute{z}\}$, and $E^{\pm}_{mn}$ is a function of the observation coordinate system $\mathbf{r} = \{x, y, z\}$.

Examination of (3.35) reveals that the denominator expression $(1 + R_{mn}\psi_{mn})$ accounts for the resonance behavior of the cavity through the phase term ψ_{mn}. This term is complex with $|\psi_{mn}| = 1$. If the spherical reflector is an electric wall, at resonance $\psi_{mn} = 1$, for a magnetic wall resonance occurs when $\psi_{mn} = -1$. For real physical reflectors $|R_{mn}| < 1$, thus reflector loss is included in $\bar{\mathbf{G}}\mathbf{e}_c$.

Consider an outgoing wavebeam in the cavity starting at $z = 0$ and undergoing a round trip through the cavity. This diverging wavebeam travels to $z = D$ where some power is transmitted through the spherical reflector, some power is lost in the reflector, and some power is reflected back into the cavity in the form of a converging wavebeam. This converging wavebeam propagates back to $z = 0$ where it is reflected by the planar reflector and is transformed back into an outgoing diverging wavebeam. In a physical resonator, some power is lost in the reflection

at the planar reflector due to its finite conductivity. To account for power loss in the planar reflector, consider a converging wavebeam of power P^- and a reflected diverging wavebeam of power P^+, define $R_p = \sqrt{P^+/P^-}$. This loss can then be included in $\bar{\mathbf{G}}\mathbf{e}_c$ by replacing R_{mn} in the resonance denominator expression with the term $R_{mn}R_p$.

Even a resonator having perfect lossless reflectors would have a finite Q due to diffraction losses. Modes of higher transverse order number will have smaller values of Q due to the larger transverse extent of their field patterns. Diffraction losses can be described on a round-trip basis similar to reflector losses. Just as $|R_{mn}R_p|^2$ describe the fraction of energy remaining in a wavebeam after making one round trip through the resonator and undergoing reflector losses, $|\chi_m\chi_n|^2$ can be interpreted as the fraction of power remaining after a round trip through a resonator after diffraction losses. χ_m and χ_n are each derived for a single transit in cylindrical strip reflector cavity such as in Fig. 3.1. A single transit in this system is equivalent to a round trip in the resonator of Fig. 2.3. Diffraction effects are included in the resonance denominator by perturbing the value of the reflection coefficient, R_{mn} is replaced by $R_{mn}R_p|\chi_m\chi_n|$.

The values of χ_m and χ_n can be calculated by modifying the method used by Soohoo [53]. The first order integral equations may each be interpreted as representing an infinite strip cylindrical resonator. For each of the strip resonators, define $c_x = \pi a_x^2/(D\lambda)$ and $c_y = \pi a_y^2/(D\lambda)$. In finding the eigenvalues, c_x is used with $R_x = 2F_x$ to compute χ_m, and c_y is used with $R_y = 2F_y$ to compute χ_n. Thus the method of Soohoo has been adapted for to solve for the eigenvalues of a plano-concave resonator having a bicylindrical lens with a rectangular aperture.

3.4.2 Nonresonant Field Contribution

The cavity resonant Green's function $\bar{\mathbf{G}}\mathbf{e}_r$ as derived in the previous section describes the coupling between an electric current density and the cavity modal fields. In the derivation of the traveling wavebeams, far field radiation was assumed as well as paraxial propagation. In the absence of the curved reflector, these fields would comprise radiating fields which diverge from the z axis by a small angle. In general, a current distribution located over a ground plane will produce some nonparaxial radiation as well as near field components which have intensity that decreases faster than $1/r$. This situation is depicted in Fig. 3.5.

These nonresonant field terms, $\bar{\mathbf{G}}\mathbf{e}_n$, must be added to $\bar{\mathbf{G}}\mathbf{e}_r$ to produce the complete cavity Green's function, $\bar{\mathbf{G}}\mathbf{e}_c$.

$$\bar{\mathbf{G}}\mathbf{e}_c = \bar{\mathbf{G}}\mathbf{e}_r + \bar{\mathbf{G}}\mathbf{e}_n \tag{3.36}$$

Knowledge of all fields produced by the current distribution is necessary, if, for example one wishes to use $\bar{\mathbf{G}}\mathbf{e}_c$ to determine the driving point impedance of an antenna within the cavity.

$\bar{\mathbf{G}}e_n$, is derived by assuming that the non-resonant component of the field near the plane $z = d$ and close to the z axis is essentially unchanged if the spherical reflector is removed. This assumption is justifiable because much of the radiating nonparaxial energy falls outside the spherical reflector aperture, also most of the nonparaxial energy that impinges on the spherical reflector diverges from the z axis after reflection and does not return to the region of the source current. Also, the amount of energy reflected back to the source due to the near field terms is negligible because the reflectors are assumed to be in each other's far field.

If the spherical reflector is removed then a half-space remains which is bounded by the perfectly conducting planar reflector. The field components that comprised the cavity modal fields become, in the half space, radiating paraxial wavebeams. These fields will be described by a paraxial Green's function $\bar{\mathbf{G}}\mathbf{e}_p$. Which can be found mathematically from (3.35) using

$$\bar{\mathbf{G}}e_p = \lim_{\substack{R_{mn} \to 0 \\ T_{mn} \to 1}} \bar{\mathbf{G}}e_r$$

$$= -\frac{\bar{\mathbf{I}}_{\mathbf{T}}}{2} \sum_{mn} (\acute{E}^-_{mn} - \acute{E}^+_{mn}) \begin{cases} \frac{\Upsilon_{mn}}{1-\Upsilon_{mn}} (E^-_{mn} - E^+_{mn}), & 0 \le z < d \\ E^+_{mn} & d \le z \end{cases} \tag{3.37}$$

Figure 3.5: The Various Field Components Excited by a Current Element Over a Ground Plane.

The dyadic Green's function for this half-space is known to be [63]

$$\frac{\bar{\mathbf{G}}e_h}{j\omega\mu_0} = \left(\bar{\mathbf{I}} - \frac{\nabla\acute{\nabla}}{k_0^2}\right)(G_0(\mathbf{r};\acute{\mathbf{r}}) - G_0(\mathbf{r};\acute{\mathbf{r}} - 2\acute{z}\hat{\mathbf{a}}_z)) + 2G_0(\mathbf{r};\acute{\mathbf{r}} - 2\acute{z}\hat{\mathbf{a}}_z)\hat{\mathbf{a}}_z\hat{\mathbf{a}}_z \quad (3.38)$$

where

$$G_0(\mathbf{r};\acute{\mathbf{r}}) = \frac{\exp(jk_0|\mathbf{r} - \acute{\mathbf{r}}|)}{4\pi|\mathbf{r} - \acute{\mathbf{r}}|},$$

and

$$\bar{\mathbf{I}} = \hat{\mathbf{a}}_x\hat{\mathbf{a}}_x + \hat{\mathbf{a}}_y\hat{\mathbf{a}}_y + \hat{\mathbf{a}}_z\hat{\mathbf{a}}_z.$$

$\bar{\mathbf{G}}e_h$ represents all the field components generated by an electric source current density in the half space, specifically traveling paraxial wavebeams , nonparaxial fields, and nonradiating fields are represented. A Green's function, $\bar{\mathbf{G}}\mathbf{e}_n$, which represents the nonresonant terms can be found by removing the paraxial component of $\bar{\mathbf{G}}\mathbf{e}_h$.

$$\bar{\mathbf{G}}e_n = \bar{\mathbf{G}}e_h - \bar{\mathbf{G}}e_p \quad (3.39)$$

Finally, the complete Green's function for the interior of the cavity is found by using (3.36).

$$\bar{\mathbf{G}}\mathbf{e}_c = \bar{\mathbf{G}}\mathbf{e}_r + \bar{\mathbf{G}}\mathbf{e}_n = \bar{\mathbf{G}}\mathbf{e}_h + \bar{\mathbf{G}}\mathbf{e}_r - \bar{\mathbf{G}}\mathbf{e}_p$$

$$= \bar{\mathbf{G}}\mathbf{e}_h - \sum_{mn}\frac{R_{mn}\psi_{mn}}{2(1 + R_{mn}\psi_{mn})}(E_{mn}^- - E_{mn}^+)(\acute{E}_{mn}^- - \acute{E}_{mn}^+)\bar{\mathbf{I}}_t \ , \ 0 < z < D \quad (3.40)$$

Equation (3.40) is symmetrical under exchange of coordinate systems $\mathbf{r}$ and $\mathbf{r}'$ as is required of electric field Green's functions for the wave equation and most common boundary conditions [63]. Furthermore

$$\lim_{R_{mn}\to 0}\bar{\mathbf{G}}\mathbf{e}_c = \bar{\mathbf{G}}\mathbf{e}_h$$

as is expected.

3.5 Dyadic Green's Function for Magnetic Source Currents

Equation 3.40 completely describes the fields induced by an electric current density within the cavity. For situations in which energy is coupled into the resonator by apertures, it is convenient to a Green's function, $\bar{\mathbf{G}}\mathbf{h}_c$, for magnetic source currents $\mathbf{M_S}$. If both $\mathbf{J_S}$ and $\mathbf{M_S}$ are present, the fields are found by superposition as indicated in Eqn. 3.1.

The derivation of resonant part of $\bar{\mathbf{G}}\mathbf{h}_c$, termed $\bar{\mathbf{G}}\mathbf{h}_r$, follows the same procedure as was used to obtain $\bar{\mathbf{G}}\mathbf{e}_r$. Using the assignments

$$\begin{aligned} &\mathbf{E}_{T,st} = \mathbf{E}_b, \quad \mathbf{H}_{T,st} = \mathbf{H}_b, \quad \mathbf{J}_S = \mathbf{J}_a = 0 \\ &\mathbf{E}_S = \mathbf{E}_a, \qquad \mathbf{H}_S = \mathbf{H}_a, \qquad \mathbf{M}_S = \mathbf{M}_a \\ &\mathbf{J}_T = \mathbf{J}_b, \qquad\qquad\qquad\quad \mathbf{M}_T = \mathbf{M}_b = 0 \end{aligned} \tag{3.41}$$

in (3.30), the right hand side of (3.31) becomes

$$-\frac{\epsilon}{\mu}\int_{\mathbf{\Omega}} \hat{\mathbf{a}}_z \times \mathbf{c}_{st} \cdot \mathbf{M_S}(E^-_{st} + E^+_{st})dv. \tag{3.42}$$

Continuing as before (3.32) becomes

$$2\hat{\mathbf{a}}_T \cdot \mathbf{g}_{mn} = -\sqrt{\frac{\epsilon}{\mu}}\frac{T_{mn}}{1 + R_{mn}\psi_{mn}}\int_{\mathbf{\Omega}} \hat{\mathbf{a}}_z \times \hat{\mathbf{a}}_T \cdot \mathbf{M_S}(E^-_{mn} + E^+_{mn})dv. \tag{3.43}$$

Since $\hat{\mathbf{a}}_z \times \mathbf{c}_{st} = c^x_{st}\hat{\mathbf{a}}_y - c^y_{st}\hat{\mathbf{a}}_x$, from (3.42) we can see that the $\hat{\mathbf{a}}_x$ directed component of $\mathbf{M_S}$ produces $\hat{\mathbf{a}}_y$ polarized E and that the $\hat{\mathbf{a}}_y$ directed component of $\mathbf{M_S}$ produces $\hat{\mathbf{a}}_x$ polarized E. Due to this, (3.43) can be written as

$$\mathbf{g}_{mn} = -\frac{1}{2}\sqrt{\frac{\epsilon}{\mu}}\frac{T_{mn}}{1 + R_{mn}\psi_{mn}}\int_{\mathbf{\Omega}} \hat{\mathbf{a}}_z \times \bar{\mathbf{I}}_T \cdot \mathbf{M_S}(E^-_{mn} + E^+_{mn})dv. \tag{3.44}$$

Which leads to the modal cavity Green's function for magnetic source current

$$\bar{\mathbf{G}}\mathbf{h}_r = \sqrt{\frac{\epsilon}{\mu}} \sum_{mn} \left[\frac{(\acute{E}^+_{mn} + \acute{E}^-_{mn})\hat{\mathbf{a}}_z \times \bar{\mathbf{I}}_T}{2(1 + R_{mn}\psi_{mn})} \begin{cases} \frac{R_{mn}\psi_{mn} + \Upsilon_{mn}}{1 - \Upsilon_{mn}}(E^-_{mn} - E^+_{mn}), & 0 \le z < d \\ (\psi_{mn} R_{mn} E^-_{mn} + E^+_{mn}), & d < z \le D \\ T_{mn} E^+_{mn}, & D < z \end{cases} \right] \tag{3.45}$$

The quantity $\bar{\mathbf{G}}\mathbf{h}_r - \bar{\mathbf{G}}\mathbf{h}_p$, for regions inside the cavity, is found to be

$$\bar{\mathbf{G}}\mathbf{h}_r - \bar{\mathbf{G}}\mathbf{h}_p = \bar{\mathbf{G}}\mathbf{h}_r - \lim_{\substack{R_{mn} \to 0 \\ T_{mn} \to 1}} \bar{\mathbf{G}}\mathbf{h}_r$$

$$= \sqrt{\frac{\epsilon}{\mu}} \sum_{mn} \left[\frac{1}{2}(\acute{E}^+_{mn} + \acute{E}^-_{mn})\hat{\mathbf{a}}_z \times \bar{\mathbf{I}}_T \frac{R_{mn}\psi_{mn}}{1 + R_{mn}\psi_{mn}}(E^-_{mn} - E^+_{mn}) \right], \ 0 \le z \le D \tag{3.46}$$

The complete cavity Green's function for magnetic source current is

$$\bar{\mathbf{G}}\mathbf{h}_c = \bar{\mathbf{G}}\mathbf{h}_h + \bar{\mathbf{G}}\mathbf{h}_r - \bar{\mathbf{G}}\mathbf{h}_p. \tag{3.47}$$

This Green's function is not symmetrical to exchange of $\mathbf{r}$ and $\mathbf{r}'$. It can be shown that a Green's function for the electric field in terms of a magnetic source current need not be symmetrical. For a free-space region containing magnetic or electric source currents the following are true;

$$\nabla \times \nabla \times \mathbf{E} - k^2 \mathbf{E} = i\omega\mu_0 \mathbf{J} \tag{3.48}$$

$$\nabla \times \nabla \times \mathbf{H} - k^2 \mathbf{H} == k^2 \mathbf{M} \tag{3.49}$$

$$\nabla \times \mathbf{H} = -i\omega\epsilon_0 \mathbf{E}, \ \ \mathbf{j} = 0. \tag{3.50}$$

Symmetry is required for a valid Green's function which relates electric field to electric source current [63]. By comparing the differential operators in (3.48) and

(3.49) it is obvious that a Green's function relating **H** and **M** must similarly be symmetrical under exchange of **r** and **r′**. **E** can be determined from **M** by first finding **H** excited by **M** and then applying (3.50). Since the relation (3.50) calls for operation on the **r** coordinate system alone, the resulting expression is not expected to be symmetrical under exchange of **r** and **r′**.

The half space Green's function for magnetic source current, $\hat{\mathbf{G}}\mathbf{h}_h$, can be derived using the auxiliary potential function $\mathbf{A}_M$ along with image theory. Alternatively, the half space fields can be calculated directly by application of potential theory. The potential function is defined [40]

$$\mathbf{A}_M = \oint_S \frac{\epsilon \mathbf{M}_S}{4\pi R} \exp(-ikR) da,$$

and the fields are found using

$$\begin{aligned} \epsilon \mathbf{E} &= -\nabla \times \mathbf{A}_M \\ \mathbf{H} &= -i\omega \mathbf{A}_M + \tfrac{\nabla \nabla \cdot \mathbf{A}_M}{i\omega\epsilon\mu}. \end{aligned} \tag{3.51}$$

The conducting plane is removed and replaced with the image of the magnetic current which has the same transverse polarity as the source magnetic current and the opposite longitudinal polarity. This calculation results in a formula for $\hat{\mathbf{G}}\mathbf{h}_n$.

Chapter 4

Application of Green's Functions to Quasi-Optical Systems

4.1 Impedance Matrix of an Array of Small Antennas

The driving point impedance matrix for an array of small electric dipoles within the cavity is determined. The result of this calculation is a multiport impedance which models the antenna array and the cavity. This model can be used in the design and analysis of power combiners or, in general, for design of structures which couple into Gaussian optical systems. This analysis was performed for short inverted-L antennas as shown in Fig. 4.1. Each antenna consists of a semirigid coaxial feed which penetrates a cylindrical copper ferrule. The coaxial outer conductor is cut flush with the surface of the ferrule and soldered to it. The inner conductor forms the radiating structure which is bent parallel to the face of the ferrule. The sides of the ferrule are threaded to fit tapped holes in the resonator planar reflector. The ferrule and antenna assembly is screwed into the resonator planar reflector until the ferrule surface is flush with the reflector inner surface.

4.1.1 Resonator Characterization

A resonator was designed, constructed, and then used in an experimental verification of theoretical Green's function calculations. The resonator geometry was designed

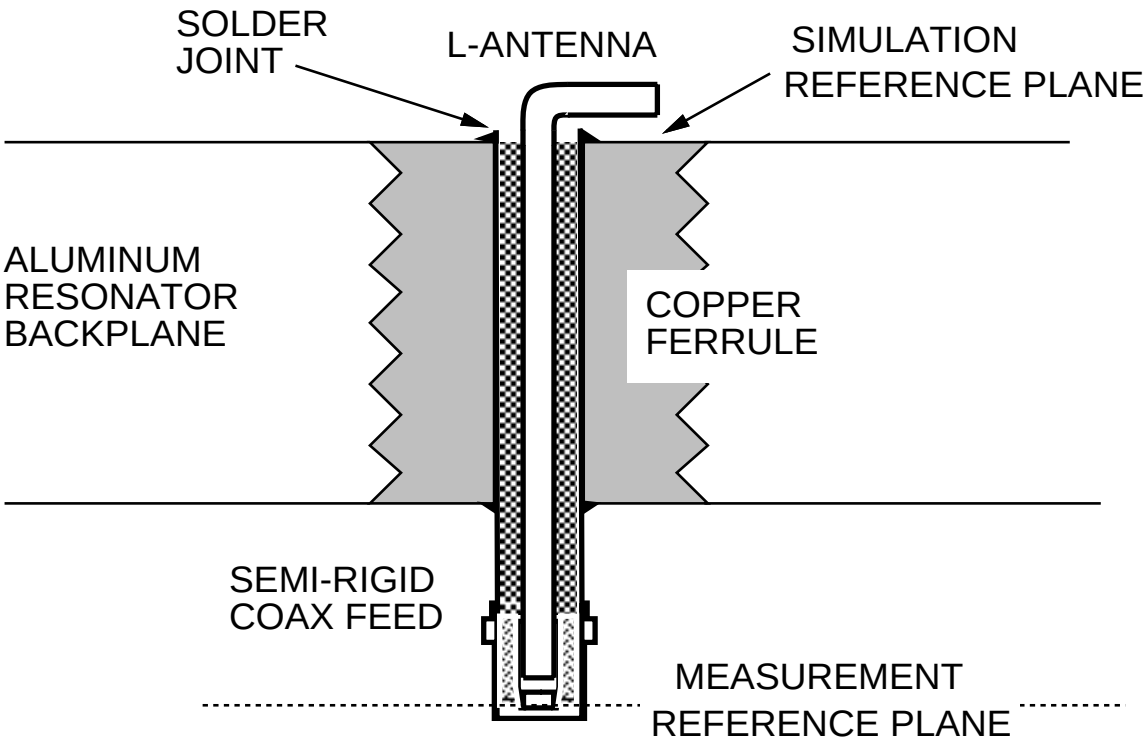

Figure 4.1: The Inverted-L Type Antenna.

for experiments at X-band frequencies which allowed the use of an HP 8510B network analyzer for measurements.

The reflectors of the plano-concave resonator were fabricated from 6061 T6 aluminum. The spherical reflector was placed in a mount which permitted the reflector axis to be adjusted in a horizontal plane. The spherical reflector has a 183 cm radius of curvature and a circular aperture with a 25.4 cm aperture radius. The planar reflector is mounted on a translation table allowing longitudinal and transverse positioning. The rectangular aperture dimensions of the planar reflector are $a_x = 33$ cm, $a_y = 32$ cm. Measurements were taken using a reflector spacing of $D = 62.1$ cm. This resonator is similar to one having two identical spherical reflectors with spacing $2D$ and numerical aperture $c = \pi a^2/D\lambda = 9.25$ at 8.5 GHz. This spacing corresponds to approximately 2/3 of the semiconfocal spacing for the 91.5 cm focal length of the spherical reflector. Preliminary electrical measurements of the resonator indicated less than ideal behavior. These nonidealities are characterized and included in $\bar{\mathbf{G}}\mathbf{e}_c$ so that the model more closely represents the physical resonator.

The physical construction of the resonator should result in Laguerre-Gaussian modes since nearly all diffraction losses occur at the spherical reflector which has a circular aperture. The major diffraction losses occur at the spherical reflector because the beam spot-size is larger on the spherical reflector than it is on the planar reflector and the spherical reflector also has a smaller aperture size. Thus the resulting boundary conditions have cylindrical symmetry and Laguerre-Gaussian modes are expected. Measurements of the planar reflector show that it is distorted. Along the x-axis the reflector is seen to be concave with a .23 mm dip in 61 cm. A convex crown of .20 mm in 35 cm was measured along the y-axis. This distortion has approximate rectangular symmetry and apparently disturbs the resonator cylindrical symmetry, resulting in the experimentally observed Hermite-Gaussian modes. The

distortion was not sufficiently uniform to be characterized through use of mechanical measurements.

The affect of the warped planar reflector on the resonance spectrum can be examined by considering the phase term of (3.14). At resonance, the phase of a traveling beam mode should be unchanged after one round-trip through the resonator. Thus, if the phase change for a half-trip is $q\pi$, for some integer q, then resonance will occur. These resonant frequencies are then

$$f_{mnq} = \frac{c}{2D}\left[q + \frac{1}{\pi}(m+\frac{1}{2})\arctan\sqrt{\frac{D}{2F_x - D}} + \frac{1}{\pi}(n+\frac{1}{2})\arctan\sqrt{\frac{D}{2F_y - D}}\ \right], \tag{4.1}$$

where c is the speed of light and q, the longitudinal mode number corresponds to an integer number of longitudinal half waves.

Equation (4.1) predicts families of resonances with each family corresponding to a particular q and having members consisting of resonances with different transverse mode numbers m and n. Each family is offset from the next by $\Delta f_q = c/(2D)$. Within each family the value of Q decreases with increasing transverse mode order because the beam diameter is larger for higher order modes so they suffer greater diffraction losses. If $F_x = F_y$, then in each family all modes with $m + n =$ constant are degenerate. Observed resonances for the experimental cavity did not show this degeneracy. In fact the mode spacing corresponds to a resonator with $F_x = 89.4$ cm and $F_y = 95.3$ cm. When compared with the nominal focal length of the spherical reflector, 91.4 cm, we see that, as expected, the concavity of the planar reflector along the x-axis decreases the effective x focal length of the spherical reflector and the convex shape along the y-axis increases the effective y focal length. These effective focal lengths are used in simulation, thus the distortion of the planar reflector is modeled by slight changes in curvature of the spherical reflector while assuming

that the planar reflector is ideal.

No provisions were made in the experimental apparatus for precise alignment of the reflectors. Since the spherical reflector has no axis, the z-axis of the resonator is defined to be a line normal to the planar reflector which intersects the center of the face of the spherical reflector. It can be seen that tilting of the mirrors will effect the location of the coordinate system origin, i.e. the z-axis intersection with the face of the planar reflector (and thus the location of the antennas). Also, since it is the distortion of the planar reflector which causes the rectangular mode structure, the orientation and origin of the transverse axes (x-y) is unknown. It cannot be assumed that the transverse axes necessarily align with edges of the planar reflector.

The approximate location of the z-axis and the orientation of the transverse axes were determined by measurement. The cavity was fed through the planar reflector at a position $x = 2.7$cm $y = 1.7cm$ by a short inverted-L antenna of height 1.9 mm, length 2.6 mm, and using $\hat{\mathbf{a}}_\mathbf{x}$ polarization. The spatial distribution of the resonant fields was mapped by studying changes in the uncalibrated reflection coefficient of the antenna as a function of the position of a small sphere of lossy dielectric located in the $z = 40$mm plane. Spatial measurements of field strength were taken at frequencies near the modal resonances. By this method, the resonant modal field distribution in the plane $z = 40$mm was determined from antenna reflection coefficient measurements.

We can see that a change in the observed cavity reflection coefficient is proportional to the field strength at the location of the dielectric sphere. We need to show that the magnitude of the antenna resonant driving point impedance is proportional to the magnitude of the cavity resonant field strength for a given antenna current. It is assumed that the lossy sphere attenuates the field pattern in proportion to the field strength at its location, so changes in resonant impedance are proportional to

the field strength at the location of the sphere. What remains to be shown is that changes in the reflection coefficient are proportional to changes in the driving point impedance, and thus to field strength at the sphere.

$$S_{11} = \frac{Z - Z_0}{Z + Z_0} \tag{4.2}$$

where Z_0 is the network analyzer reference impedance, and Z is the driving point impedance of the antenna. If $S_{11}^{(1)}$ is the reflection coefficient before the dielectric is placed in the cavity when $Z = Z_1$, and $S_{11}^{(2)}$ is the reflection coefficient when the sphere is in the field when $Z = Z_2$,

$$\Delta S_{11} = S_{11}^{(2)} - S_{11}^{(1)} = \frac{2Z_0(Z_2 - Z_1)}{Z_1 Z_2 + Z_0^2 + Z_0(Z_2 + Z_1)} \tag{4.3}$$

Defining $Z = Z_2$, $Z_1 = Z - \Delta Z$, and assuming that $|Z + Z_0| >> |\Delta Z|$, we have

$$\Delta S_{11} \approx Z_0 \frac{2\Delta Z}{(Z + Z_0)^2}. \tag{4.4}$$

Which is the desired result showing for a lossy dielectric sphere placed at $\{x_0, y_0, z_0\}$ that $\Delta S_{11} \propto \Delta Z \propto |\mathbf{E}(x_0, y_0, z_0)|$.

Data for the TEM_{00} and TEM_{10} modes is shown in Figs. 4.2 and 4.3 which consist of 10 rows each containing 57 sample points. The axes scales indicate the data point number, the actual dimensions of the scans are 25.5 cm $\times$ 13.0 cm. These plots were used to determine the approximate location of the axes origin and its orientation. Variations in the field profile from that expected by theory in the vicinity of the point $\{37,\ 6.8\}$ are thought to be due to near field effects of the antenna which is at that point.

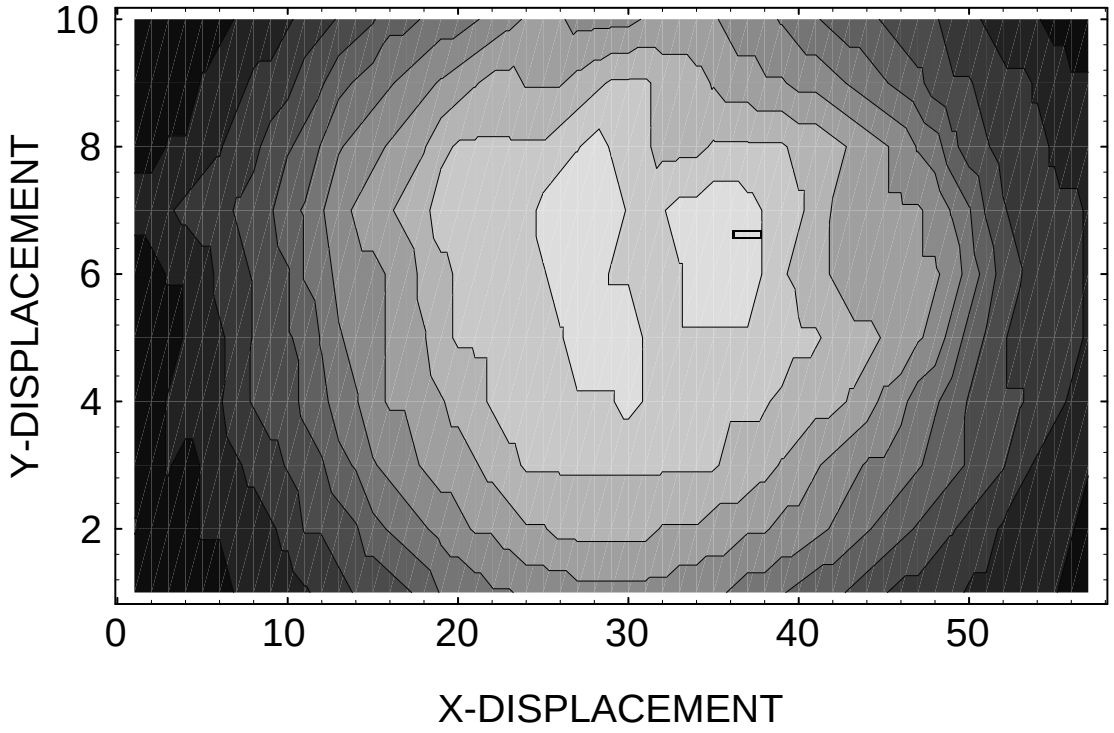

Figure 4.2: Measured Relative Field Strength for the $TEM_{0,0,35}$ Mode, Antenna Location and Orientation Are Indicated. Sample Spacing is 4.6 mm and 14.4 mm in the x and y Directions.

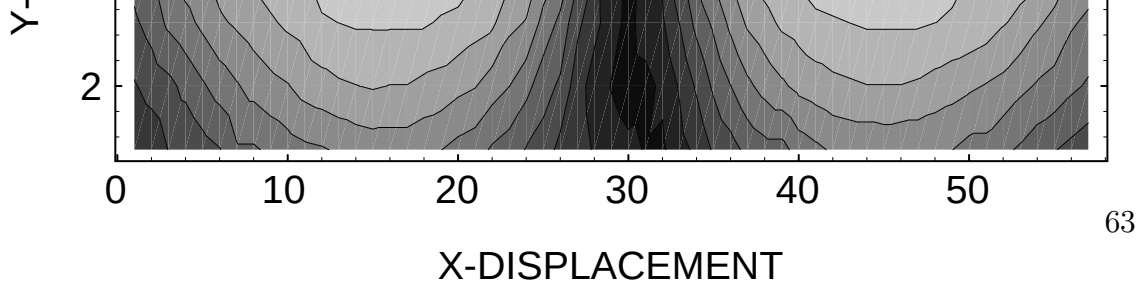

Figure 4.3: Measured Relative Field Strength for the $TEM_{1,0,35}$ Mode, Antenna Location and Orientation Are Indicated. Sample Spacing is 4.6 mm and 14.4 mm in the x and y Directions.

The bottom scans (y=1) of Figs. 4.2 and 4.3 were normalized so that the maximum of the TEM_{00} mode was unity. This data is compared with the a calculated field intensity at the same location in Fig. 4.4. The theoretical field intensity was determined by assuming that the antenna current density was a point source $\delta(x-x_0)\delta(y-y_0)\delta(z-z_0)\hat{\mathbf{a}}_\mathbf{x}$ situated at the antenna location. This expression was used in (3.1) with (3.35) to predict the fields. The theoretical fields were also normalized so that the TEM_{00} mode had a unit maximum. We can see that the cavity model provides a good approximation to the actual field profile and relative mode amplitudes. The Hermite-Gaussian functions are seen to over estimate the field strength away from the z axis. This is a known property of the Hermite-Gaussian functions which accurately approximate the field distribution only near the z axis.

Next, a portion of the mode spectrum of the antenna coupled cavity was studied. Frequencies of several modes were recorded, the relative maximum field strength in the plane $z = 0.4$ cm for each mode was determined using the lossy sphere. The theoretical mode spectrum was determined by calculating the resonant frequencies and the maximum the field strength of each mode in the plane $z = 0.4$ cm. Again, $\bar{\mathbf{G}}e_r$ was used assuming a point source, and was then normalized to give the TEM_{00} mode unit amplitude. Figure 4.5 shows good agreement between measured and calculated relative field strengths and resonance frequencies, indicating that the resonator has been successfully characterized.

Examination of cavity measurements showed that conductor losses were higher than those predicted by surface resistance calculations using bulk conductivity for 6061 T6 aluminum. It is expected that the oxide layer, surface roughness and contamination would increase the value of surface resistance above its ideal value. A constant value for conductor losses was selected based upon examination of data and was used in all calculations. A reflection coefficient due to conductor losses of

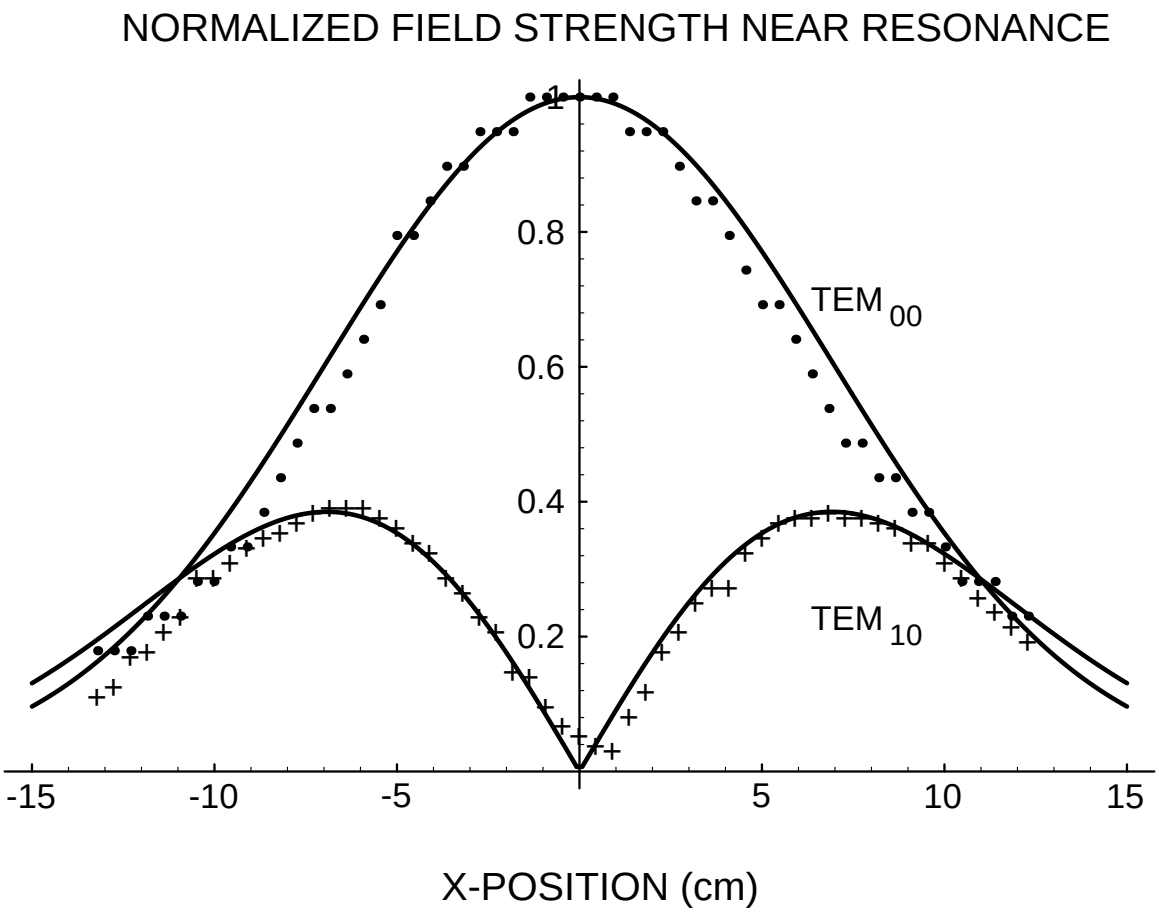

Figure 4.4: Comparison of Theoretical (line) and Measured (points) Modal Field Strength of the TEM_{00} and TEM_{01} Modes Along the Line y=-7.8 cm, z= 4.0 cm.

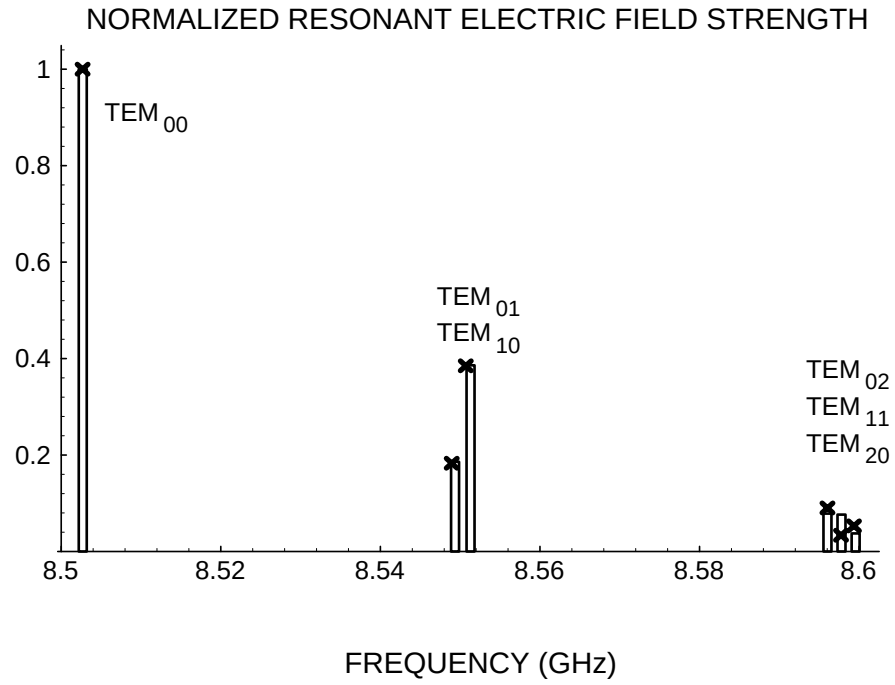

Figure 4.5: Predicted (bar) and Measured (x) Mode Frequencies and Relative Mode Amplitudes for a Plano-Concave Resonator.

-0.9992 was used rather than the theoretical value of -0.9996 at 8.5 GHz which is for two bounces (once on the spherical reflector and once on the planar reflector).

4.1.2 Resonant Coupling Analysis

Using $\bar{\mathbf{G}}\mathbf{e}_c$, a model will be derived for the impedance matrix of an array of short wire antennas radiating into the cavity. Calibrated measurements of an experimental two antenna array will be made over a continuous range of frequencies and then compared with theoretical predictions. The impedance matrix is derived by considering an array of P short wire antennas, each has $\hat{\mathbf{a}}_\mathbf{x}$ polarization, the p th antenna is located at $\{x_p, y_p, d\}$. If we assume that more than one antenna is radiating, the driving point impedance of the qth dipole in the presence of all other dipoles is found by use of a reaction principle [41]

$$Z_q = -\frac{1}{I_q^2}\int_V \mathbf{J}_q \cdot \mathbf{E}_S dV. \tag{4.5}$$

Where $\mathbf{J}_q$ is the current distribution of the q th antenna, I_q is the magnitude of the driving point terminal current, and $\mathbf{E}_S$ is the electric field induced by all radiating antennas. To find $\mathbf{E}_S$, (3.1) is rewritten as

$$\mathbf{E}_c(\mathbf{r}) = \int_{\mathbf{\Omega'}} (\bar{\mathbf{G}}\mathbf{e}_r - \bar{\mathbf{G}}\mathbf{e}_p)\cdot\mathbf{J}_S dv' + \int_{\mathbf{\Omega'}} \bar{\mathbf{G}}\mathbf{e}_h \cdot \mathbf{J}_S dv'. \tag{4.6}$$

The first term on the right of (4.6) describes the strong resonant field component which changes rapidly with frequency. The other term describes the nonresonant field component which changes relatively slowly vs. frequency. The method that is used to calculate impedance (4.5) is incompatible with the nonresonant term because it is undefined for $R \to 0$, i.e. at the surface of the antenna. An alternate method to compute impedance using power calculations would require cumbersome

volume integrals. From Eqns. 4.5 and 4.6, it is clear that the resonant and non-resonant impedances are in series. The resonant impedance will be computed as in (4.6). Since the short antennas are inefficient radiators, the nonresonant term will contribute mostly reactance to the diagonal terms in the impedance matrix. This nonresonant impedance will be modeled using lumped circuit elements.

The resonant field component is found for the source array by assuming $\hat{\mathbf{a}}_x$ directed point sources of the form

$$\int \mathbf{J}_S \cdot d\mathbf{x} = \hat{a}_x \sum_{p=1}^{P} \delta(x - x_p)\delta(y - y_p)\delta(z - d)\Delta X_p I_p, \tag{4.7}$$

where ΔX_p is the effective length of the p th current source and I_p is the terminal current of the p th antenna. Using (4.7) in the resonant part of (4.6) and taking the resonant terms from (3.40), the field within the resonator becomes

$$\mathbf{E}_S = -\frac{\hat{\mathbf{a}}_\mathbf{x}}{2} \sum_{mn} \left[\frac{R_{mn}\psi_{mn}}{(1 + R_{mn}\psi_{mn})} (E^-_{mn} - E^+_{mn}) \sum_{p=1}^{P} I_p \Delta X_p (E^-_{p,mn} - E^+_{p,mn}) \right], \tag{4.8}$$

where $E^\pm_{p,mn}$ indicates $E^\pm_{mn}$ evaluated at $\{x_p, y_p, d\}$. The resonant part of the driving point impedance can be found by substituting (4.8) into (4.5) and using the point source approximation for $\mathbf{J}_q$. This results in

$$z_q = \frac{\Delta X_q}{2I_q} \sum_{mn} \left[\frac{R_{mn}\psi_{mn}}{(1 + R_{mn}\psi_{mn})} (E^-_{q,mn} - E^+_{q,mn}) \sum_{p=1}^{P} I_p \Delta X_p (E^-_{p,mn} - E^+_{p,mn}) \right], \tag{4.9}$$

again $E^\pm_{q,mn}$ indicates $E^\pm_{mn}$ evaluated at $\{x_q, y_q, d\}$.

To characterize the array, we seek the elements z_{qp} of the impedance matrix $\mathbf{Z}$ which satisfies the equation

$$\mathbf{V} = \mathbf{ZI} \tag{4.10}$$

where $\mathbf{V}/\mathbf{I}$ are vectors of antenna terminal voltages/currents. The equation (4.9) for fixed q, can be seen to be the sum the q th row of $\mathbf{Z}$. The elements, z_{qp}, of the impedance matrix $\mathbf{Z}$ must be found but we cannot directly set $I_q = 0$ in (4.9). Consider one of the equations obtained from (4.10) by setting all $I = 0$ except $I_p = I_q = \hat{I}$. Thus

$$v_q = z_{qq} I_q + z_{qp} I_p = (z_{qq} + z_{qp})\hat{I}$$

so that

$$z_{qq} + z_{qp} = \frac{v_q}{\hat{I}}.$$

For this linear device, the driving point impedance with two active sources is the sum of the impedances when the same sources act individually. Any desired value for I_q and I_p may be chosen because z_{qq} and z_{qp} are independent of the values of these currents. Thus $z_{qq}+z_{qp}$ is found from (4.9) by setting $I = 0$ except $I_p = I_q = \hat{I}$.

$$\begin{aligned} z_{qq} + z_{qp} &= \frac{\Delta X_q}{2} \sum_{mn} \left[\frac{(R_{mn}\psi_{mn})}{(1 + R_{mn}\psi_{mn})} (E^-_{q,mn} - E^+_{q,mn}) \right. \\ &\quad \left. \cdot \left(\Delta X_q (E^-_{q,mn} - E^+_{q,mn}) + \Delta X_p (E^-_{p,mn} - E^+_{p,mn}) \right) \right]. \end{aligned} \tag{4.11}$$

Subtracting z_{qq} from (4.11) yields z_{qp}. The diagonal term,z_{qq} , is found from (4.9) by setting all $I_p = 0$ for $p \neq q$. When the expression for z_{qq} is subtracted from (4.11), the general impedance matrix term is found to be

$$z_{qp} = \frac{\Delta X_q \Delta X_p}{2} \sum_{mn} \left[\frac{R_{mn}\psi_{mn}}{(1 + R_{mn}\psi_{mn})} (E^-_{p,mn} - E^+_{p,mn})(E^-_{q,mn} - E^+_{q,mn}) \right]. \tag{4.12}$$

Alternatively, the expression for z_{qp} can also be derived by finding $\mathbf{E}_S$ when I_p acts alone, then using $z_{qp} = v_{qp}/I_p$, where

$$v_{qp} = -\int \mathbf{E}_S \cdot \hat{\mathbf{d}} \ell_q = -\Delta X_q E_{q,S}.$$

The result,(4.12), applies to infinitesimal $\hat{\mathbf{a}}_\mathbf{x}$-directed current sources. If both field polarizations are included and the small antenna assumption is removed, using (4.5) as the definition of impedance, (4.9) becomes

$$z_q = \frac{1}{2I_q^2} \sum_{mn} \frac{R_{mn}\psi_{mn})}{(1 + R_{mn}\psi_{mn})} \int_V (E_{mn}^- - E_{mn}^+)\mathbf{J}_q \cdot \int_{\acute{V}} (\acute{E}_{mn}^- - \acute{E}_{mn}^+)\bar{\mathbf{I}}_\mathbf{T} \cdot \mathbf{J}'_S dV' \, dV \quad (4.13)$$

where $\mathbf{J}_q$ is the source current density on the q th antenna.

Antenna Modeling

The nonresonant impedance for each antenna, which corresponds to the term with $\bar{\mathbf{G}}\mathbf{e}_h$ in (4.6), must be determined. The nonresonant behavior of each antenna was modeled by a lumped element circuit. Each antenna was situated over a ground plane then broad band impedance measurements were made. A Bodie plot of a representative measurement is shown in Fig. 4.6. A transmission line model was used to transform the impedance data from the location of the coaxial feed connection to the simulation plane as shown in Fig. 4.1. Values for the circuit elements were optimized so that the model response matched the impedance data.

The model for two short antennas radiating into the resonator is shown in Fig. 4.7. The cavity impedance model is given by (4.12) while each electrically short antenna is modeled by a lumped element circuit. The capacitor C_D represents the discontinuity of the outer conductor of the coaxial line at the simulation reference plane. The open circuited short transmission line formed by the antenna-wire over the ground plane is modeled by C_T. Some energy is lost due to radiation that does not couple into cavity modes, this is represented by R. Although the antenna lengths were approximately 3.2 mm long which corresponds to about $\lambda/10$ at the frequencies of investigation, resonance phenomena were observed to effect the phase of the antenna driving point impedance. So, L was included to account for these

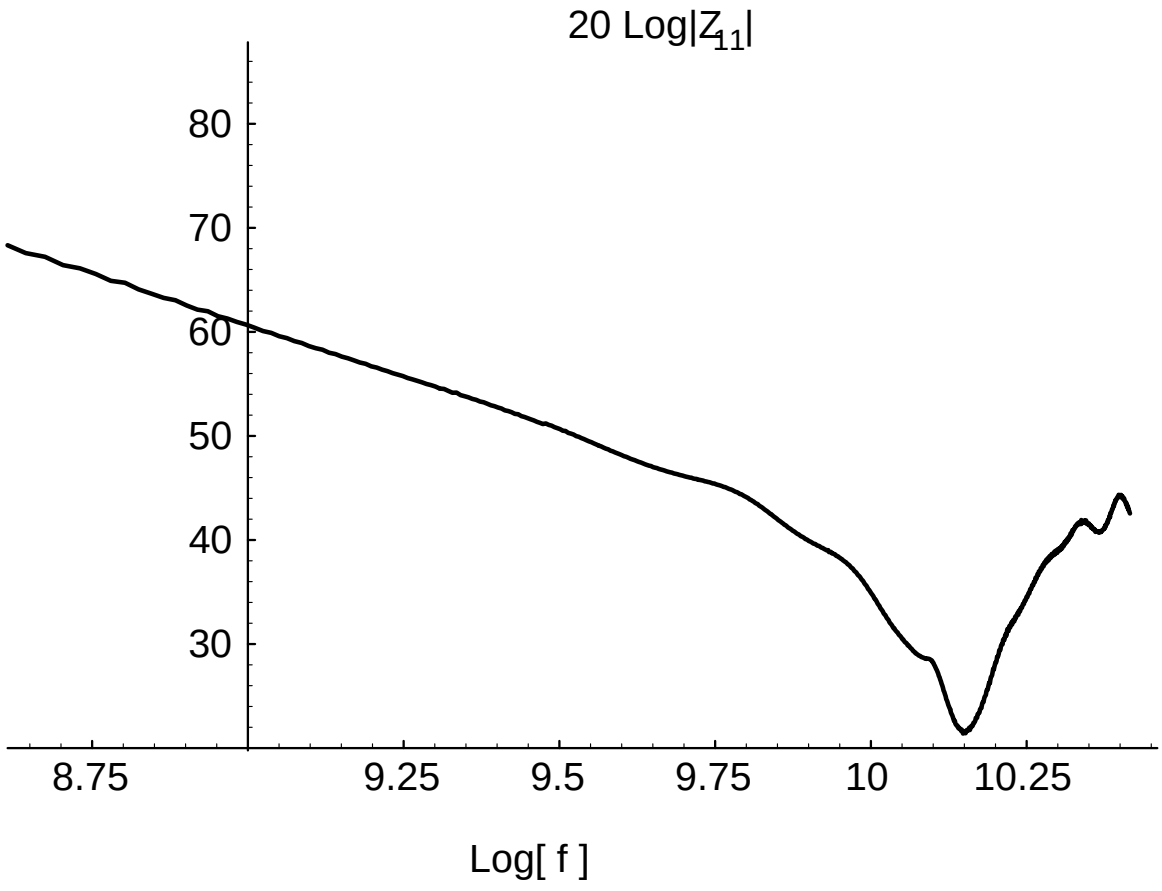

Figure 4.6: Magnitude Bode Plot of Measured Broad Band Impedance Data for an Inverted-L Antenna Over a Ground Plane.

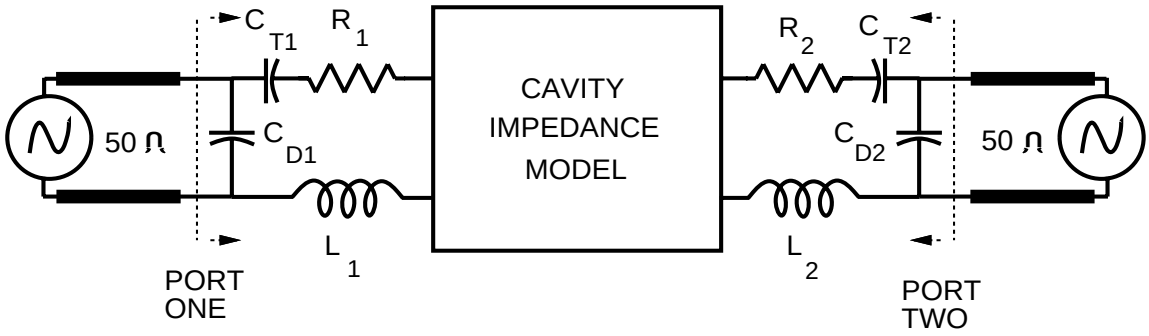

Figure 4.7: Two Port Model for Two Nonresonant Antennas Radiating into an Open Cavity.

	C_D fF	C_T fF	L nH	$R\ \Omega$
antenna 1	99.15	71.46	0.810	23.78
antenna 2	91.04	76.63	0.844	21.86

Table 4.1: Circuit Element Values for the Nonresonant Antenna Model.

effects. The optimized circuit values for (0.5 GHz $< f <$ 26.5 GHz) are shown in table 4.1. Each antenna is approximately 2.5 mm high.

The weights for the equivalent point sources in (4.7) must be determined. The inverted-L antenna located over a ground plane is approximated by an $\hat{\mathbf{a}}_\mathbf{x}$ directed point source and an $\hat{\mathbf{a}}_\mathbf{z}$ directed point source as shown in Fig. 4.8. The image sources are used in later work when the ground plane is removed. The values of $I\Delta X$ and $I\Delta Z$ for each antenna were determined as follows. For the electrically short antennas, $|\mathbf{J}_p|$ was assumed to taper linearly along the antenna from a value of I_0 at the ground plane, to zero at the end of the horizontal segment. The shape of the antennas was assumed to be comprised of two linear sections joined by a 1/4 circular arc as shown in Fig. 4.8. A function describing the $\hat{\mathbf{a}}_\mathbf{x}$ and $\hat{\mathbf{a}}_\mathbf{z}$ components of $\mathbf{J}_p$ was parameterized, the point source weights were found using line integrals.

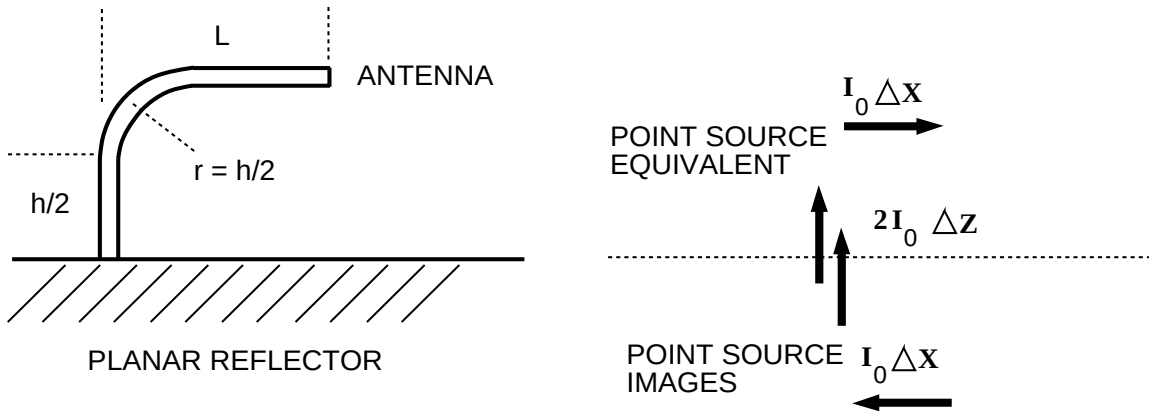

Figure 4.8: Inverted-L Antenna Over a Ground Plane and Equivalent Point Sources, Image Sources are Included if the Ground Plane is Removed.

$$I_0 \Delta X = \int \mathbf{J}_p \cdot \hat{\mathbf{a}}_\mathbf{x} d\ell$$

$$I_0 \Delta Z = \int \mathbf{J}_p \cdot \hat{\mathbf{a}}_\mathbf{z} d\ell \tag{4.14}$$

The weights of the equivalent point sources were found to be $I_0 \Delta X = 0.1145 I_0$ amp cm, and $I_0 \Delta Y = 0.19 I_0$ amp cm. The value for the $\hat{\mathbf{a}}_\mathbf{x}$ component of the current was used in the calculation of resonant impedance. The $\hat{\mathbf{a}}_\mathbf{z}$ directed current does not couple into the cavity mode structure.

Two Port Experimental Results

For each q, the transverse electromagnetic modes; TEM_{00}, TEM_{10}, TEM_{01}, TEM_{20}, TEM_{02}, and TEM_{11} were observed. The response for higher transverse mode numbers was very small due to diffraction losses. Two port measurements were made for each of these modes for the $q = 35$ family and are compared with simulated results in figures 4.9-4.17. The inverted-L antennas for port-1 and port-2 were located at $\{x, y\} = \{-9.06 \text{ cm}, 1.5 \text{ cm}\}$ and $\{x, y\} = \{2.7 \text{ cm}, 1.7 \text{ cm}\}$ respectively. The

modes are of high Q so measurements over three frequency ranges were required to resolve the resonances using 401 sampled frequency points per frequency range. Figures 4.9 and 4.10 show the magnitude and phase of z_{11} for the dominant mode and indicate very good agreement between simulation and measurement. The agreement for the TEM_{00} response of z_{22} was also observed to be very good. The relative agreement between measured and simulated magnitude and between measured and simulated phase are similar for all measurements, so magnitude information alone will be presented. Figure 4.11 shows very good agreement between measured and simulated values of z_{12} for the TEM_{00} mode.

A comparison for the TEM_{01} and TEM_{10} modes is made in Figs. 4.12-4.14. The measured and simulated responses for z_{11} differ by an impedance which is approximately constant over the frequency range shown in this figure. This difference is caused by a systematic measurement error. During calibration of the HP-8510B, calibration standards with 3.5mm connectors are placed at the measurement reference plane. After calibration, the HP-8510B ports are connected to the antenna feeds which are SMA connectors on RG-401 semirigid coaxial line, reflections occur at this connection. The measurement data is then transformed, using the transmission line equation, to the simulation plane. This transformed impedance data contains a small periodic ripple whose period corresponds to the length of the antenna feed line and is caused by an interaction between the reflection at the connector, and the transmission line transformation. As a result, the simulated antenna characteristics differ slightly from those of the physical data for some frequency ranges. Similar impedance offsets are seen in Figs. 4.15 and 4.16.

In Fig. 4.12 we can see that the simulated TEM_{01} mode response is much smaller than the measured response. This is thought to be due to an error in precisely locating the resonator axes during characterization of the resonator. Consequently

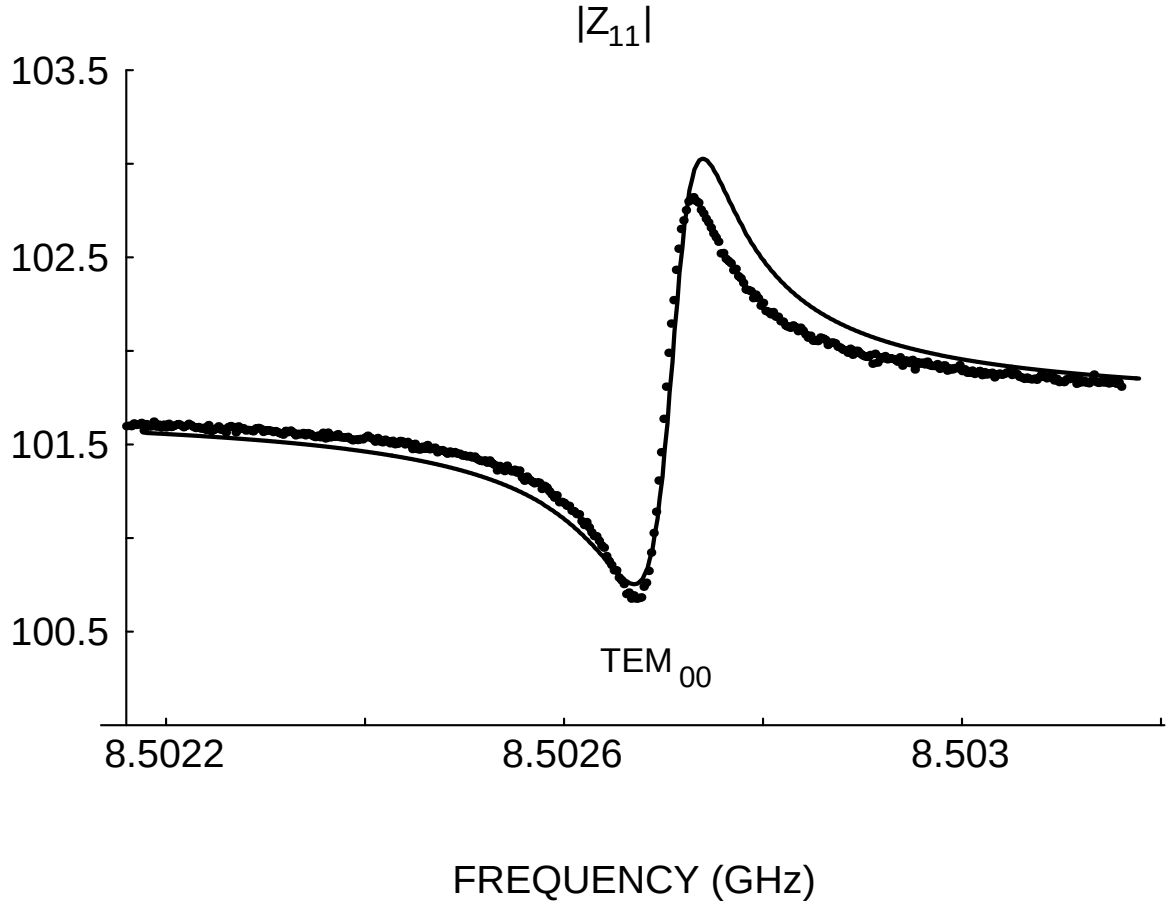

Figure 4.9: $|Z_{11}|$ of the Gaussian Mode for a Two Antenna Array.

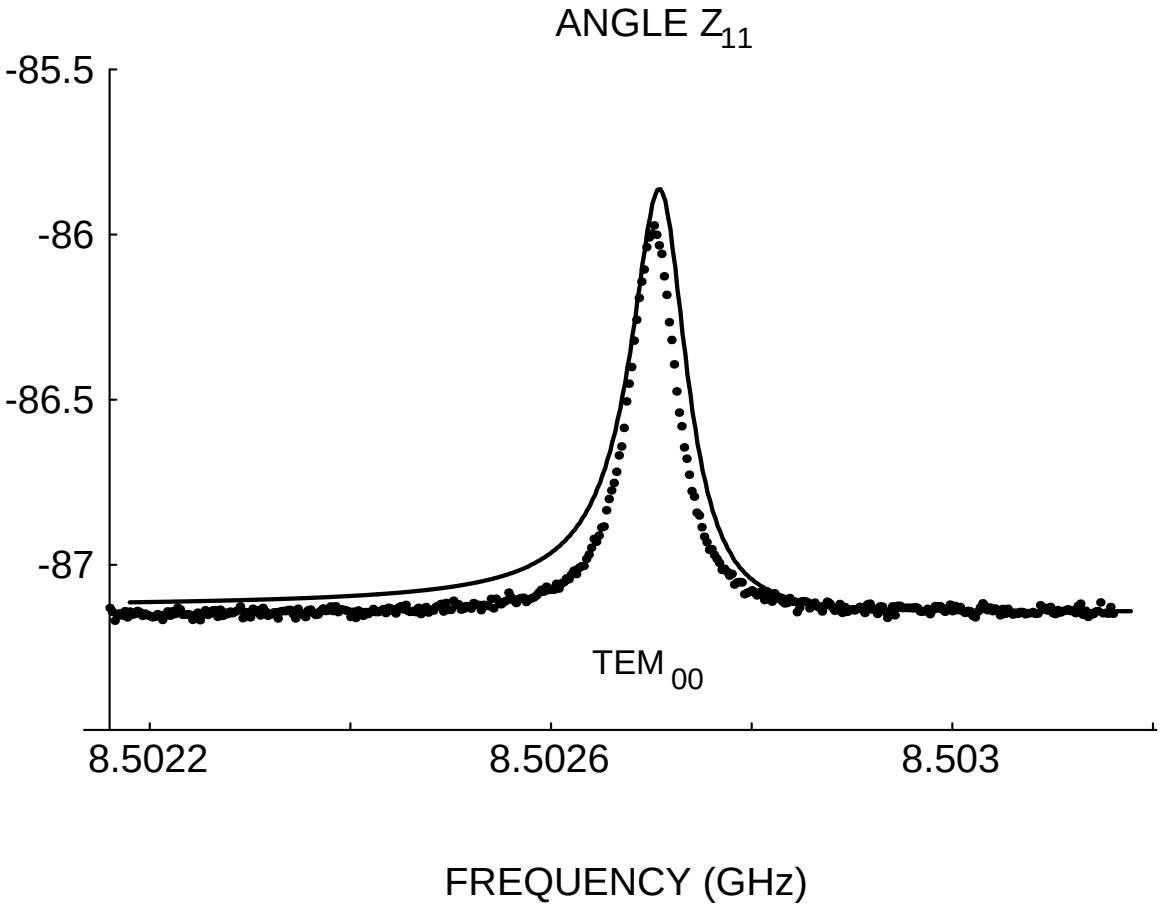

Figure 4.10: Arg Z_{11} of the Gaussian mode for a Two Antenna Array.

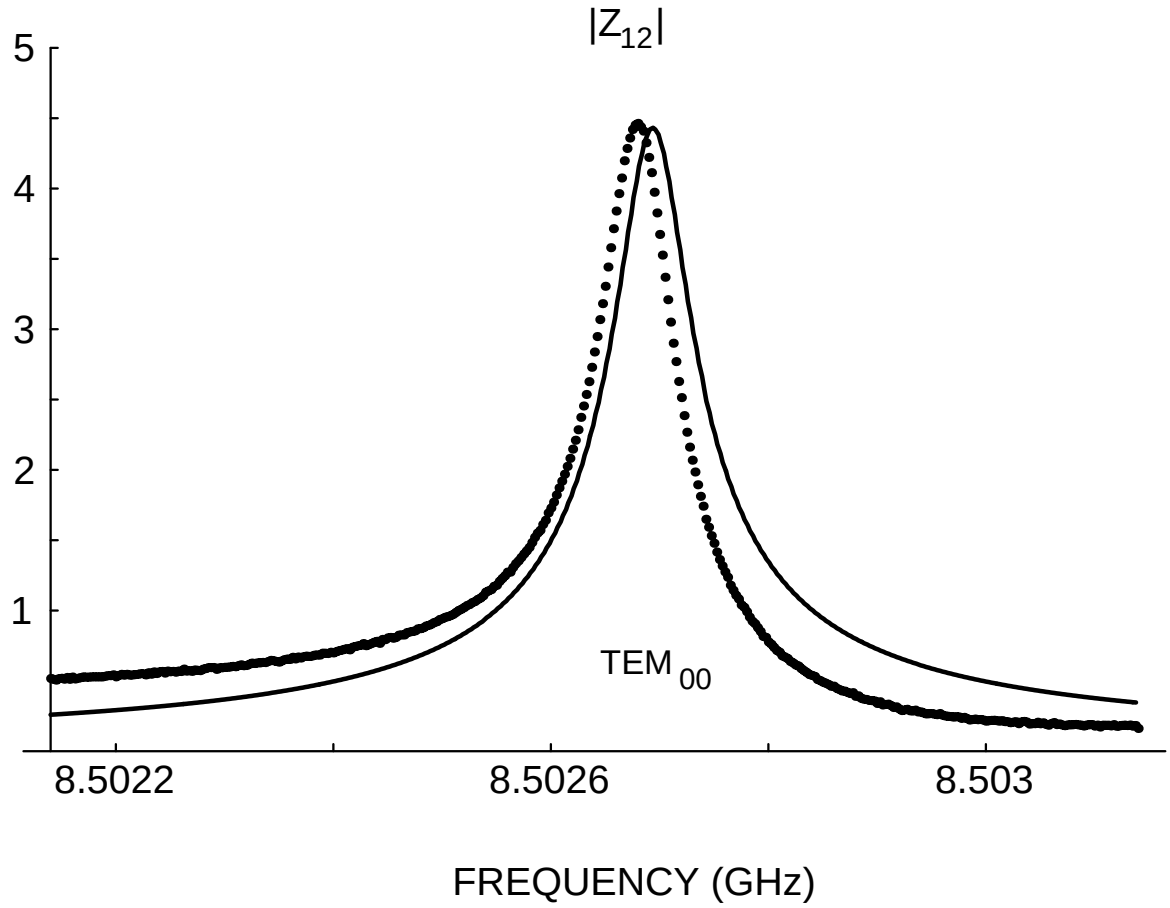

Figure 4.11: $|Z_{12}|$ of the Gaussian Mode for a Two Antenna Array.

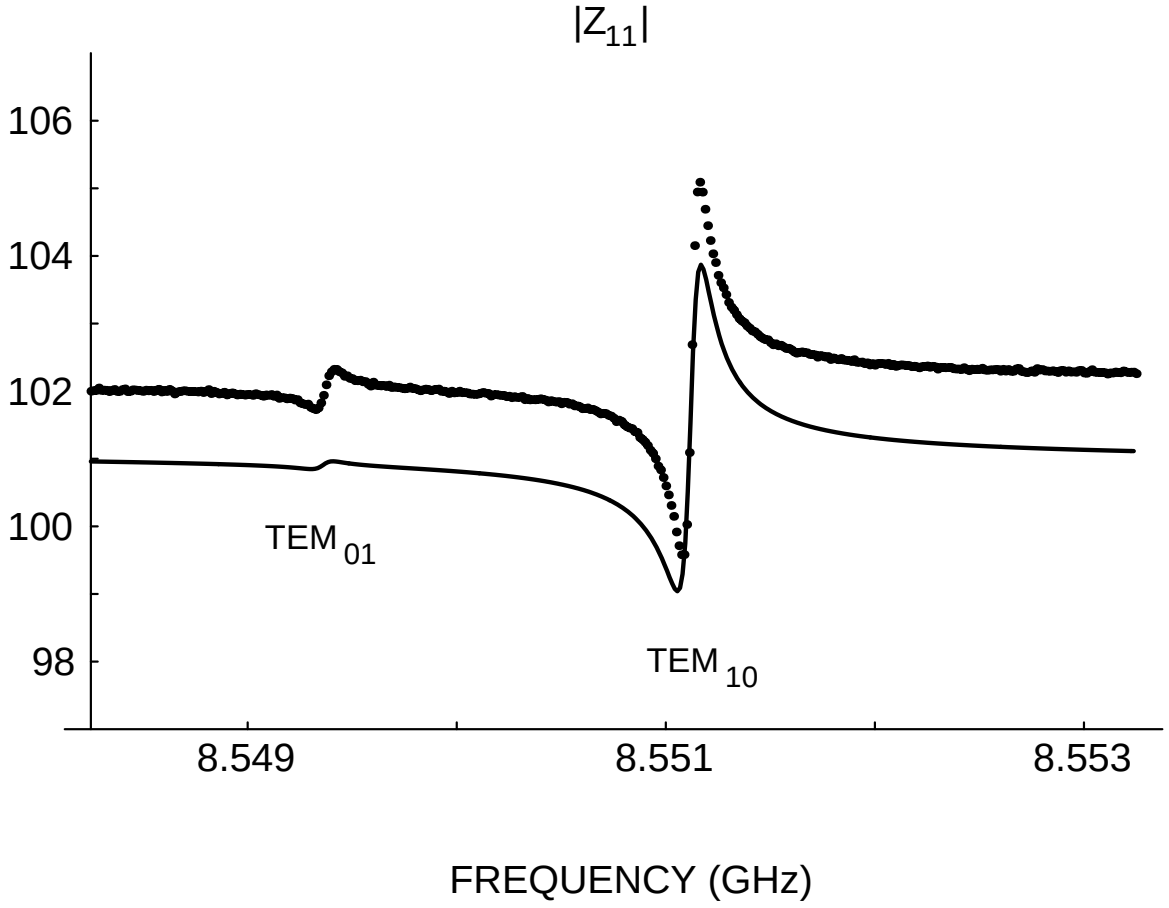

Figure 4.12: $|Z_{11}|$ for Modes With $m + n = 1$ Which Are Not Degenerate Due to a Distorted Reflector.

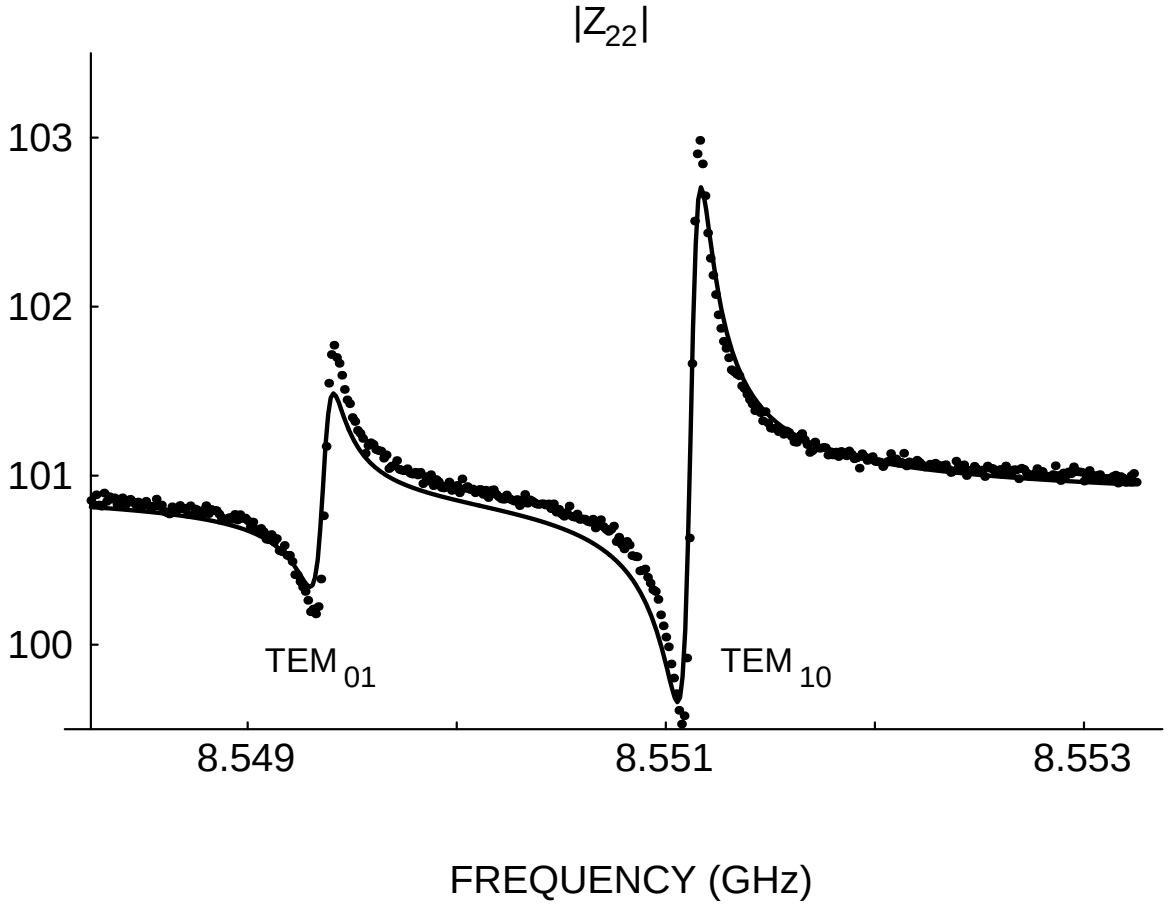

Figure 4.13: $|Z_{22}|$ for Modes With $m + n = 1$.

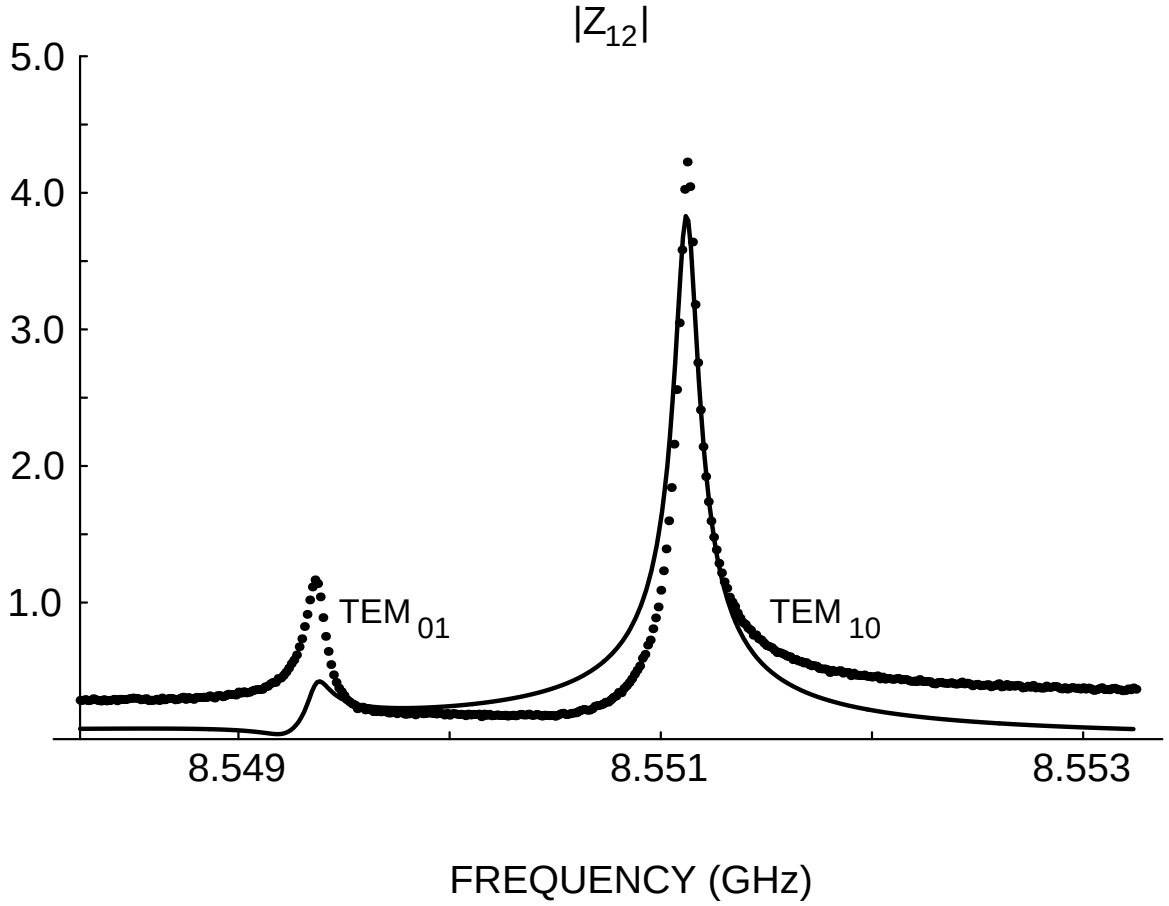

Figure 4.14: $|Z_{12}|$ for Modes With $m + n = 1$.

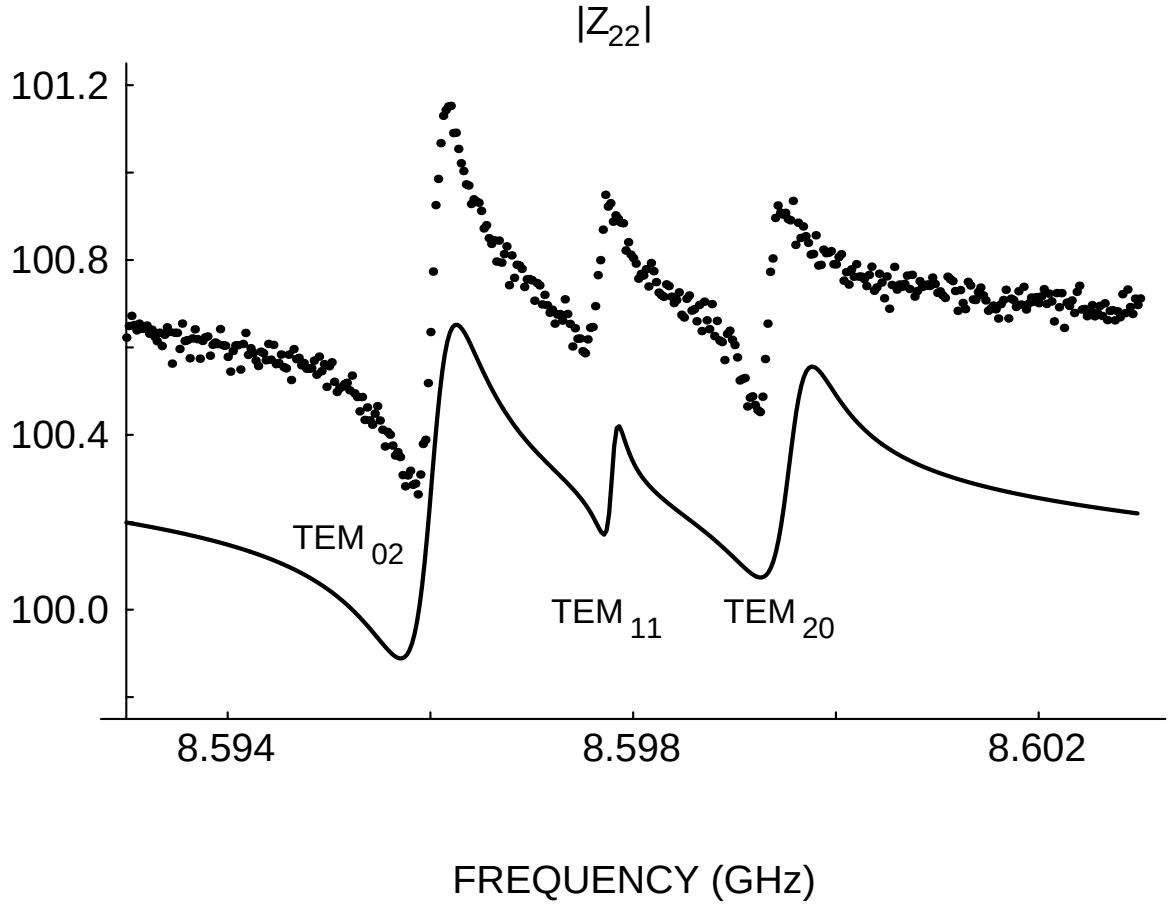

Figure 4.15: $|Z_{22}|$ for Modes With $m + n = 2$.

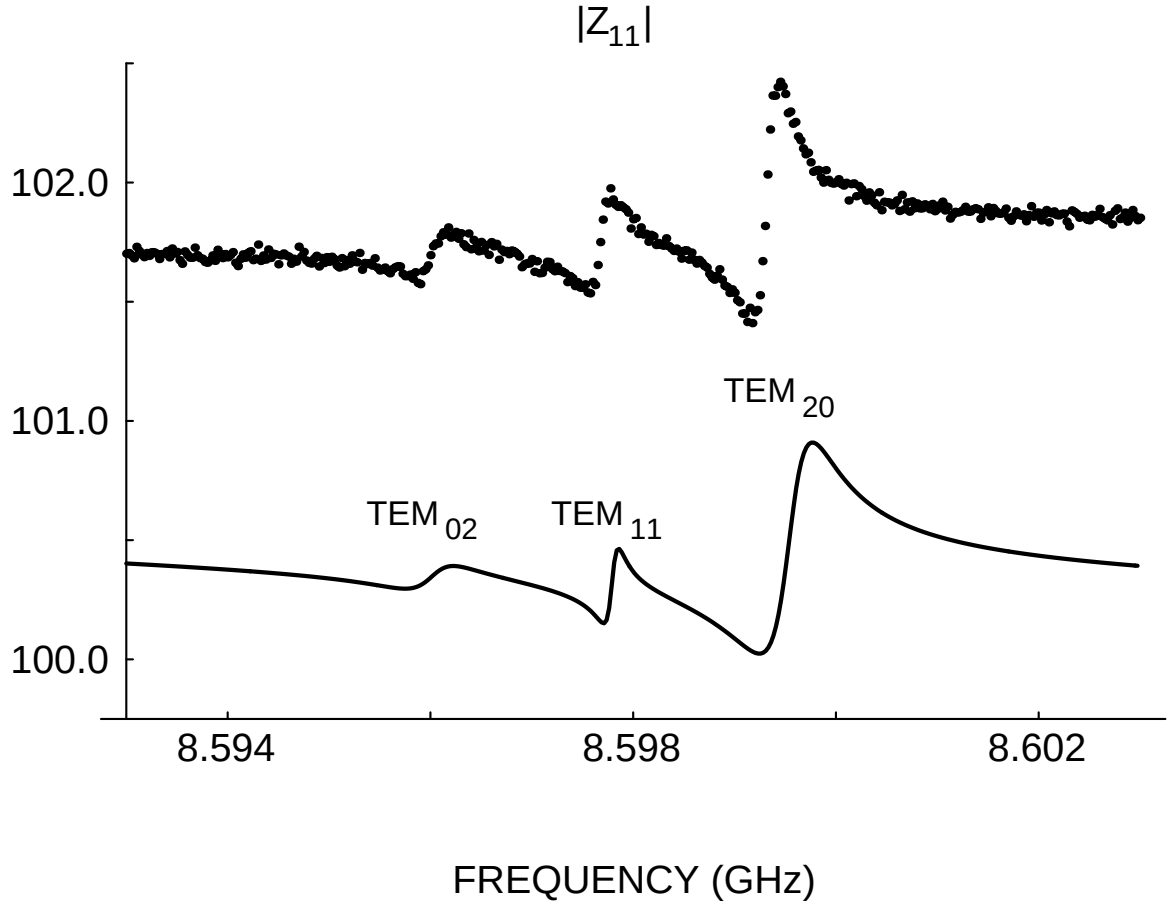

Figure 4.16: $|Z_{11}|$ for Modes With $m + n = 2$.

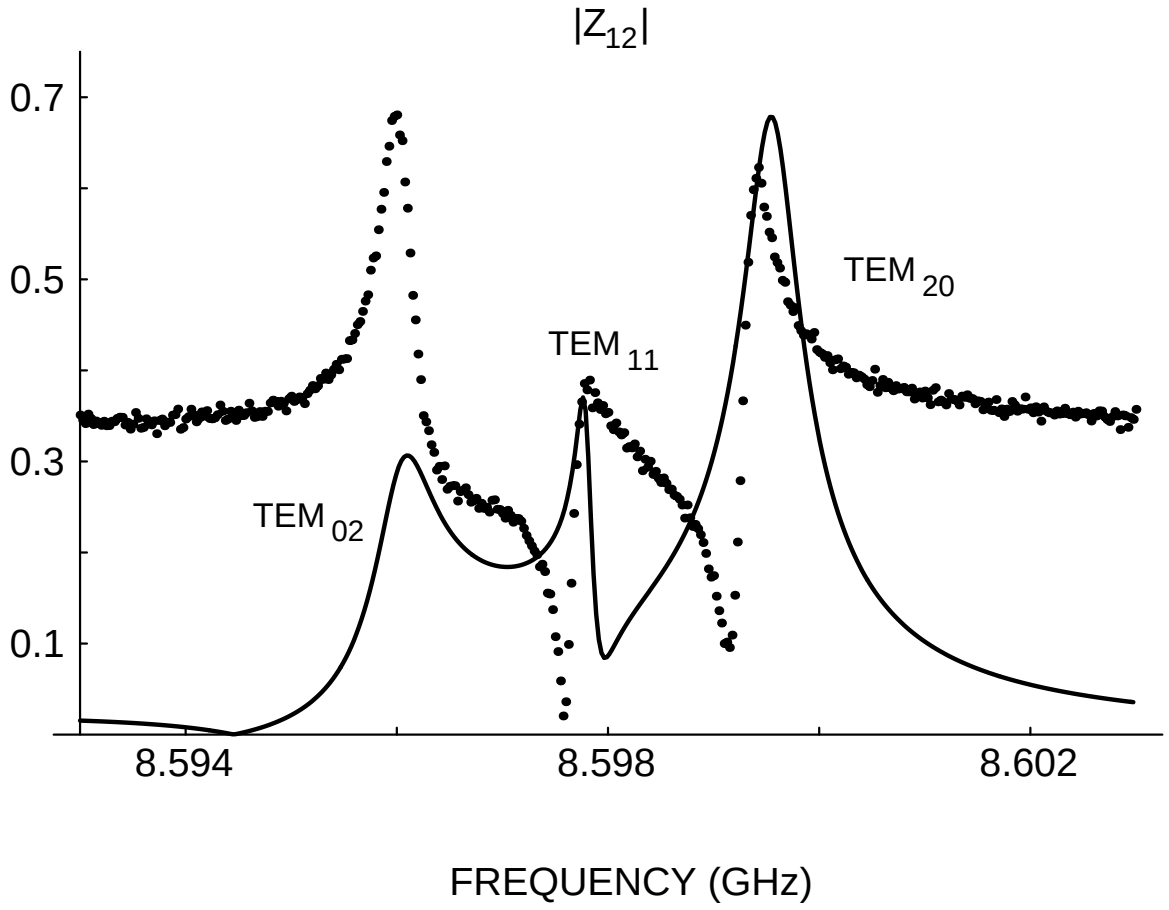

Figure 4.17: $|Z_{11}|$ for Modes With $m + n = 2$, Error is Because Direct Radiation Coupling Was Ignored.

the simulated antenna location is different from the the exact location of the physical antenna. In Fig. 4.14 it is apparent that the simulated value of $|z_{12}|$ is similarly effected for the TEM_{01} mode. Another discrepancy is that the simulated value of z_{12} goes to zero at frequencies which are far removed from resonance while the measured value approaches a small nonzero impedance. It is believed that this is due to direct radiation coupling between the two antennas. Direct coupling effects were not included in the simulator model, $\bar{\mathbf{G}}\mathbf{e}_h$ was not used, but will be considered in the next section.

A comparison of the TEM_{02}, TEM_{11}, and TEM_{20} modes is shown in Figs. 4.15-4.17. Again the simulated values for z_{11} and z_{22} are in excellent agreement. In Fig. 4.17 the coupling through direct radiation is no longer small compared with the coupling though the resonator modes. At some frequencies the two forms of coupling are in phase and reinforce each other, while they are out of phase and of apparently equal magnitude at others.

4.1.3 Full Green's Function Analysis

Figure 4.17 indicates that the previous analysis, which used $\bar{\mathbf{G}}\mathbf{e}_r$ in conjunction with a circuit model for the antenna, does not give accurate results under all conditions. This approach is probably sufficiently accurate for the diagonal terms of $\mathbf{Z}$, but ignores direct radiation coupling in all the off diagonal terms.

Z_{12} was calculated for the two antennas using $\bar{\mathbf{G}}\mathbf{e}_n$ rather than the circuit model. For off diagonal terms, the impedance definition 4.5 can be applied since the source current is zero over the range of integration. For a line current, the form of $\bar{\mathbf{G}}\mathbf{e}_h$ expressed in (3.38) cannot be used because the derivatives over the source coordinates present problems. The nonresonant fields indicated in (4.6) were computed

using the free space vector magnetic potential [39]. The ground plane was removed and the equivalent point sources and their images as seen in Fig. 4.8 were used to compute the nonresonant part of $\mathbf{E}_S$. The nonresonant part of Z_{12} was calculated using (4.5) and was then added to the resonant part of Z_{12} which was calculated previously. Figure 4.18 indicates that this calculation gives much better results than the circuit model approach.

4.2 Radiators Having Unknown Current Distributions

In the analysis of short antennas, satisfactory results were obtained by assuming the functional form of the antenna current density. This approach was successful because the short antennas are very inefficient radiators and interaction with the cavity field distribution has only modest effects on the antenna current density. This technique will not work with larger, resonant sized antennae. It is expected that the current distribution for an antenna radiating into a resonator will be substantially different from the current distribution of the same antenna radiating into free space. The effect of the resonator on the antenna current distribution can be determined iteratively using a perturbation technique.

4.2.1 Analysis of Resonant Circular Patch Antenna

Patch antenna arrays are logical choices for coupling into a cavity. The arrays and their active driving devices can be fabricated monolithically. The array ground plane can be placed in contact with the surface of the planar reflector which provides mechanical support and acts as a heat sink. Active devices can be impedance matched to the patch antenna in the cavity by selecting the correct antenna feed

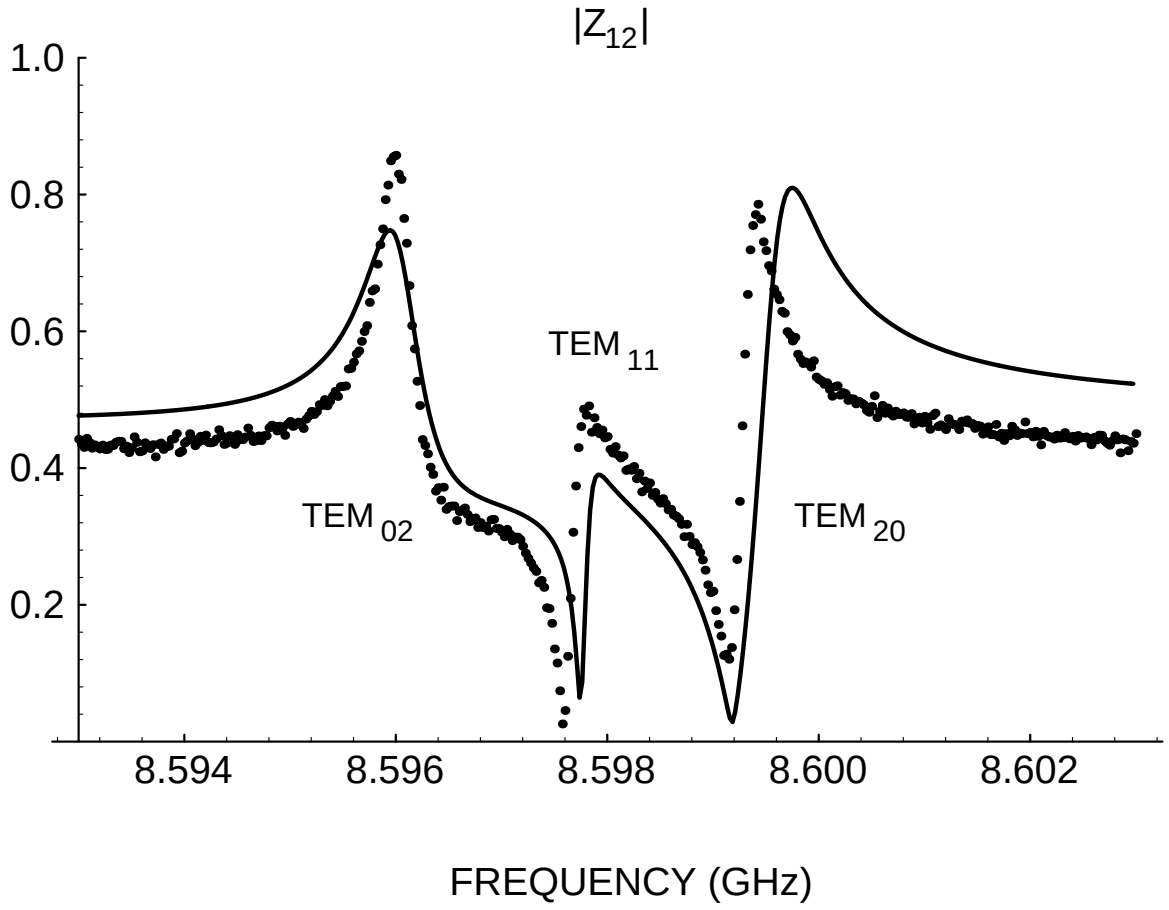

Figure 4.18: $|Z_{12}|$ Calculated Using the Full Green's Function, $\bar{\mathbf{G}}\mathbf{e}_c$.

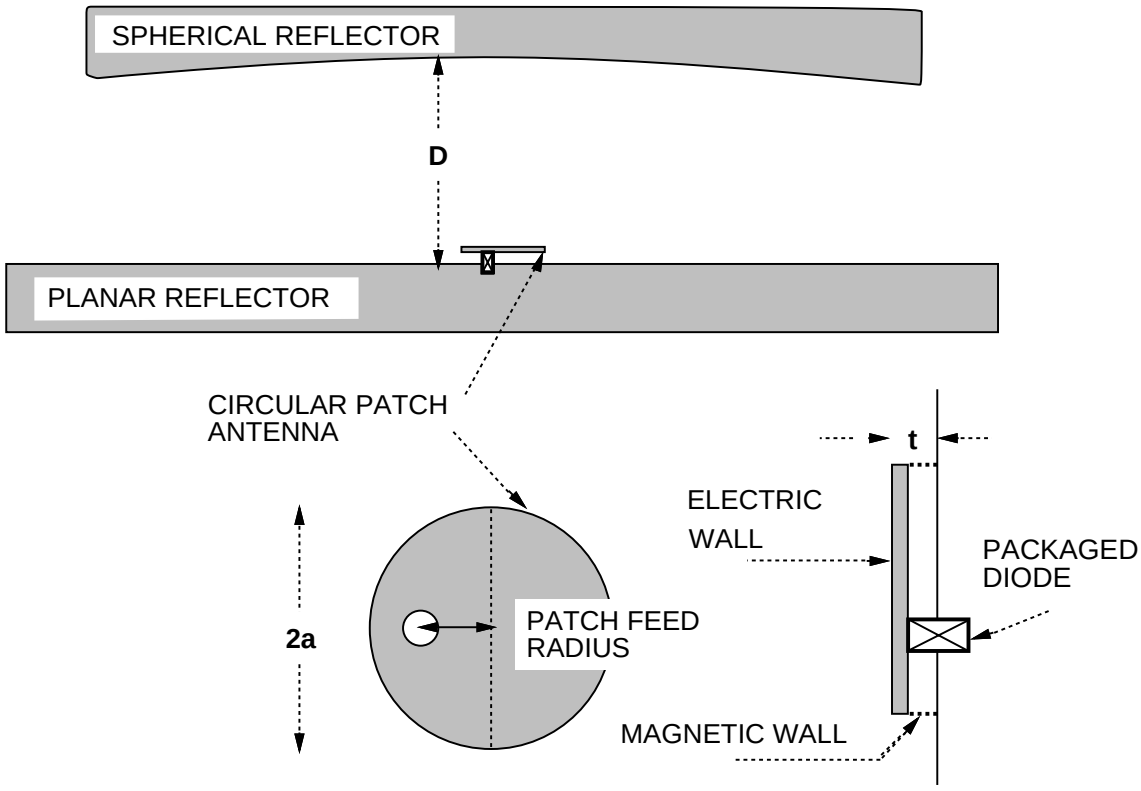

Figure 4.19: Singular Circular Patch Antenna Within a Cavity.

point [82].

A single circular patch antenna within the cavity depicted in Fig. 4.19 is considered and will be modeled using the cavity model [61], [82]. Other patch shapes can be analyzed using the same method. Patches on a dielectric substrate can be analyzed using the same method provided that the patch height t is not too high.

$$t \leq \lambda_\epsilon 0.02 \tag{4.15}$$

Otherwise surface waves can be excited in the dielectric. If (4.15) is not satisfied, then full wave analysis may be required for accurate results. To account for fringing

fields an effective patch radius a_e is used in calculations [82]

$$a_e = a\left[1 + \frac{2t}{\pi a \epsilon_r}\left(\ln\frac{\pi a}{2t} + 1.7726\right)\right]^{1/2}. \tag{4.16}$$

The active device is assumed to be an IMPATT or GUNN diode which is located between the patch and the ground plane. The objective of the analysis is to determine a procedure which will yield the the effective impedance presented to the diode. During the analysis the diode can be replaced by a filamentary $\hat{\mathbf{a}}_\mathbf{z}$ directed current source.

The eigenfunctions and eigenvalues of the Hemholtz equation for the patch are determined. The boundary conditions under the patch at the ground plane $z = 0$ and just under the patch $z = t^-$ are $\mathbf{E} \times \hat{\mathbf{a}}_\mathbf{z} = 0$. From this and (4.15) the form of the electric field under the patch is assumed to be

$$\mathbf{E} = \Phi(x, y)\hat{\mathbf{a}}_\mathbf{z}. \tag{4.17}$$

Application of Faraday's law to (4.17) yields the form of the magnetic field

$$\mathbf{H} = \frac{\hat{\mathbf{a}}_\mathbf{z}}{i\omega\mu} \times \nabla_t \Phi \tag{4.18}$$

where ∇_t operates on the transverse coordinates only.

Using circular cylindrical coordinates centered on the patch, we can see that the patch surface current must satisfy $\mathbf{J} \cdot \hat{\mathbf{a}}_\mathbf{r} = 0$ at $r = a$. Since $-\hat{\mathbf{a}}_\mathbf{z} \times \mathbf{H} = \mathbf{J}$ and $\mathbf{H}$ is not a function of z, then $\mathbf{H} \cdot \hat{\mathbf{a}}_\mathbf{r} = 0$ at $r = a$. Using this fact and (4.18) with ∇_t expressed in cylindrical coordinates, we can state the boundary condition for Φ

$$\frac{\partial \Phi}{\partial r} = 0, \quad r = a. \tag{4.19}$$

This is the so called magnetic wall boundary condition. The requirement that H have no tangential components at the patch edge is equivalent to placing a perfect magnetic conductor at this location.

If the forms (4.17) and (4.18) are used in conjunction with Maxwell's equations, it can be shown that Φ satisfies the homogeneous transverse Hemholtz equation

$$\nabla_t^2 \Phi + k\Phi = 0. \tag{4.20}$$

This formulation is called the cavity model for patch antennas because the patch antenna is treated as a closed resonator with electric walls on top and bottom, and magnetic side walls. A solution of (4.20) and (4.19) exists only for discrete values of $k = k_{mn}$ and $\Phi = \Phi_{mn}$. These eigenvalues and eigenfunctions describe the resonant frequencies and modes of the patch cavity. For a circular patch these solutions are

$$\Phi_{mn} = J_m \left(\frac{k_{mn} a}{r} \right) \cos(m\phi) \tag{4.21}$$

where $J_m(x)$ is a Bessel function of the first kind of order m. The eigenvalue k_{nm} is the n th root of the equation

$$\frac{\partial J_m(kr)}{\partial (kr)} \mid_{r=a} = 0. \tag{4.22}$$

To analyze a patch with an $\hat{\mathbf{a}}_\mathbf{z}$ directed source current, the solution of the inhomogeneous Hemholtz equation is assumed to be a series of eigenfunctions. This series is substituted into the inhomogeneous equation, both sides of the equation are multiplied by Φ_{pq}, and the orthogonality relationship

$$\int_0^{2\pi} \int_0^a \Phi_{mn} \Phi_{pq}^* r dr d\phi =$$

$$\frac{a^2 \pi}{2} J^2(k_{mn}) \left(1 - \frac{n^2}{k_{mn}^2} \right) \delta_{mp} \delta_{nq} \tag{4.23}$$

is applied. This determines the coefficients of the expansion, resulting in an expression for the forced oscillation of the patch.

$$\mathbf{E} = \frac{1}{2} i\omega\mu \hat{\mathbf{a}}_\mathbf{z} a^2 \pi$$

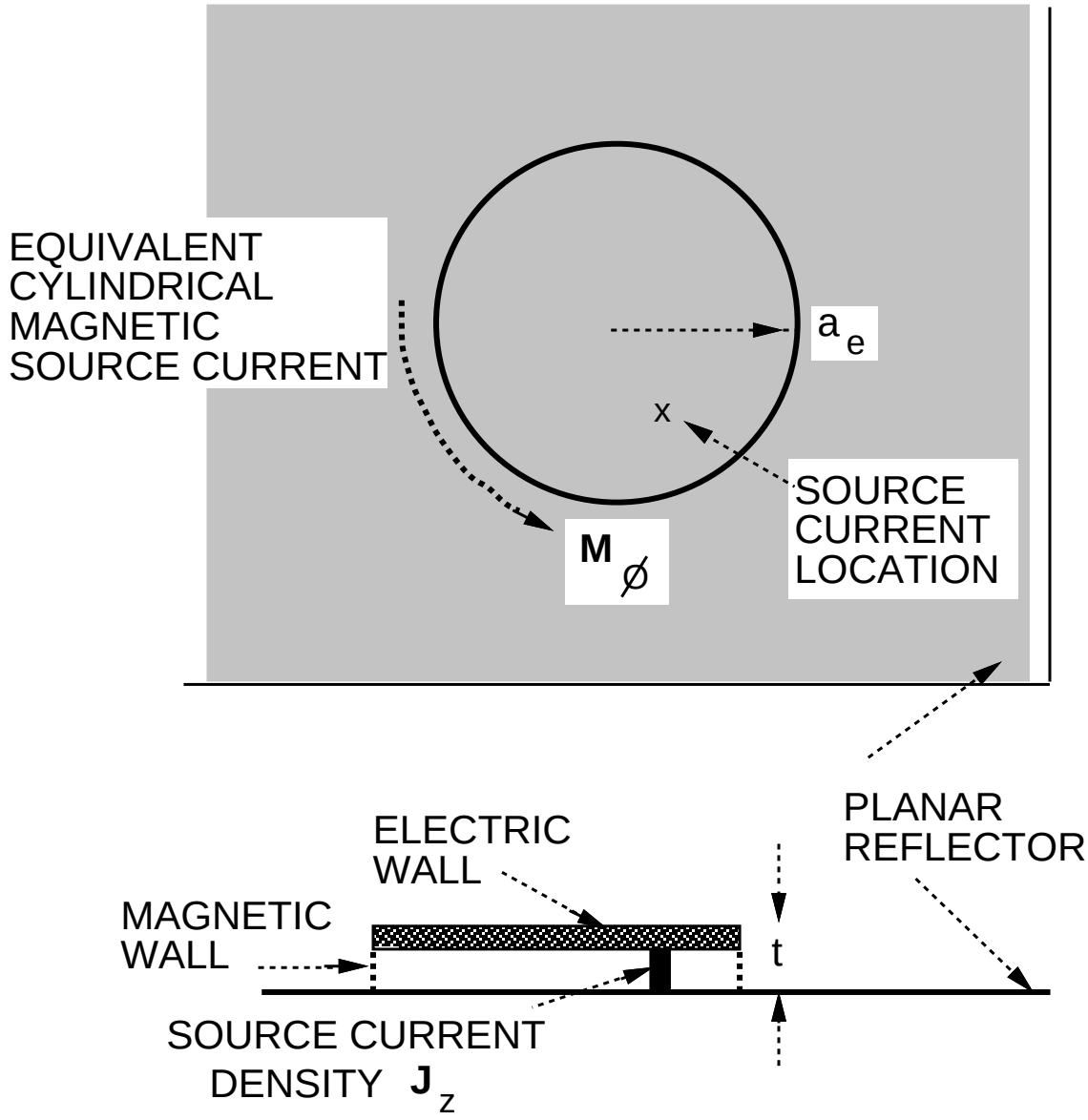

Figure 4.20: Circular Patch Antenna and Equivalent Magnetic Current Density Used for Radiation Calculations.

$$\cdot \sum_{mn} \left[\left(1 - \frac{n^2}{k_{mn}^2} \right) J_{mn}^2(k_{mn}) \frac{\Phi_{mn}}{k^2 - k_{mn}^2} \int_0^{2\pi} \int_0^a J \Phi_{mn}^* r dr d\phi \right] \tag{4.24}$$

The fields under the patch which are induced by a source current density are now specified by (4.24) and (4.18). The patch radiation is assumed to be caused mainly by fringing fields and is determined by ignoring the electric current density on the patch and considering only the electric field at the edge of the patch. This situation is depicted in Fig. 4.20 in which the patch is replaced by a magnetic current density. The equivalent cylindrical magnetic current density is determined using the boundary condition for a perfect magnetic conductor,

$$\mathbf{M} = -\hat{\mathbf{a}}_\mathbf{r} \times \mathbf{E}. \tag{4.25}$$

Then the cavity dyadic Green's function is used to determine the resonator fields and radiated fields

$$\mathbf{E}_c = \int_{\acute{V}} \bar{\mathbf{G}} \mathbf{h}_c \cdot \mathbf{M} d\acute{v} \tag{4.26}$$

Finally, the driving point impedance of the patch is determined from $z = V/I$ where I is the known source current at $\{x, y\} = \{x_0, y_0\}$. Due to (4.17), V is found to be

$$V = -\int_0^t \mathbf{E}(x_0, y_0, z) \cdot \hat{\mathbf{a}}_\mathbf{z} dz \tag{4.27}$$

So far, the model treats the patch as an ideal lossless cavity. Since the eigenvalues are real, the patch model predicts an infinite response at the resonant frequencies. The effects of power lost due to radiation, conductor losses and resonator reflector losses are not included. The effects of energy storage in the quasi-optical resonator must also be included. The effects of energy storage and power loss are included by the use of a complex wavenumber in the denominator of (4.24)

$$\tilde{k} = k' + ik'' = \omega \sqrt{\mu \epsilon_{\text{eff}}} \tag{4.28}$$

which comes about by defining an effective permittivity $\epsilon_{\text{eff}} = \epsilon_0\epsilon_r(1 - i\delta_{\text{eff}})$ where δ_{eff} is an effective dielectric loss tangent. For cavities, $\delta_{\text{eff}} = 1/Q$ so the complex wavenumber can be found by computing Q which is defined [39]

$$Q = \omega\frac{(U_e + U_m)}{P_\ell}. \tag{4.29}$$

U_e and U_m are the time average energy stored in the electric and magnetic fields. Energy storage is assumed to be due to fields under the patch, and the resonant modes of the cavity $\mathbf{E_r}$, this makes the volume integral much easier.

$$U_e = \frac{\epsilon_0}{4}\int_{\text{patch}} \mathbf{E}\cdot\mathbf{E}^* dv + \frac{\epsilon_0}{4}\int_{\text{resonator}} \mathbf{E_r}\cdot\mathbf{E_r^*} dv \tag{4.30}$$

$$U_m = \frac{\mu_0}{4}\int_{\text{patch}} \mathbf{H}\cdot\mathbf{H}^* dv + \frac{\mu_0}{4}\int_{\text{resonator}} \mathbf{H_r}\cdot\mathbf{H_r^*} dv. \tag{4.31}$$

The power lost from the system, P_ℓ, is due to radiation losses P_{rad} , reflector losses P_{ref} which includes diffraction losses with output coupling and reflector conductor losses, dielectric losses under the patch P_d, and conductor losses on the patch and the ground plane beneath the patch P_{cond}.

P_{rad} is assumed to be due only to the field terms produced by $\bar{\mathbf{G}}\mathbf{h}_n$ and using Poynting's theorem can be found by the the surface integral in spherical coordinates,

$$P_{\text{rad}} = \text{Re}\int_0^{\pi/2}\int_0^{2\pi}(E_\theta H_\phi^* - E_\phi H_\theta^*)r^2\sin\theta\, d\phi d\theta. \tag{4.32}$$

P_{cond} is found by the usual surface resistance calculation, P_d is found by modeling the lossy dielectric as having an equivalent conductivity $\sigma_d = \omega\epsilon_r\epsilon_0\delta$.

Once Q is obtained, $\tilde{k}$ is calculated, then (4.24) can be applied again. This process is repeated until the solution for the fields under the patch relax to a constant value from iteration to iteration. This process is illustrated in Fig. 4.21.

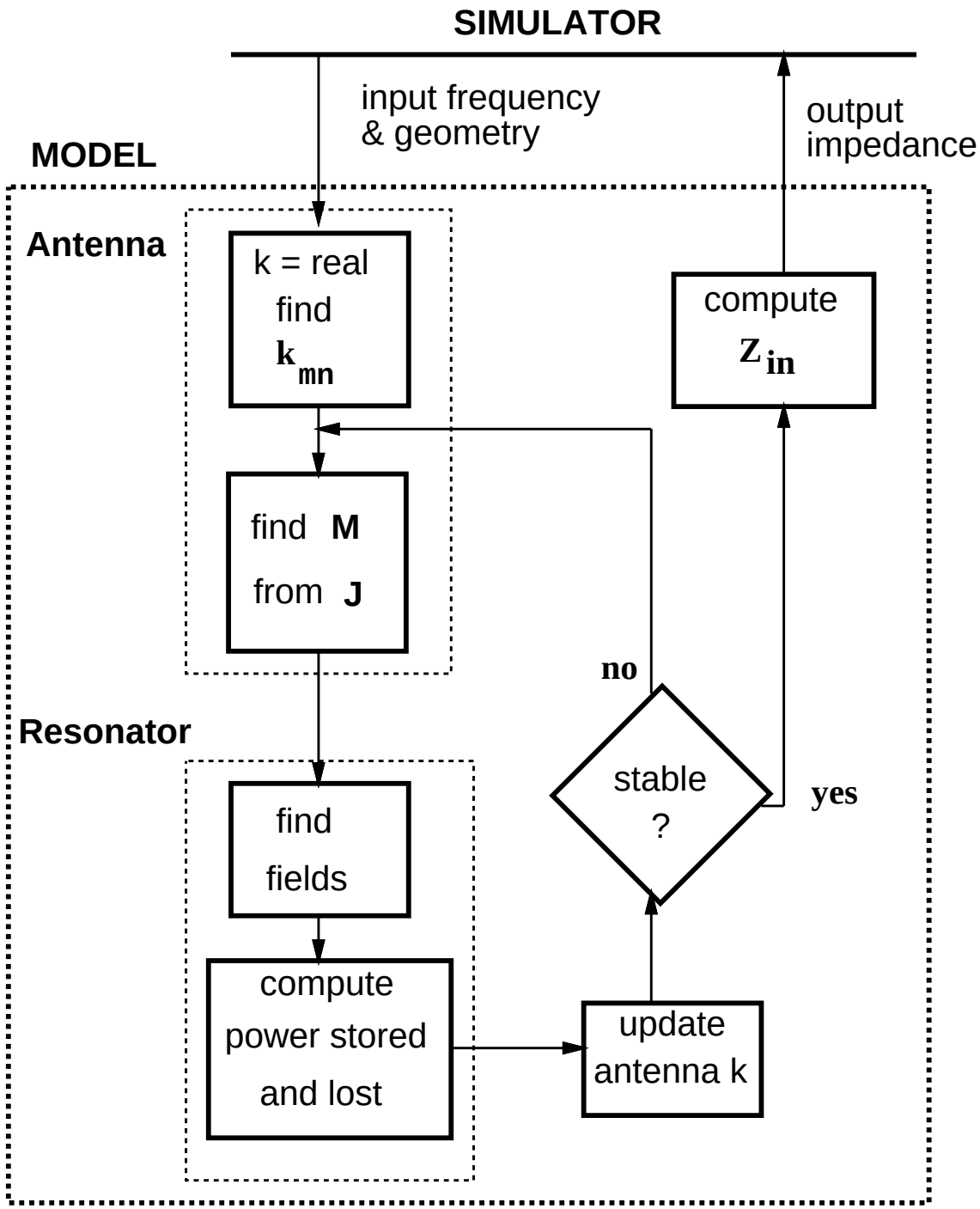

Figure 4.21: Iterative Model for a Circuit Simulator Describing a Patch Antenna in a Quasi-Optical Resonator.

4.3 Practical Considerations for Simulation of Quasi-Optical Systems

To design or analyze quasi-optical systems a model is derived using $\bar{\mathbf{G}}\mathbf{e}_c$ or $\bar{\mathbf{G}}\mathbf{h}_c$ and used in conjunction with a circuit simulator. A harmonic balance type simulation is the logical choice as the Green's function provides a linear frequency domain description of the cavity and the models for nonlinear solid state devices are most often in the time domain. If we consider one iteration of a simulation for an $n \times n$ oscillator array, each of the n^2 active device models will have to be evaluated for an input driving time sequence. While the linear model for the array driving point impedance matrix will contain n^4 th terms , each must be evaluated at every analysis frequency and each of these evaluations is an iterative procedure. The linear model is reciprocal, so only $n^2(N^2+1)/2$ are independent and further reduction is possible if array symmetry can be exploited (this is true regarding the nonlinear elements also). Nonetheless, evaluation of the impedance matrix is a formidable task. When a simulator is searching to determine the system oscillation frequency set, the impedance matrix must be re-evaluated at each frequency guess. Simulator efficiency can be substantially improved if the number of frequencies that are used in the frequency domain analysis can be reduced. If the analysis frequency set is too small, however, significant error can be introduced during the evaluation of the nonlinear time domain models and the subsequent Fourier transform. It can be shown that in many cases, much of this error is due to aliasing during the Fourier transform operation [72].

In appendix A, background on the harmonic balance simulation technique is provided. A dual frequency set analysis technique is introduced. In this technique the spectrum of the frequencies used in the transform is sufficiently large to include

modulation effects of the nonliner elements. The frequency domain spectrum is a subset of the transform spectrum. This technique eliminates error due to transform aliasing and allows for evaluation of the linear cavity model at fewer frequencies.

Figure 4.22 represents data which was taken for a single pulsed IMPATT oscillator within a quasi-optical resonator. It can be seen that the oscillator produces power at several incommensurate frequencies. This results in a different problem when simulating oscillators in a quasi-optical cavity. Standard transform techniques utilize a set of frequencies $\{\omega_0,\ \omega_1,\ \ldots,\ \omega_N\}$ in which all frequencies are harmonics of the lowest frequency, $\omega_n = n\omega_0$. This constraint is unacceptable for frequencies given by (4.1). A multidimensional transform can be used for this case, in particular multidimensional fast transform techniques are attractive due to their efficiency. One problem that is encountered when using the multidimensional fast Fourier transform is obtaining the frequency domain response derivatives for the time domain nonliner elements. This information is required at each iteration to determine the simulation solution. One approach that has been used is to numerically approximate these derivatives using finite difference techniques. This approximation is often insufficiently accurate resulting in poor simulation results. A technique is derived in appendix B that allows efficient analytic computation of the frequency domain derivatives using known time domain derivatives and the multidimensional fast transform. Use of this technique allows the harmonic balance analysis of quasi-optical systems which operate at a set of incommensurate frequencies.

Figure 4.22: Spectrum of a Single Pulsed IMPATT Oscillator in a Quasi-Optical Cavity Showing Oscillation at Incommensurate Frequencies.

Chapter 5

Conclusions and Future Research

5.1 Conclusions

This dissertation provides five original contributions to the field of modeling and simulation of quasi-optical systems. In chapter 3, Green's functions are derived which describe the electromagnetic fields excited by electric and magnetic source current densities within a plano-concave open resonator. Each Green's function is composed of a term which describes the resonant cavity fields and a term which accounts for nonresonant fields. The resonant field Green's functions are expressed as a series of traveling wave beam modes. Source currents are assumed to be located near the resonator planar reflector and the fields are assumed to be approximately TEM in this region. Reflector losses and diffraction losses are incorporated by perturbing the resonance denominator term of $\bar{\mathbf{G}}\mathbf{e}_r$ and $\bar{\mathbf{G}}\mathbf{h}_r$. Reflection losses are determined by characterization of the resonator reflectors. Diffraction losses are found by formulating an integral equation for the cavity using Huygen's principle, then numerically solving the equation. The nonresonant field Green's function component is determined by considering a half space Green's function, then removing the components which couple into paraxial fields.

An impedance model for an array of small antennas which radiate into a quasi-optical resonator was developed. The current distribution is assumed to taper linearly along the length of each antenna. Each small antenna is replaced by an equivalent point source, then the Green's function is applied to determine the induced

fields. A reaction principle is applied to determine the driving point impedance of each antenna. The array driving point impedance matrix is calculated from this information. An experimental quasi-optical resonator was designed and constructed. Two port microwave measurements were taken for inverted-L antennas at X-band in the cavity. These measurements show excellent agreement with results of the impedance model calculations.

A method was derived which models the coupling into a quasi-optical cavity by antennas or apertures that are not electrically small. The current distribution of these resonant sized structures is not know and must be determined during simulation. This method is introduced by way of an example in which a resonant circular patch antenna is considered. The patch is initially assumed to be a high Q structure and the response to an excitation current is determined in terms of the patch resonant modes. The loading effect of the cavity on the patch is considered by appropriately modifying the Q of the patch resonant modes. This loading is determined by first applying the cavity Green's function to determine the field structure exterior to the patch, then calculating the energy stored within the resonator as well as the power which is dissipated. The patch response to an excitation current is then recalculated again using the updated Q. This procedure is iterated until a stable solution is determined. Once the resonator and patch fields are known, the driving point impedance of the patch is calculated.

Techniques are derived in the appendices which permit efficient application of harmonic balance circuit analysis to quasi-optical systems. A dual frequency set technique is described in appendix A. Time domain models are sampled at a rate which is sufficiently high to capture the modulation effects of the nonlinear models. The complete time domain sampled data set is transformed into a frequency domain spectrum. Due to the high sample rate, the spectrum is sufficiently broad to avoid

transform aliasing affects. A subset of this transform spectrum is used in linear element evaluation and in determining the simulation solution. This technique is shown to significantly reduce simulation time without unreasonable sacrifice of accuracy. The dual frequency set technique is particularly attractive for use in quasi-optical systems that are excited by arrays because it reduces the number of frequencies at which the lengthy cavity computations must be made and reduces the dimension of the error function.

A method is derived in appendix B for determining the analytic frequency domain derivatives of time domain nonlinear models using the multidimensional fast Fourier transform. This result is achieved by considering a matrix multiplication which is equivalent to the transform operation, then using the chain rule for differentiation to generate an expression for the frequency domain derivatives. The expression is then recast in terms of a transform operator and the available time domain derivatives. The resulting procedure allows analytic calculation of frequency domain derivatives for use in derivative based (e.g. Newton's method) circuit solving programs. This technique is implemented in a harmonic balance circuit simulator program then performance improvements are demonstrated. A multidimensional transform is required for the analysis of nonlinear oscillators in a quasi-optical cavity because the cavity resonant mode spectrum can result in oscillation at incommensurate frequencies.

5.2 Future Research

This dissertation opens the way for future research in both refinement of the Green's functions, and in application of the functions to modeling and simulation of quasi-optical systems.

5.2.1 Green's Function Refinements

The Green's functions in this dissertation were derived using various simplifying assumptions. These assumptions may not be applicable to quasi-optical systems under certain circumstances. Methods for refining the Green's functions by removing the assumptions will be presented.

The variable ψ_{mn} contains phase information which, in the denominators of $\bar{\mathbf{G}}\mathbf{e}_r$ and $\bar{\mathbf{G}}\mathbf{h}_r$, models the resonant behavior of the cavity. This resonance information is also contained within the eigenvalues γ_{mn} of (3.2), but only $|\gamma_{mn}|$ is used. An alternate derivation of $\bar{\mathbf{G}}\mathbf{e}_c$ and $\bar{\mathbf{G}}\mathbf{h}_c$ may be possible in uses the full information contained within γ_{mn} in lieu of ψ_{mn}.

The modal fields within the cavity were assumed to be approximately TEM. This assumption may be inadequate for sources which are not located near the $z = 0$ plane, particularly when sources are located away from the z axis. This situation may arise when additional arrays such as reactive tuning arrays, frequency doubling arrays, or wire grid filters are placed within the cavity. The Green's functions can be re-derived without using the TEM approximation. Weinstein [49] introduces a quasi-rectangular coordinate system that is derived from the oblate spheroidal coordinates and allows description of modes that are linearly polarized along the constant phase ellipsoidal surfaces. The modal field expressions in this coordinate system can be determined by applying potential theory in this coordinate system using the known reflector surface current density. These non TEM modal fields could then be used in a series expansion representing the resonant Green's functions.

Models for resonant sized antennas or apertures require calculation of U_e and U_m. Calculation of each of these stored energy terms requires evaluation of the

terms

$$\int_{\mathbf{\Omega}} E^{+}_{mn}(E^{-}_{mn})^{*}dv = \int_{\mathbf{\Omega}} (E^{+}_{mn})^{2}dv. \tag{5.1}$$

This volume integral is too cumbersome to compute during simulation and thus must be evaluated analytically prior to simulation. This remains to be done, but may be accomplished as follows. Equation (5.1) is computed as an iterated integral. The field E^{+}_{mn} should be expressed in oblate spheroidal coordinates, then (5.1) becomes [64]

$$a^3 \int_0^{\pi/2} \int_0^{2\pi} \int_0^{\operatorname{arcsinh}(D/a)} (E^{+}_{mn}(\theta,\phi,\eta))^2 (\cosh^2\eta - \sin^2\theta)\cosh\eta\,\sin\theta d\theta d\phi d\eta \tag{5.2}$$

where $2a$ is the interfocal distance of the coordinate system. Equation (5.2) can then be approximated using asymptotic expansion techniques [65]. For practical systems (5.2) would need to be evaluated for only a few of the lower order modes.

At this time, easy calculation of γ_{mn} has only been possible for resonators with rectangular apertures. In this case, the second order integral equation can be separated into two first order integral equations. It is possible to separate the second order integral equation in cylindrical coordinates for circular aperture reflectors [66]. In this case, $\bar{\mathbf{G}}\mathbf{e}_c$ and $\bar{\mathbf{G}}\mathbf{h}_c$ can be easily written for circular aperture cavities by substituting appropriately normalized Laguerre-Gaussian function for the Hermite-Gaussian functions in (3.40).

5.3 System Design

The theoretical combining efficiency as well as the optimal array geometry for an array of antennas radiating into an open resonator have not been determined. The optimal radiator spacing can easily be determined for a fixed number of radiators by using $\bar{\mathbf{G}}\mathbf{e}_c$ and assuming that each oscillator operates in phase. An array of

small antennas can be considered. Most small antennas are approximately isotropic radiators in a half space. Coupling to the TEM_{00} mode and radiation losses can be studied using the Green's functions. It is evident that coupling to the TEM_{00} mode is strongest for oscillators which are packed closely to the point $x = 0$, $y = 0$. This close spacing reduces the array aperture which results in increased radiation loss. The theoretical combining efficiency can be computed once the optimal spacing is found. The effect of element nonuniform amplitude oscillations can be studied using a circuit simulator and simple models for nonlinear elements. The next step in a design would be to impedance match each solid state device to its antenna.

The resonator Green's functions can be used to study novel methods for coupling energy from active arrays into the cavity. Several practical problems arise if a substrate containing active devices and antennas is placed within the cavity. Wavebeams are reflected at the dielectric interface which modifies the form of $\mathbf{E}_S$, power is also dissipated in the dielectric. Bias lines are exposed to the cavity fields and can alter the system behavior. The thickness of dielectric which produces efficient radiators is unsuitable for good microstrip circuit performance. These difficulties can be avoided by use of an aperture coupling scheme which still allows use of monolithic circuits. In this scheme the bottom of the substrate ground plane forms the inside surface of the resonator planar reflector. Small apertures in the ground plane couple energy from each oscillator into the resonator. It has been observed that small apertures can be used for coupling into quasi-optical resonators without disturbing the cavity mode structure [81]. The cavity Green's function can be used in conjunction with the theory of coupling by small apertures [40] to analyze this configuration.

One persistent problem with QR power combiners is the competition between various longitudinal modes. This difficulty will have to be resolved to enable prac-

tical QR devices. Single longitudinal modes can be eliminated by coupling to a wavemeter by a cavity aperture. Multiple modes may be eliminated by using a second low loss resonator. Resonant grid filters can also be used to eliminate oscillation over broad frequency bands. Antireflection techniques should be studied for grid filters.

References

[1] E. A. Wolff and R. Kaul, *Microwave Engineering and Systems Applications,* p. 476, Wiley, 1988.

[2] R.J.Dinger, D.J.White, and D.R. Bowling, "10 GHz Space Power Combiner with Parasitic Injection Locking," *Electron. Letters,* V.23, n.8, pp.397-398, 20 Feb. 1987

[3] J. W. Mink, "Quasi-Optical Power Combining of Solid-State Millimeter-Wave Sources," *IEEE Trans on Microwave Theory and Tech.*, vol MTT-34 Feb, 1986, pp. 273-279.

[4] P. L. Heron, G. P. Monahan, J. W. Mink, F. W. Schwering, and M. B. Steer, " Impedance matrix of an antenna array in a quasi-optical resonator," accepted for publication in *IEEE Trans on Microwave Theory and Tech.* Oct. 1993.

[5] P. L. Heron, F. W. Schwering, G. P. Monahan, J. W. Mink, and M. B. Steer, "A dyadic Green's function for the plano-concave quasi-optical resonator," submitted for review to *IEEE Microwave and Guided Wave Letters.*

[6] P. L. Heron, G. P. Monahan, J. E. Byrd, M. B. Steer, F. W. Schwering, and J. .W. Mink, "Circuit level modeling of quasi-optical power combining open cavities," accepted for presentation and publication by the *1993 IEEE Symposium on Microwave Theory and Tech.*

[7] J. C. Wiltse and J. W. Mink, "Quasi-Optical Power Combining of Solid-State Sources," *Microwave Journal,* Feb 1992, pp.144-156.

[8] K. J. Cogan, F. C. De Lucia, and J. W. Mink, "Design of a millimeter wave quasi-optical power combiner for IMPATT diodes," *SPIE*, vol. 791 1987.

[9] D. B. Rutledge et.al.,"Quasi-Optical Power-Combining Arrays," *1990 IEEE MTT-S International Symposium Digest*, pp. 1201-1204.

[10] Z. B. Popovic, R. M Weikle II, M. Kim and D. B. Rutledge, "A 100-MESFET Planar Grid Oscillator," *MTT Trans.*, vol 39, NO2, Feb. 1991.

[11] Z. B. Popovic, M. Kim, and D. B. Rutledge, "Grid oscillators,"Int Journal of Infrared and Millmeter Waves," Vol. 9, No. 11, pp. 1003-1010, 1988.

[12] Z. B. Popovic, R. M Weikle II, M. Kim, K. Potter, and D. B. Rutledge, "Bar–grid oscillators," *IEEE Trans. Microwave Theory and Tech.,* Vol. 19, pp. 193-200, February 1990.

[13] S. Bundy, T. Mader,and Z. Popovic, "Quasi–optical array VCO's," *1992 MTT Symposium Digest,* pp. 1539–1542.

[14] M. Nakayama, M, Hieda,T. Tanaka, and K. Mizuno,"Millimeter and Submillimeter Wave Quasi-Optical Oscillator with Multi-Elements," *1990 IEEE MTT-S International Symposium Digest*, pp. 1209-1212.

[15] R. Weilke, M. Kim, J. Hacker, M. DeLisio, and D. Rutledge, "Planar MESDET grid oscillators using gate feedback," *IEEE Trans. Microwave Theory and Tech.,* Vol. 40, No. 11, pp. 1997–2003, November 1992.

[16] R. Weilke, M. Kim, J. Hacker, M. DeLisio, Z. Popovic and D. Rutledge, "Transistor oscillator and amplifier grids," *Proceedings of the IEEE,* Vol. 80, No. 11, pp. 1800-1809, November 1992.

[17] A. Mortazawi and T. Itoh, "A Periodic Second Harmonic Spatial Power Combining Oscillator," *1990 IEEE MTT-S Digest*, pp.1213-1216.

[18] A. Mortazawi and T. Itoh, "A Periodic Planar Gunn Diode Power Combining Oscillator," *IEEE Trans on Microwave Theory and Tech.*, v.38,n.1, pp.86-87, Jan.1990

[19] J. Birkeland and T. Itoh, "Two-Port FET Oscillators with Applications to Active Arrays," ,*IEEE Microwave and Guided Wave Letters,* v.1, n.5, pp.112-113, May 1991

[20] J. Birkeland and T. Itoh, "Spatial Power Combining using Push-Pull FET Oscillators with Microstrip Patch Resonators," *1990 MTT-S Digest,* pp.1217-1220.

[21] J. Birkeland and T. Itoh, "A 16 element quasi-optical FET oscillator power combining array with external injection locking," *IEEE Trans on Microwave Theory and Tech.*, v. 40, n. 3, March 1992, pp. 475–481.

[22] K. D. Stephan, "Inter-Injection-Locked Oscillators for Power Combining and Phased Arrays," *IEEE Trans. Microwave Theory Tech.,* v. MTT-34, n. 10,pp. 1017-1025, Oct.1986.

[23] K. D. Stephan and S. Young, "Mode Stability of Radiation-Coupled Interinjection-Locked Oscillators for Integrated Phased Arrays," *IEEE Transactions on Microwave Theory and Techniques,* v.36, no.5, May 1988.

[24] K. D. Stephan and T. Itoh, "Recent Efforts on Planar Components for Active Quasi-optical Applications," *1990 IEEE MTT-S Digest,* pp.1205-1208

[25] K. D. Stephan, E. R. Brown, C. D. Parker, W. D. Goodhue, C. L. Chen, and T. Sollner, "Resonant-Tunneling Diode Oscillator Using a Slot-Coupled Quasi-Optical Open Resonator," *Electron. Lett.,* v.27, n.8, pp.647-649, 11 April, 1991

[26] W. P. Shillue and K. D. Stephan, "A technique for the measurement of mutual impedance of monolithic solid–state quasi-optical oscillators," *Microwave and Optical Technology Letters,* Vol. 3, No. 12, December, 1990.

[27] C.Xue and Q. Wang, "Discussion of the Source-Array Plane Location in the Quasi-Optical Cavity for Solid State Power Combining," *Int. Journal Infrared and Millimeter Waves,* v.9, n.8, pp.725-731, 1988

[28] M. Hieda, M. Nakayama, K. Mizuno, T. Ajikata, and D. B. Rutledge, "Quasi-optical resonator for millimeter and submillimeter wave solid-state sources," *Proceedings of the SPIE,* Vol: 1039 p. 55-6, 1988

[29] Q. Wang, C. Xue, H. Li, and F. Wu, "Optimized Design of Quasi-Optical Source-Array of Solid State Power Combiner at Frequency 100 GHz," *Int. Journal Infrared and Millimeter Waves,* v.11, n.11, pp.1269-1283, 1990

[30] J. X. Ge, S. F. Li, and Y. Y. Chen, "Millimetre Wave Quasioptical Power Combiner," *Electronics Letters*," March 1991.

[31] K. Chang and C. Sun, "Millimeter-Wave Power-Combining Techniques," *IEEE Trans. Microwave Theory Tech.,* v.MTT-31, n.3, pp.91-107, Feb.1983

[32] L. Wandinger and V. Nalbandian, "Quasioptical millimeter-wave power combiner," *Proc. 6th Int. Conf. Infrared and Millimeter Waves.*

[33] R. A. York and R. C. Compton, "Quasi-Optical Power Combining Using Mutually Synchronized Oscillator Arrays," *IEEE Trans. Microwave Theory Tech.,* v.39, n.6, pp.1000-1009, June 1991.

[34] R. A. York, and R. C. Compton, "Mode-Locked Oscillator Arrays," *Microwave and Guided Wave Letters,* V-1, NO-8, Aug 1991.

[35] K. A. Hummer and K. Chang, "Spatial power combining using active microstrip patch antennas," *Microwave and Optical Technology Letters,* Vol. 1, N0. 1, pp. 8-9, March 1988.

[36] N. Camilleri and B. Bayraktaroglu, "Monolithic Millimeter-wave IMPATT Oscillator and Active Antenna," *IEEE Trans. Microwave Theory Tech.,* v.36, n.12 pp.1670-1676, Dec.1988

[37] K. A. Lee and M. A. Frerking,"Experimental Results of a High Q Quasioptical Reflection Cavity ," *Int. Journal of IR. and Millimeter Waves,* v.10 n.7, 1989 pp.789-803.

[38] P. F. Goldsmith, "Quasi-optical techniques," *Proceedings of the IEEE,* Vol. 80, No. 11, Nov. 1992, pp. 1729-1747.

[39] R. E. Collin, *Foundations for Microwave Engineering,* McGraw Hill, 1966.

[40] R. E. Collin, *Field Theory of Guided Waves,* IEEE Press, 1991. p. 36.

[41] C. A. Balanis, *Antenna Theory, Analysis and Design,* Harper and Row, 1982.

[42] G. Goubau and F. Schwering, "On the Guided Propagation of Electromagnetic Wave Beams," *IRE Trans. on Antennas and Prop.,* May 1961, pp.248-256.

[43] G. Goubau, "Beam Waveguides," in *Advances in Microwaves*,vol.3, New York: Academic Press 1968, pp 67-126.

[44] G. Goubau, "Optical relations for coherant wave beams,"*Proceedings Symposium on Electromagnetic Theory and Antennas, Copenhagen,* June 25–30, 1963.

[45] F. Schwering, "Reiterative wave beams of rectangular symmetry," *Sonderdruk aus Archiv Der Elektrischen Ubertragung,* pp. 555–564, 1961.

[46] J. Beyer and E. Scheibe, "Higher modes in guided electromagnetic–wave beams," *IRE Trans on Antennas and Prop,* pp. 349–350, May 1962.

[47] T. Li, "Mode selection in an aperture–limited concentric maser interferometer," *Bell Syst. Tech. Journal,* pp. 2609–2620, Nov. 1963.

[48] T. Li, "Diffraction loss and selection of modes in maser resonators with circular mirrors," *Bell Syst. Tech. Journal,* pp. 917–933, May 1965.

[49] L. A. Weinstein, *Open Resonators and Open Waveguides*, The Golem Press, 1969.

[50] G. D. Boyd and H. Kogelnik, "Generalized Confocal Resonator Theory," *Bell Sys. Tech. Jour.,* July 1962, pp.1347-1369.

[51] G. D. Boyd and J. P. Gordon, "Confocal Multimode Resonator for Millimeter Through Optical Wavelength Masers," *Bell Sys. Tech. Jour.,* March 1961, pp.489-509.

[52] G. Boyd, "The confocal resonator for millimeter through optical wavelength masers," *Advances in Quantum Electronics,* pp. 319–327, Columbia University Press, 1961.

[53] R. F. Soohoo,"Nonconfocal Multimode Resonators for Masers," *Proceedings of IEEE*, Jan.1963, pp.70-75.

[54] A. G. Fox and T. Li, "Resonant Modes in a Maser Interferometer," *Bell Sys. Tech. Jour.,* March 1961, pp.453-489.

[55] A. G. Fox and T. Li, "Modes in a Maser Interferometer with Curved and Tilted Mirrors ," *Proceedings of IEEE*, Jan. 1963, pp. 80-89

[56] R. W. Zimmerer *et. al.*, "Millimeter Wavelength Resonant Structures ," *IEEE Trans. Microwave Theory and Tech.*,March 1962 , pp.142-149.

[57] R. W. Zimmerer, "Spherical Mirror Fabry-Perot Resonators," *IEEE Trans. Microwave Theory and Tech.* Sept. 1963, pp.371-379.

[58] Flammer, *Spheriodal Wave Functions,* Stanford University Press, 1957.

[59] Stratton, Morse, Chu, Little and Corbato, *Spheriodal Wave Functions,* Willey 1956.

[60] K. Fujimoto, A. Henderson, K. Hirasawa, and J. R. James, *Small Antennas,* Research Studies Press LTD, 1987.

[61] K. Chang, *Handbook of Microwave and Optical Components V.3,* Wiley, 1990, p.173

[62] E. Jordan and K. Balmain, *Electromagnetic Waves and Radiating Systems,* Prentice–Hall 1976, pp. 479–480.

[63] C. Tai, *Dyadic Green's Functions in Electromagnetic Theory,* Intext Educational Publishers, 1971, p. 68.

[64] P. Moon and D. E. Spencer, *Field Theory Handbook,* Springer-Verlag 1988.

[65] J. P. Keener, *Principles of Applied Mathematics, Transformation and Approximation,* Addison-Wesley 1988.

[66] Private conversation with Gregory P. Monahan, Jan. 1993.

[67] A. Ushida and L.O. Chua, "Frequency-domain analysis of nonlinear circuits driven by multi-tone signals," *IEEE Trans. Circuits and Systems*, Vol. CAS-31, Sept 1984, pp. 766-779.

[68] K.S. Kundert, G.B. Sorkin, and A. Sangiovanni-Vincentelli, "Applying harmonic balance to almost-periodic circuits," *IEEE Trans. on Microwave Theory and Tech.*, Vol. 36, Feb 1988, pp. 366-377.

[69] V. Rizzoli, C. Cecchetti, A. Lipparini, and F. Mastri, "General-purpose harmonic balance analysis of nonlinear microwave circuits under multitone excitation," *IEEE Trans. Microwave Theory Tech.*, Vol. MTT-36, Dec 1988, pp. 1650-1660.

[70] C.R. Chang, M.B. Steer and G.W. Rhyne, "Frequency domain spectral balance using the arithmetic Operator Method," *IEEE Trans. Microwave Theory Tech.*, Vol. MTT-37 Nov 1989, pp. 1681-1688.

[71] P. L. Heron and M. B. Steer, "Jacobian calculation using the multidimensional fast Fourier transform in the harmonic balance analysis of nonlinear circuits," *IEEE Trans on Microwave Theory and Tech,* pp. 429-431, v. 38, n. 4, April 1990.

[72] P.L. Heron C.R. Chang and M.B. Steer, "Control of aliasing in the harmonic balance simulation of nonlinear microwave circuits," *IEEE MTT-S International Microwave Symposium Digest*, June 1989, pp. 355-358.

[73] V. Rizzoli, C. Cecchetti, A. Lipparini, and F. Mastri, "General-purpose harmonic balance analysis of nonlinear microwave circuits under multitone excitation," *IEEE Trans. Microwave Theory Tech.*, vol. MTT-36, Dec. 1988, pp. 1650-1660.

[74] R. Gilmore, "Nonlinear circuit design using the modified harmonic balance algorithm," *IEEE Trans. Microwave Theory Tech.*, vol. MTT-34, Dec. 1986, pp. 1294-1307.

[75] A. Ushida and L. Chua, "Frequency-domain analysis of nonlinear circuits driven by multi-tone signals," *IEEE Transactions on Circuits and Systems*," vol. CAS-31, Sept. 1984, pp. 766-799.

[76] K.S. Kundert, G.B. Sorkin, and A. Sangiovanni-Vincentelli, "Applying harmonic balance to almost periodic circuits," *IEEE Transactions on Microwave Theory and Techniques*," vol. MTT-36, No. 2, Feb. 1988, pp. 366-377.

[77] TOUCHSTONE, EEsof Inc., Westlake Village, CA, USA.

[78] SUPERCOMPACT, Compact Software, Patterson, NJ, USA.

[79] C.R. Chang, P.L. Heron and M.B. Steer "Harmonic balance and frequency-domain simulation of nonlinear microwave circuits using the block Newton method," *IEEE Trans. Microwave Theory Tech.*, vol. MTT-38 April 1990, pp. 431-434.

[80] R. Gilmore and M.B. Steer, "Nonlinear Circuit Analysis Using the Method of Harmonic Balance — a Review of the Art," (invited), *International Journal on Microwave and Millimeter Wave Computer Aided Engineering*, October 1990.

[81] D. H. Auston, R. I. Primich, and R. A. Hayami, "Further considerations of the use of Fabry-Perot resonators in microwave plasma diagnostics," in *Proceedings of the Symposium on Quasi-Optics, New York 1964,* Polytechnic Press N. Y., pp. 273-299.

[82] I. J. Bahl and P. Bhartia, *Microstrip Antennas,* Artech House Inc. 1980.

Appendix A

Control of Simulation Aliasing Error

A.1 Introduction

In industry the harmonic balance technique has gained almost universal acceptance for the simulation of microwave circuits. Microwave circuits often are comprised of numerous linear elements along with relatively few lumped nonlinear elements. The linear elements may be efficiently analyzed in the frequency domain and the nonlinear elements often have algebraic time-domain constitutive relations and are thus most conveniently analyzed in the time domain. Microwave circuits are thus ideally suited for efficient simulation using harmonic balance [73]–[76] as they may be effectively partitioned , see Fig A.1. In the case of oscillator arrays within a quasi-optical cavity, the nonlinear solid state sources are analyzed in the time domain, the antennas and cavity comprise a linear distributed network and are thus analyzed in the frequency domain. To accomplish the analysis, voltage phasors are estimated at the interface nodes. A sampled time domain current waveform for elements of the nonlinear sub-circuit is obtained by applying an inverse Fourier transform to the voltage phasors, this is used as the input to the constitutive relations of elements in the nonlinear circuit.

Next, the current waveform for the each nonlinear element is converted into a frequency spectrum by a Fourier transform. These phasors are equated, i.e. balanced, with the corresponding phasors for the currents flowing into the linear sub-circuit to obtain the simulation result.

While in pursuit of acceptable simulator performance, the user is faced with a trade-off between simulation accuracy and speed. This concern dictates the number of frequency components to be used in a particular analysis. Selection of a large set of analysis frequencies will enhance the simulation accuracy but at the expense of increased simulation time and computer memory. Acceptable accuracy and speed

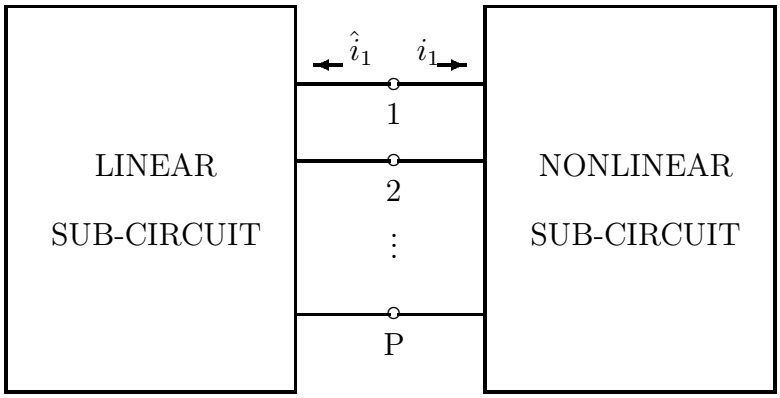

Figure A.1: Partitioning of a Microwave Circuit into a Linear and Nonlinear Subcircuit for Harmonic Balance Analysis.

can often be obtained by use of a relatively small number of analysis frequencies if the time-domain response of each nonlinear element is oversampled. The optimization process which determines the simulation solution is performed in the frequency domain, thus reduction of the number of analysis frequencies results in a more efficient simulation. If an analysis is to be performed for n antennas radiating into a quasi-optical system, the driving point impedance matrix will have n^2 terms (although, due to reciprocity, only $n(n+1)/2$ terms are unique). Each term, for a resonant sized antenna, requires considerable computation. So, reducing the size of the set of analysis frequencies is critical for efficient simulation.

The ability to oversample exists in a number of commercially available harmonic balance simulators ([77], [78]). The purpose of this appendix is to examine the contribution of aliasing to the error present in harmonic balance simulation. A rigorous treatment of aliasing is presented and practical guidelines are established for reducing aliasing by selection of a suitable oversampling rate. These guidelines allow a user to reduce aliasing to specified limits.

A.2 Harmonic Balance

A.2.1 Circuit Analysis

Harmonic balance simulators partition a circuit under analysis into a linear sub-circuit and a nonlinear sub-circuit. The steady state solution of the circuit can then be obtained by minimizing the total Kirchoff's circuit law error calculated at each node/edge in the nonlinear sub-circuit. Typically an error function, $\mathbf{E}$, is formed by comparing the response of the nonlinear sub-circuit, $\tilde{\mathbf{Y}}$ (node voltage phasors for nonlinear impedance elements and edge current phasors for nonlinear admittance elements), to the response of the linear sub-circuit, $\mathbf{Y}$, for a common set of independent analysis variables, $\mathbf{X}$ (node voltage phasors for nonlinear admittance elements, edge current phasors for nonlinear impedance elements). Thus $\mathbf{E}$ is a vector with elements

$$E_{k,n} = \tilde{Y}_{k,n} - Y_{k,n} \tag{A.1}$$

where k is a frequency index and n is a node index. The nonlinear calculations are performed element response back to the frequency domain ($\tilde{\mathbf{Y}}$). Iterative techniques, such as Newton's method, are required to minimize $\mathbf{E}$. In Newton's method all the $|E_{k,n}|^2$ are simultaneously minimized by performing the iteration

$${}^{i+1}\mathbf{X} = {}^{i}\mathbf{X} - ({}^{i}\mathbf{J}_{y,x}^{-1})({}^{i}\mathbf{E}) \tag{A.2}$$

where $\mathbf{J}$ is the Jacobian, and the leading superscript is the iteration index, and the set of frequencies used in the calculation of (B.4) is $\mathbf{\Omega}_a$. Formation and inversion of the Jacobian are expensive operations. If, for example, there are N circuit variables and K frequencies, the Jacobian will be a $(2NK)^2$ real matrix and Jacobian inversion will be an $O((2NK)^\alpha)$ operation where α is generally between 1.5 and 3 depending on the sparsity of the Jacobian. Simulator speed can be increased if the number of analysis frequencies is smaller as the size of the Jacobian matrix is then reduced. However, the resultant increase in simulation speed will invariably be accompanied by a reduction in simulation accuracy.

A.2.2 Fourier Transform

During harmonic balance simulation the independent variable at the n th node, $\mathbf{X}_n$, is inverse Fourier transformed to obtain the time-domain sampled waveform

$$\mathbf{x}_n = \mathcal{F}^{-1}(\mathbf{X}_n) \tag{A.3}$$

Then the dependent variable sequence $\tilde{\mathbf{y}}_n$ is calculated by applying the independent variable sequence to the device constitutive relation:

$$\tilde{\mathbf{y}}_n = \mathbf{h}\left(\mathbf{x}_n\right) \tag{A.4}$$

Subsequently $\tilde{\mathbf{y}}_n$ is transformed to the frequency domain to permit calculation of $\mathbf{E}$.

$$\tilde{\mathbf{Y}}_n = \mathcal{F}(\tilde{\mathbf{y}}_n) \tag{A.5}$$

Due to the sampled nature of the data, the transform is necessarily accomplished by use of a discrete Fourier transform (DFT). The exact nature of the Fourier transform depends upon the type of signal to be transformed. If the analysis signals are approximately band limited and all frequencies are harmonically related, then we can represent the operations in (B.1) and (B.3) as

$$\mathbf{x}_n = [x_m]_n = \left[\sum_{k=0}^{2K-1} X_k \exp(j(m\tau k\omega))\right]_n \tag{A.6}$$

and

$$\tilde{\mathbf{Y}}_n = \left[\tilde{Y}_k\right]_n = \left[\sum_{m=0}^{2M-1} \tilde{Y}_k \exp(\frac{1}{j}(m\tau k\omega))\right]_n \tag{A.7}$$

where $M = K$ and $\tau = \pi/(\omega M)$. In this case the DFT can be accomplished by matrix multiplication, or more efficiently by use of a fast Fourier transform (FFT) algorithm.

For N incommensurate (i.e. not harmonically related) input frequencies (B.1) and (B.3) become

$$\mathbf{x}_n = [x_{m_1 m_2 \ldots m_N}]_n = \left[\sum_{k_1=0}^{2K_1-1} \sum_{2K_2=0}^{2K_2-1} \cdots \sum_{k_N=0}^{2K_N-1} X_{k_1 k_2 \ldots k_N} \exp\left(j\left[k_1\omega_1 m_1\tau_1 + k_2\omega_2 m_2\tau_2 + \ldots + k_N\omega_N m_N\tau_N\right]\right)\right]_n \tag{A.8}$$

and

$$\tilde{\mathbf{Y}}_n = [Y_{k_1 k_2 \ldots k_N}] = \left[\sum_{m_1=0}^{M_1-1} \sum_{m_2=0}^{M_2-1} \cdots \sum_{m_N=0}^{M_N-1} y_{m_1 m_2 \ldots m_N} \exp\left[-j\left(m_1\tau_1 k_1\omega_1 + m_2\tau_2 k_2\omega_2 + \ldots + m_N\tau_N k_N\omega_N\right)\right]\right]_n \quad \text{(A.9)}$$

where $M_i = K_i$ and $\tau_i = \pi/(M_i\omega_i)$. Fourier transformation of these signals can be accomplished using the almost periodic discrete Fourier transform (APDFT) [76] or by use of a least mean square method [75]. The accuracy of these methods using a truncated spectrum can not be mathematically determined because of the arbitrary selection of sample times. However Fourier transformation can also be achieved using a multidimensional discrete Fourier transform (NDFT) and then bounds on accuracy can be evaluated. Thus the NDFT will be considered here. The NDFT has been implemented efficiently in a harmonic balance simulator using the multidimensional fast Fourier transform (NFFT) algorithm [73]. Advantages of the NFFT are it's excellent numerical stability, high speed, and compact size (transform matrices do not have to be stored) [80].

In the above representation of the signal components, the data may be conceptualized as points in a multidimensional space. In the frequency domain, each axis of the space corresponds to harmonics of a single (incommensurate) input frequency and points off the axis correspond to intermodulation components (with frequencies being integer combinations of the frequencies of the incommensurate tones). In the time domain, each coordinate direction corresponds to an advance in phase of the harmonics of a single input frequency.

It is important to note the direct relationship between the number of time-domain samples and the frequency-domain bandwidth of a transform. Nyquist's theorem dictates that in (A.7) $2K$ samples are needed to resolve the amplitudes of $(K/2)-1$ a.c. frequencies. For example, three samples are needed to resolve a single tone in the presence of d.c. Thus oversampling in the time domain corresponds to an increase in the DFT bandwidth. We can think of the transform as having a set of frequencies $\mathbf{\Omega}_t$ which is different from the analysis frequency set and $\mathbf{\Omega}_t \supseteq \mathbf{\Omega}_a$, the equality holding if oversampling is not used.

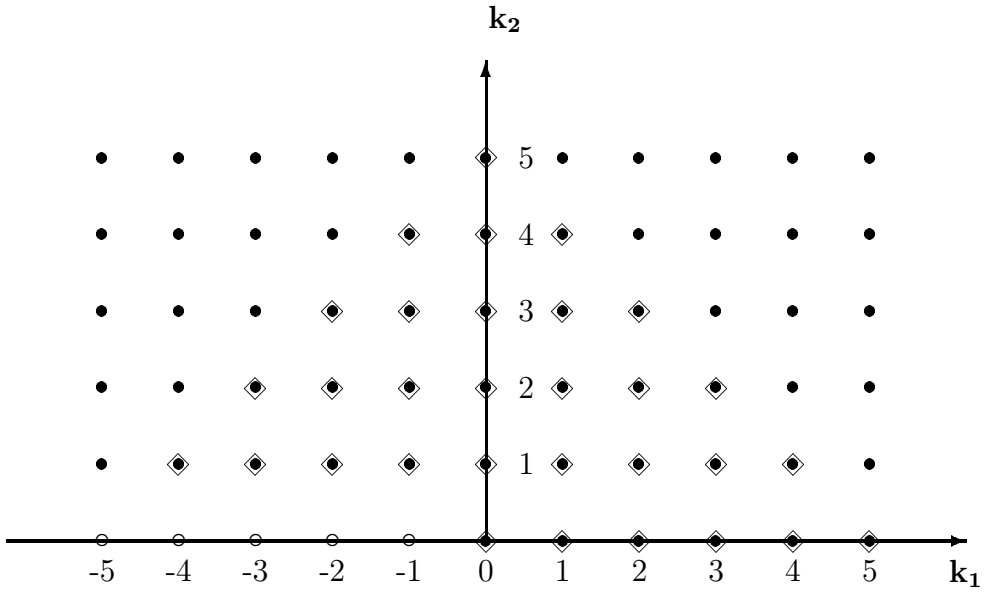

Figure A.2: Triangular ($\diamond$) and Rectangular ($\bullet$) Truncation Schemes for an Analysis with Two Incommensurate Input Tones for $\omega_2 > \omega_1$.

A.2.3 Spectrum Selection

Error in harmonic balance simulation due to analysis at a finite number of frequencies arises from two sources; 1) insufficient analysis bandwidth, i.e. $\mathbf{\Omega}_a$ too small, and 2) insufficient transform bandwidth, $\mathbf{\Omega}_t$ too small. These errors will be referred to respectively as analysis error and aliasing. Generally $\mathbf{\Omega}_a$ and $\mathbf{\Omega}_t$ are chosen using either the triangular or rectangular truncation schemes as depicted in Fig. A.2. However, if fast Fourier transformation is used, the choice of Ω_t is restricted to the rectangular truncation scheme. If insufficient analysis bandwidth is used, then the instantaneous bias applied to each nonlinear element will be inaccurate resulting in incorrect simulation results, this is analysis error. If the transform bandwidth is too small, then the operational characteristics of the nonlinear devices will be corrupted due to aliasing. Amplitude components of the device response which are at frequencies outside the transform bandwidth will add to those used in the transform. Thus the frequencies which are included in the transform will have coefficients which are corrupted by aliasing as the full spectrum 'folds' in on top of $\mathbf{\Omega}_t$.

Experience has shown that the simulation error arising from an analysis with a finite number of frequencies can be reduced by use of a relatively small set of fre-

quencies $\mathbf{\Omega}_a$, and a somewhat larger set of frequencies $\mathbf{\Omega}_t$. This is true because the simulation error can most often be attributed to aliasing. This point is illustrated in Fig. A.3 which shows the third harmonic output power for the simulation of a class-C BJT amplifier versus the number of analysis frequencies. This harmonic balance simulation was performed without oversampling (i.e. $\mathbf{\Omega}_t = \mathbf{\Omega}_a$). The horizontal asymptote represents the solution for a large number of analysis frequencies and is assumed to be the correct solution. The distance between the solid curve and the asymptote represents the combined effect of analysis error and aliasing. Normally these two sources of error can not be distinguished. Aliasing, however, can be performed manually as follows. During Fourier transformation the frequency components not included in Ω_t fold on to frequency components in Ω_t as indicated in Fig. A.4. So, a simulation with 35 frequencies was performed to permit approximate calculation of the amount of error due to aliasing alone. Since the asymptotic solution is approximated here, the analysis error is negligible. The voltage of the appropriate components (dependent upon the number of frequencies in the effective Ω_t) from the 35 frequency spectrum were added to the third harmonic. For example, with Ω_t including components up to the third harmonic, the 4th, 10th, 11th, 18th, 19th, 25th, 26th, 32nd and 33rd components were added to the voltage of the 3rd harmonic. The result is shown as the broken curve in Fig. A.3 and the proximity to the solid simulated curve indicates that, in this case, aliasing is the major contributor to simulation error.

A.3 Aliasing

In this section we examine aliasing theoretically and determine the minimum oversampling rate required to obtain a prescribed simulation accuracy. This is accomplished by examining the spectral error introduced by aliasing during the continuous Fourier transform of a sampled periodic signal. The result is extended to almost periodic signals when the transform is accomplished by an NDFT or an NFFT.

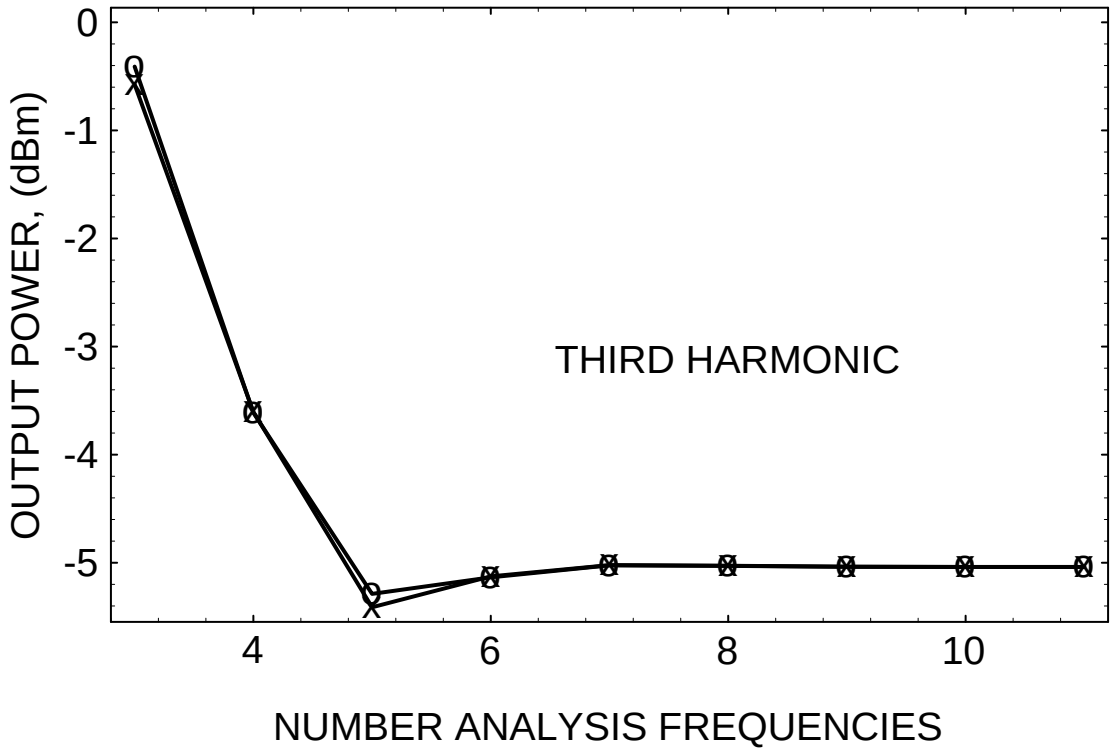

Figure A.3: Third Harmonic Voltage Amplitude vs. Number of Frequencies Used in Traditional Harmonic Balance Analysis of a Class-C BJT Amplifier. The Curve with (X) Data Points is a Simulation Result, the Curve With (o) Data Points is a Theoretical Result Assuming all Error is Due to Aliasing.

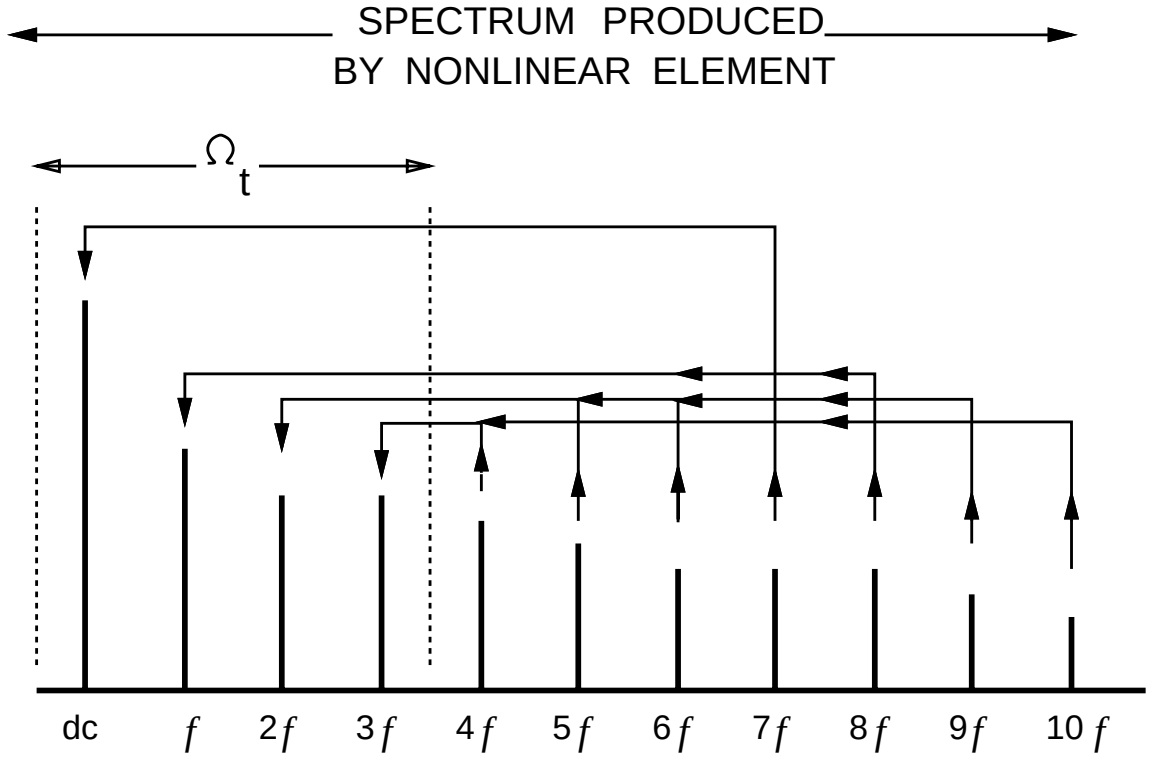

Figure A.4: Frequency Folding During Fourier Transformation. $\mathbf{\Omega}_t$ is the Set of Transform Frequencies.

A.3.1 Periodic Signals

Consider the continuous periodic signal

$$x(t) = \sum_{k=-K}^{K} a_k \exp(jk\omega_0 t)$$

where a_{-k} is the complex conjugate of a_k. Our aim is to recover the coefficients a_k from the signal $x(t)$ by sampling the signal and performing a transform operation on the samples. The spectrum is obtained first by observing the signal over a finite period of time. This effect is modeled by multiplying the signal by a rectangular window distribution

$$w(t,T) = H(t+T) - H(t-T)$$

where $H(t)$ is the unit Heaviside distribution. Next the windowed waveform, $x_w(t) = w(t,T)x(t)$, is sampled at discrete time instants. This may be accomplished by multiplying by a sampling impulse train $p(t,\tau_S)$ which, for periodic signals, has equally spaced sampling intervals so that

$$p(t,\tau_S) = \sum_{\ell=-\infty}^{\infty} \delta(t - \ell\tau_S)$$

The sampled data waveform is then

$$\hat{x}_w(t) = p(t,\tau_S)x_w(t) = p(t,\tau_S)w(t,T)x(t)$$

Now time-domain multiplication is equivalent to frequency-domain convolution, so the spectrum of the signal is

$$\mathcal{F}\left(\hat{x}_w(t)\right) = \mathcal{F}\left(p(t,\tau_S)\right) * \mathcal{F}\left(w(t,T)\right) * \mathcal{F}\left(x(t)\right) \tag{A.10}$$

where the Fourier transform operator is defined

$$\mathcal{F}(\cdots) \triangleq \int_{-\infty}^{\infty} (\cdots) \exp(-j2\pi ft)dt$$

and the individual frequency-domain distributions are

$$\mathcal{F}\left(x(t)\right) = \sum_{k=-K}^{K} a_k \delta(\omega - k\omega_0) \tag{A.11}$$

$$\mathcal{F}\left(w(t,T)\right) = \frac{t}{2\pi} S_a\left(\frac{\omega T}{2}\right) \tag{A.12}$$

$$\mathcal{F}\left(p(t,\tau_S)\right) = \frac{1}{\tau_S} \sum_{\ell=-\infty}^{\infty} \delta\left(\omega - \frac{2\pi\ell}{\tau_S}\right) \tag{A.13}$$

and $S_a(\cdots)$ is the sampling function. Substituting (A.11)–(A.13) into (A.10), expanding, and evaluating the frequency-domain spectrum at the discrete frequencies $\omega = p\omega_0$, yields the discrete spectrum of the sampled signal

$$\hat{X}_w(p\omega_0) = \mathcal{F}\hat{x}_w(t) = \frac{T}{2\pi\tau_S} \sum_{\ell=-\infty}^{\infty} \sum_{k=-K}^{K} a_k \mathrm{Sa}\left(\frac{T}{2}\left((p-k)\omega_0 - \frac{2\pi\ell}{\tau_S}\right)\right) \tag{A.14}$$

As can be seen, a consequence of sampling is that the entire spectrum is replicated and is offset in frequency by multiples of $2\pi/\tau_S$. The interference of these multiple spectra with the primary ($\ell = 0$) spectrum is called *aliasing*. To insure that the coefficient a_p is not corrupted by adjacent spectra, we can see from (A.14) that the condition that must be satisfied is

$$\tau_S \leq \left(\frac{\tau_0}{K+p+1}\right) \tag{A.15}$$

When all coefficients are to be recovered, including the $p = K$ term, (A.15) reduces to the standard sampling theorem. This result permits selection of an appropriate Fourier transform size based upon estimated bandwidth and simulation accuracy requirements. To simulate a circuit with frequency components having significant power up to $\omega = K\omega_0$ and obtain a solution at frequencies up to $\omega_p = p\omega_0$ that are not affected by aliasing[1], we find the required transform frequency set

$$\mathbf{\Omega_t} = \{\omega \mid \omega = i\omega_0\} \ ; \ i = 1, ..., (K+p+1) \tag{A.16}$$

If we assume that the default simulator sample rate for an analysis with p harmonics in $\mathbf{\Omega}_a$ is $\tau_p = \pi/(p\omega_0)$, then we can express the oversampling factor (osf) as

$$\text{osf } = \frac{\tau_S}{\tau_p} = \left(\frac{2p}{p+K+1}\right) \tag{A.17}$$

Another effect of the discrete transform is evident from (A.14). Due to finite observation time (windowing) the discrete spectrum is convolved with a sampling function. Spectral leakage occurs when a coefficient is corrupted by the sampling

[1]The dependent variable components with $\omega > \omega_p$ will alias onto the components with $\omega \leq \omega_p$ and erroneously contribute to their computed magnitude. Therefore spectral components are considered to be insignificant if their magnitude is less than the tolerable simulation error.

functions which are associated with tones in the same spectrum (constant ℓ). This does not create a problem if the signal is periodic when the ratio T/τ_0 is selected to be an integer as this results in nulls at $k\omega_0$ for all sampling functions associated with adjacent frequencies. Therefore the amplitude at each sampled frequency is independent of the amplitudes at all other frequencies (i.e. there is no leakage).

A.3.2 Aperiodic Signals

Aliasing during simulation of circuits which are driven by multiple incommensurate tones can be understood by applying the previous ideas to a multidimensional frequency space. This frequency space is complex and N-dimensional if there are N incommensurate input frequencies. The results of sampling and windowing are analogous to those discussed for the single input tone case with the operations of (A.14) performed in a hypervolume so that we now have an N-dimensional time-space. The extension requires that there is no spectral leakage due to the sampling operation. Thus the extrapolation is valid for an NFFT with appropriate choices of the sampling instants in each dimension of time-space. In particular, in each dimension of time-space, the sampling instants must be equally spaced over a period of the fundamental incommensurate tone associated with that dimension. With this choice of sampling instants, sampling function nulls occur at the frequency components not in the particular dimension of frequency-space being examined, as required. This is not the case with the almost periodic Fourier transform [75] as the sampling nulls do not, in general, coincide with any frequency components.

Application of (A.15) to the multi-tone case requires that we assume the shape of the hypervolume in N-space which contains the significant power. If we assume that the spectrum forms a hypercube (this is just the conventional rectangular truncation scheme in the two incommensurate tone case), then (A.15) must be simultaneously satisfied in each of the N dimensions. That is,

$$(\tau_S)_r \leq \left(\frac{\tau_r}{K_r + p_r + 1} \right) \; ; \; r = 0, ..., N \tag{A.18}$$

Similarly the minimum oversampling factor in the rth dimension is

$$(\text{osf})_r = \left(\frac{2p_r}{K_r + p_r + 1} \right) \tag{A.19}$$

	1	**3**	**7**	**15**
1	8.880	8.920	8.921	8.921
3	9.063	9.120	9.124	9.124
7	9.062	9.121	9.125	9.125
15	9.061	9.121	9.125	9.125

Table A.1: Output Power (dBm) for Large Signal Analysis of a MESFET Amplifier Driven by Two Incommensurate Tones vs. Highest Order of Intermodulation used in the FFT for f_1 (Row) and f_2 (Column).

Table A.1 illustrates the effect of aliasing in two dimensions during the large signal simulation of a MESFET amplifier. The amplifier was driven by two incommensurate input frequencies, f_1 with an input power of 1.0 dBm, and f_2 with an input power of 3.0 dBm. A rectangular frequency truncation scheme with the frequencies determined by $K_1 = K_2 = 1$ was used in the Newton method and linear calculations. The row and column heading of table A.1 indicate the order of intermodulation used by the 2-D FFT in the f_1 and f_2 directions respectively. Table entries represent the amplifier output power (dBm) at the frequency f_1 and aliasing is seen to affect the solution for transforms using less than $K_1 = K_2 = 7$.

An important, and expected, feature of multidimensional transforms is suggested in table A.1. If a transform is of sufficiently high order in all dimensions but one, all frequency domain coefficients may be corrupted due to aliasing. In other words, (A.18) must simultaneously be satisfied in each dimension. Therefore the elimination of aliasing in multifrequency simulation necessitates the use of a large set of transform frequencies.

A.4 Results and Discussion

Dual-frequency-set harmonic balance has been incorporated into *FREDA*, a general nonlinear microwave circuit simulation program. FREDA uses a modification of the Sămanskii method with a block Newton iteration step to solve the system determining equations [79]. Harmonic balance simulation using either the DFT, APDFT, or

NFFT transform schemes is available.

A MESFET amplifier was simulated under single tone large signal conditions using the APDFT and both traditional and dual-frequency-set harmonic balance. The results are presented in Fig. A.5. During traditional harmonic balance simulation the solution was observed to be stable for sixteen or more a.c. analysis and transform frequencies (solid lines). For comparison a dual-set analysis was performed using the APDFT and sixteen constant a.c. transform frequencies with a variable number of analysis frequencies (broken line). Virtually the same result was obtained using only six analysis frequencies as for traditional simulation with sixteen frequencies. Dual frequency set analysis with six analysis frequencies required 998 kB (kilobytes) and 2.6 s on a DECstation 3100[2] (rated at 12-13 VAX 11/780 MIPs). Similar traditional analysis with sixteen a.c. frequencies required 2088 kB and 16.9 s. With the FFT method, a traditional simulation with fifteen a.c. frequencies required 1681 kB and 1.1 s. A similar dual frequency set FFT analysis with fifteen transform frequencies and six a.c. analysis frequencies required 685 kB and 0.5 s.

As a second example a class-C BJT amplifier was simulated using dual frequency set HB. The solution was observed to be stable for fifteen or more transform frequencies and any fixed number of analysis frequencies. Next, simulations were performed with 15 transform frequencies while the number of analysis frequencies was varied from 4 through 15. The relative solution error for the output power at the fourth harmonic versus relative simulation time are plotted in Fig. A.6 as functions of the number of analysis frequencies used.

The above examples are for periodic signals. The usefulness of dual frequency set HB analysis for the simulation of circuits with multi-tone excitation can be seen with the MESFET simulation using a 2D-FFT shown in table A.1. The output power was 8.17 mW (9.12 dBm) for a dual set simulation with rectangular truncation and using $K_1 = 3$ (f_1 direction) and $K_2 = 7$ (f_2 direction) to determine $\mathbf{\Omega_t}$ and $K_1 = K_2 = 1$ used to determine $\mathbf{\Omega_a}$. This result was obtained in 3.0 s using 756 kB. Traditional harmonic balance simulation using $K_1 = 4$ and $K_2 = 5$ (use of higher order intermodulation exceeded available computer memory) required 32 analysis frequencies, 9436 kB, and 170 s. The output power for f_1 was 8.49 mW (9.29 dBm).

[2]DECstation is a trademark of the Digital Equipment Corporation.

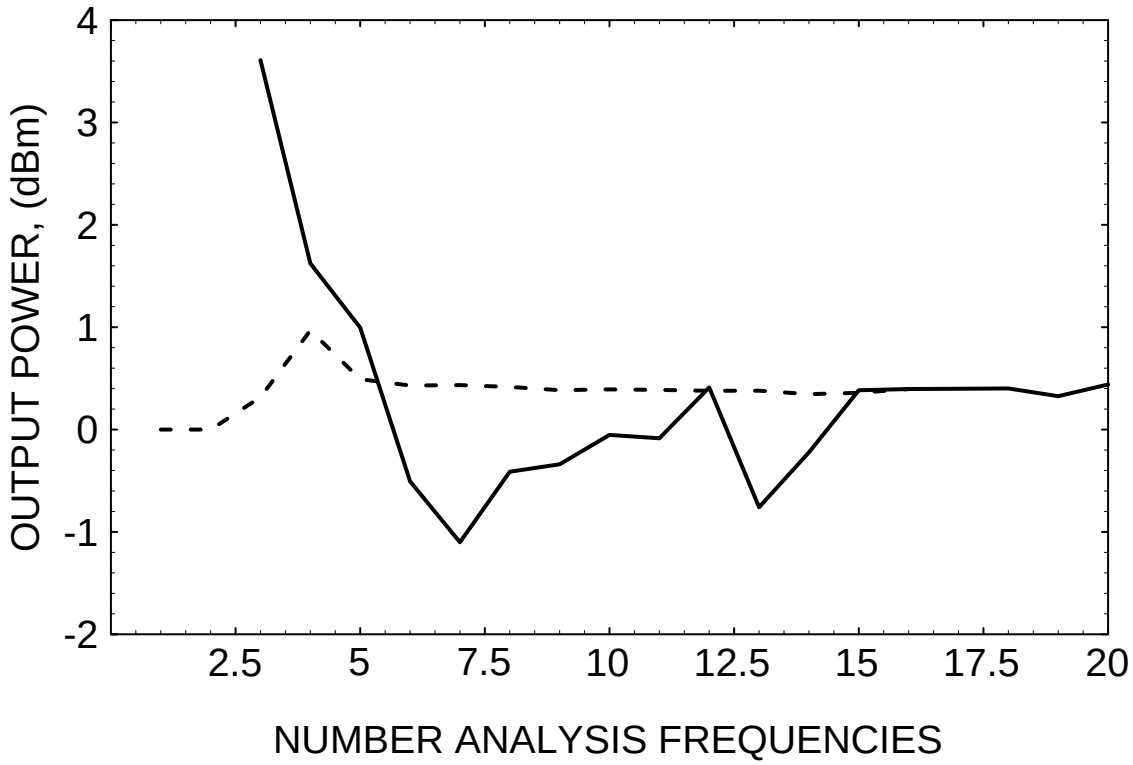

Figure A.5: Results of a MESFET Simulation Using; Traditional Analysis With APDFT (Solid Line), Dual-Frequency-Set (Broken Line) Analysis.

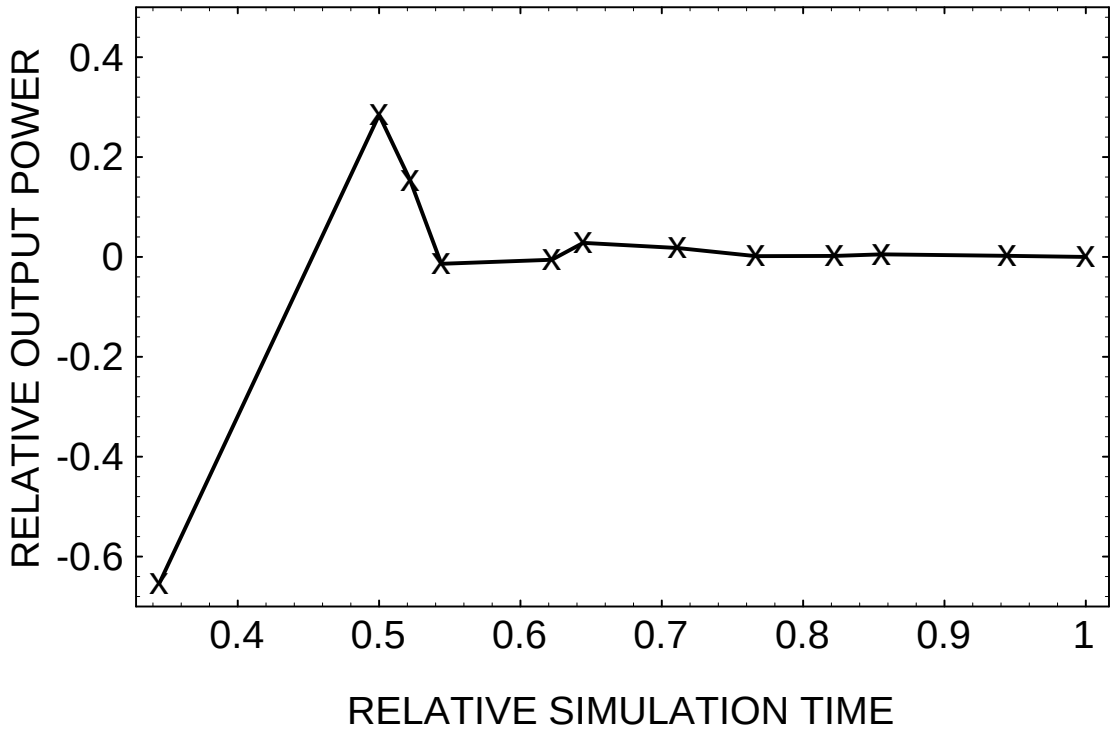

Figure A.6: BJT Amplifier Simulation Using the FFT With Dual-Frequency-Set Analysis. The Data Points Correspond to an Increasing Number of Analysis Frequencies, the Number of Transform Frequencies is Fixed.

The two results are within 4% of each other.

The tradeoff between accuracy and the analysis frequency set size was investigated in the simulation of a MESFET amplifier driven by two incommensurate tones. The 2D-FFT used a constant frequency set with rectangular truncation and $K_1 = K_2 = 7$, while a triangular truncation scheme was used to determine $\mathbf{\Omega_a}$. The power at the intermediate frequency is plotted in Fig. A.7 versus the triangular truncation index (K) for the analysis frequencies. Again it can be seen that the analysis frequency set can be much smaller than the transform frequency set.

A.4.1 Conclusion

There is a trade-off between simulation time and accuracy in the harmonic balance simulation of nonlinear circuits. In traditional harmonic balance analysis, using a single frequency set, a major contributor to the simulation error for typical microwave circuits is aliasing in the Fourier transform operation. However, large $\mathbf{\Omega_a}$ requires that much of the computation time be used in performing the harmonic balance iteration. Use of the dual-frequency-set harmonic balance method presented here can result in considerable time savings if the transform and evaluation of the nonlinear constitutive relationships can be performed efficiently. This technique may be applied to any type of harmonic balance simulator regardless of the optimization method used. However, the relative sizes of analysis error and error due to aliasing will depend upon the nature of the nonlinearities in the circuit, the input power level, and the impedance presented to each nonlinear element by the remainder of the circuit.

Through a theoretical analysis of aliasing, guidelines for selecting a minimal transform frequency set were established as a function of the desired analysis frequency set and the estimated signal bandwidth. Furthermore, efficient NFFT algorithms require that the number of frequencies be a power of 2 in each dimension. Thus the use of a multidimensional FFT leads naturally to dual-set analysis with a large transform frequency set and a reduced analysis frequency set.

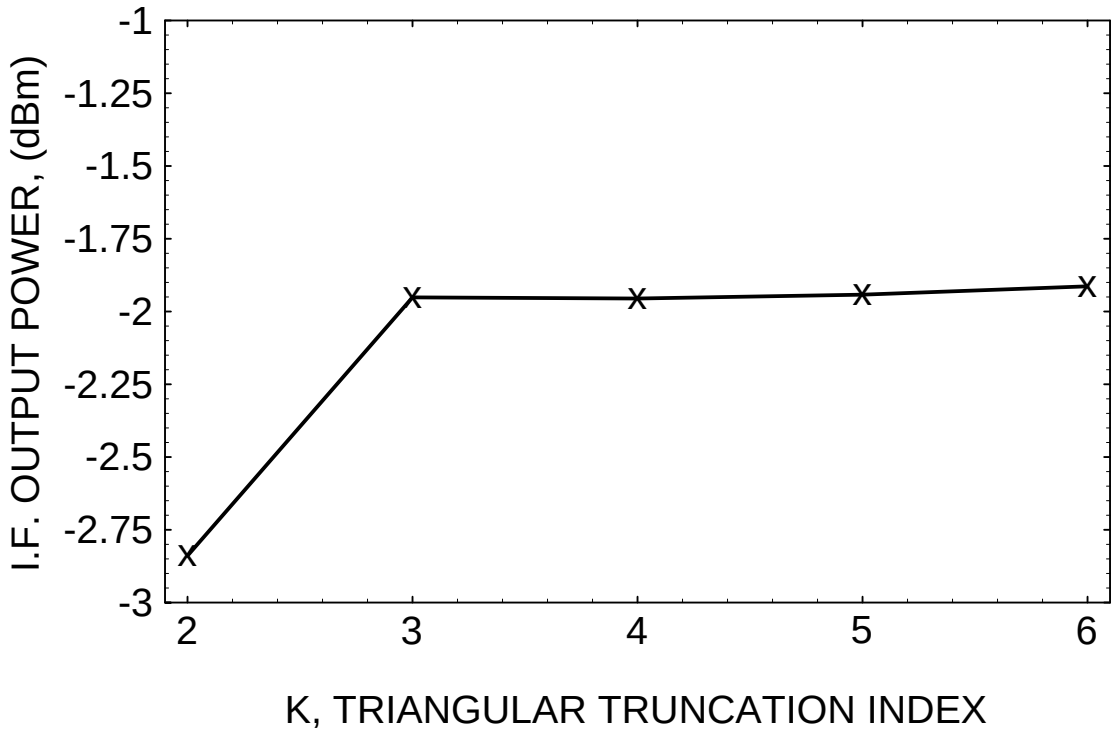

Figure A.7: I.F. Power vs. Triangular Truncation Index (K) in the Two Tone Simulation of a MESFET Amplifier.

Appendix B

Jacobian Calculation using the Multidimensional Fast Fourier Transform

A technique is developed whereby the gradient of frequency domain simulation variables may be analytically determined using time domain derivative information and the multidimensional fast Fourier transform. It is shown that this technique can be efficiently implemented when a circuit is driven by any number of incommensurate input frequencies. A harmonic balance simulator is constructed which uses this technique to determine the entries of the Jacobian matrix which are needed in a quasi-Newton iteration scheme. A significant reduction of simulation time is observed when compared with a harmonic balance simulator that uses matrix multiplication based transforms.

B.1 Introduction

In the harmonic balance method of nonlinear analog circuit simulation, the linear subcircuit is analyzed in the frequency domain and the nonlinear subcircuit in the time domain. For simulations with multifrequency excitation, the time domain and frequency domain analyses have been interfaced using either the almost periodic discrete Fourier transform (APDFT) method [67, 68] or the multidimensional fast Fourier transform (NFFT) method [73]. The advantage of the APDFT is that computer implementation is relatively simple for an arbitrary number of incommensurate input frequencies. On the other hand the NFFT algorithm is computationally more efficient and exhibits superior numerical stability. An alternate method to that used by Rizzoli *et.al* [73] is presented here in which the Jacobian is calculated using the NFFT. This method has the advantage that frequency domain derivatives may be computed for every frequency contained in the transform. It can also be used in

conjunction with the block Newton iteration scheme [70].

B.2 Harmonic Balance

Harmonic balance analysis proceeds by first selecting a set of frequency domain analysis variables at every edge/node which is common to both the linear and nonlinear portions of the circuit. The frequency domain independent variable is $\mathbf{X}$, and for impedance (admittance) type elements $\mathbf{X}$ is a set of current (voltage) phasors, while the dependent variable, $\mathbf{Y}$, is a set of voltage (current) phasors. Lower case variables will be used to indicate time domain quantities.

The independent and dependent variables at a single node or edge will be denoted by the subscript n. Absence of this subscript will indicate the collection of *all* independent or dependent variables in the simulation. For example; $\mathbf{X}_n$ represents the frequency domain independent variable containing all analysis frequencies at the n th node/edge, and $\mathbf{y}$ is the collection of the time domain dependent variables at *every* node/edge and sample time.

The objective of the harmonic balance procedure is to "balance" the response of the nonlinear elements ($\mathbf{Y}$) to that of the linear elements ($\tilde{\mathbf{Y}}$). Defining the forward and inverse transform operators as $\mathcal{F}$ and $\mathcal{F}^{-1}$ respectively, the "balance point" is determined iteratively as follows. During each iteration and at each analysis node/edge an updated estimate of $\mathbf{X}_n$ is inverse Fourier transformed into the time domain,

$$\mathbf{x}_n = \mathcal{F}^{-1}(\mathbf{X}_n) \tag{B.1}$$

and applied as input to the constitutive relations of a nonlinear element. This yields the time domain response ($\mathbf{y}_n$) for the present iterate of the dependent variable:

$$\mathbf{y}_n = \mathbf{h}(\mathbf{x}_n) \tag{B.2}$$

This is then Fourier transformed to the frequency domain,

$$\mathbf{Y}_n = \mathcal{F}(\mathbf{y}_n) \tag{B.3}$$

and compared with the response of the linear circuit to generate the error function E, $E = \|\mathbf{E}\|$ where $\mathbf{E} = [E_{k,n}] = \left[Y_{k,n} - \tilde{Y}_{k,n}\right]$ where the subscript k indexes the frequencies and n indexes the edges/nodes of elements $E_{k,n}$ of the matrix $\mathbf{E}$.

The error function is minimized by iteratively selecting better estimates for all independent variables. Generally, methods using first derivative information, known as quasi-Newton methods, are preferred. For each iteration the updated version of all independent variables is calculated using

$$^{i+1}\mathbf{X} =^{i} \mathbf{X} - (^{i}\mathbf{J}^{-1})(^{i}\mathbf{E}) \tag{B.4}$$

where the leading superscript is the iteration index and $^{i}\mathbf{J} =^{i} (\partial\mathbf{E}/\partial\mathbf{X})$ is the Jacobian matrix or an approximation to the Jacobian matrix.

B.3 NFFT

The harmonic balance algorithm can be generalized to signals having N incommensurate input frequencies by using a multidimensional Fourier transform. The operations in (B.1) and (B.3) then become

$$x_{\mathbf{m},n} = \frac{1}{|\mathbf{M}|} \sum_{k_1=0}^{M_1-1} \sum_{k_2=0}^{M_2-1} ... \sum_{k_N=0}^{M_N-1} X_{\mathbf{k},n} \exp \frac{2\pi}{j} \left(\frac{k_1}{M_1} m_1 + \frac{k_2}{M_2} m_2 + ... + \frac{k_N}{M_N} m_N \right) \tag{B.5}$$

and

$$Y_{\mathbf{k},n} = \sum_{m_1=0}^{M_1-1} \sum_{m_2=0}^{M_2-1} ... \sum_{m_N=0}^{M_N-1} y_{\mathbf{m},n} \exp 2j\pi \left(\frac{m_1}{M_1} k_1 + \frac{m_2}{M_2} k_2 + ... + \frac{m_N}{M_N} k_N \right) \tag{B.6}$$

where $|\mathbf{M}| = \Pi^N |M_i|$ and the subscripts $\mathbf{k}$ and $\mathbf{m}$ are multi-indices which represent $[k_1 k_2 ... k_N]$ and $[m_1 m_2 ... m_N]$ respectively. The operations in (B.5) and (B.6) are most efficiently implemented using an NFFT. In this algorithm, the complex frequency domain coefficients, $X_{\mathbf{k},n}$ and $Y_{\mathbf{k},n}$, may be thought of as belonging to an N-dimensional frequency space (elements of an N-dimensional matrix). Each dimension in this space corresponds to a particular input frequency. The frequency domain coefficient indexed by $\mathbf{k}$ corresponds to the amplitude of a phasor having frequency $\omega_{\mathbf{k}} = \omega_1 k_1 + ... + \omega_N k_N$. The phase factors $2\pi m_i k_i / M_i$ come from the product $\omega_{k_i} \tau_{m_i}$ where $\omega_{k_i} = \omega_i k_i$ and the discrete evaluation times are $\tau_{m_i} = 2\pi m_i / \omega_i$. To satisfy the Nyquist sampling criterion we let the k_i th index reference frequencies up to the $(M_i/2 - 1)$ th harmonic of ω_i (coefficients for negative, Nyquist and d.c.

frequencies account for the other $M_i/2+1$ terms). Similarly the time domain coefficients $x_{\mathbf{m}}$ and $y_{\mathbf{m}}$ can be viewed as elements of a multidimensional sample matrix and the phase associated with harmonics of the ω_i th input frequency varying as we traverse the matrix along the i th dimension (i.e. as the index m_i increases the phase associated with the ω_i th frequency advances).

We thus have a multidimensional time space and the signals $\mathbf{y}_n$ and $\mathbf{x}_n$ cannot be related to any real physical signal. The time domain constitutive relationships of nonlinear elements are constrained to be algebraic, i.e. have no memory, due to the absence of an identifiable sequence of time samples. This is not a restriction as Newton based harmonic balance simulators generally require that constitutive relations be algebraic. Nonlinear inductors, capacitors and other elements having constitutive relations involving derivatives with respect to time are handled through multiplication by an appropriate power of $j\omega$ in the frequency domain.

In the remainder of this paper we shall consider the data to be arranged in matrices. An example of the notation which will be used is

$$\frac{\partial \mathbf{y}_n}{\partial x_{\mathbf{m},n}} = \left[\frac{\partial y_{\mathbf{p}}}{\partial x}\right]_n$$

The left side of the equation states that we are taking the partial derivative of the matrix of the time domain dependent variable ($\mathbf{y}$) at all sample instants with respect to the dependent variable at one particular sample instant ($x_{\mathbf{m}}$). Here boldface type and absence of a subscript indicates a vector or matrix quantity with the index varying throughout the range of the (suppressed) subscript. Roman type and presence of a subscript indicate that we are selecting one particular scalar value. When differentiation is performed, the node index n indicates that we are performing this operation at one particular node/edge of the dependent variable and one particular node/edge of the independent variable. The node/edge in each case may be different but we will use the same n in each case to avoid additional complexity. On the right side of the previous equation, the square brackets indicate a matrix, each element of which is indicated by the enclosed quantity. In this example, matrix elements are indexed by the subscript $\mathbf{p}$ and derivatives are taken with respect to one fixed frequency component x. When subscripts are present inside the brackets they are free to vary over their range, absence of a subscript

indicates a single fixed element. Note that the subscript convention for variables outside brackets is the opposite to that used for matrix elements.

B.4 Jacobian Calculation

The harmonic balance procedure requires determination of the frequency domain derivatives $\partial\mathbf{Y}/\partial\mathbf{X}$. These can be calculated from the time domain derivatives

$$\mathbf{g}_n = [g_{\mathbf{pm}}]_n = \left[\frac{\partial y_{\mathbf{p}}}{\partial x_{\mathbf{m}}}\right]_n = \left[\frac{\partial h(x_{\mathbf{p}})}{\partial x_{\mathbf{m}}}\right]_n \tag{B.7}$$

which are available from the nonlinear device time domain constitutive relations. We may express (B.7) as

$$\mathbf{g}_n = [\delta_{\mathbf{pm}} g_{\mathbf{pm}}]_n \tag{B.8}$$

where $\delta_{\mathbf{pm}}$ is the Kronecker delta. A consequence of algebraic time domain constitutive relationships is that an element $g_{\mathbf{pm}} = 0$ if $\mathbf{p} \neq \mathbf{m}$. Here we develop a procedure for calculating the frequency domain derivatives from the time domain derivatives when an NFFT is used to accomplish transformation. Difficulties arise because of the multidimensional nature of the data and the fact that the transform is accomplished by a linear operator rather than through multiplication by a matrix.

From (B.6) we see that each frequency domain coefficient $Y_{\mathbf{k},n}$ is a function of all time domain samples, the $y_{\mathbf{m},n}$'s. Similarly, from (B.5), we see that each time domain sample $x_{\mathbf{m},n}$ is a function of all frequency domain coefficients, the $X_{\mathbf{k},n}$'s. This indicates that the transform should operate on the coefficients as if they were a vector rather than an N-dimensional matrix (as implied by the multiple indices). Thus the collection of all frequency domain or time domain coefficients will be treated here as a vector. This will be indicated by a hat ($\hat{.}$) above the frequency or time domain coefficient. For example, $\hat{\mathbf{x}}_n$ represents a vector containing all the instantaneous coefficients, $x_{\mathbf{m},n}$, and is obtained by concatenating the rows of $\mathbf{x}_n$. We will assume that the right-most index in $\mathbf{k}$ and $\mathbf{m}$ changes most rapidly and that each index is more significant than the index to its right and that the i th index counts modulo M_i. The exact order used to concatenate the N dimensional matrix into the vector is immaterial as long as a convention is set and followed consistently.

With the data represented in a column vector, the forward and inverse transforms (B.5) and (B.6) can be symbolically accomplished by matrix multiplication. The transform matrix ($\hat{\mathbf{\Gamma}}$) and the inverse transform matrix ($\hat{\mathbf{\Gamma}}^{-1}$) will always be two dimensional matrices regardless of the number N. Thus

$$\hat{\mathbf{Y}}_n = \hat{\mathcal{F}}(\mathbf{y}_n) = \hat{\mathbf{\Gamma}}\hat{\mathbf{y}}_n \tag{B.9}$$

and

$$\hat{\mathbf{x}}_n = \hat{\mathcal{F}}^{-1}(\mathbf{X}_n) = \hat{\mathbf{\Gamma}}^{-1}\hat{\mathbf{X}}_n \tag{B.10}$$

where $\hat{\mathcal{F}}$ indicates Fourier transformation followed by concatenation. The transform and inverse transform matrices are

$$\hat{\mathbf{\Gamma}} = [\gamma_{\mathbf{mk}}] \tag{B.11}$$

$$\hat{\mathbf{\Gamma}}^{-1} = \left[\gamma_{\mathbf{km}}^{-1}\right] \tag{B.12}$$

and the terms $\gamma_{\mathbf{mk}}$ and $\gamma_{\mathbf{km}}^{-1}$ can be found directly by inspection of (B.5) and (B.6)

$$\gamma_{\mathbf{mk}} = \exp\frac{2\pi}{j}\left[m_1\frac{k_1}{M_1} + ... + m_N\frac{k_N}{M_N}\right]$$

$$\gamma_{\mathbf{km}}^{-1} = \frac{1}{|\mathbf{M}|}\exp 2\pi j\left[k_1\frac{m_1}{M_1} + ... + k_N\frac{m_N}{M_N}\right]$$

Using the chain rule

$$\frac{\partial\hat{\mathbf{Y}}_n}{\partial\hat{\mathbf{X}}_n} = \frac{\partial\hat{\mathbf{Y}}_n}{\partial\hat{\mathbf{y}}_n}\left(\frac{\partial\hat{\mathbf{y}}}{\partial\hat{\mathbf{X}}}\right)_n = \frac{\partial\hat{\mathbf{Y}}_n}{\partial\hat{\mathbf{y}}_n}\left(\frac{\partial\hat{\mathbf{y}}}{\partial\hat{\mathbf{x}}}\frac{\partial\hat{\mathbf{x}}}{\partial\hat{\mathbf{X}}}\right)_n \tag{B.13}$$

and noting that the forward and inverse transform matrices are constants, we have

$$\frac{\partial\hat{\mathbf{Y}}_n}{\partial\hat{\mathbf{y}}_n} = \frac{\partial\hat{\mathbf{\Gamma}}\hat{\mathbf{y}}_n}{\partial\hat{\mathbf{y}}_n} = \hat{\mathbf{\Gamma}}\frac{\partial\hat{\mathbf{y}}_n}{\partial\hat{\mathbf{y}}_n} = \hat{\mathbf{\Gamma}}\mathbf{I} = \hat{\mathbf{\Gamma}} \tag{B.14}$$

where $\mathbf{I}$ is the identity matrix. Similarly

$$\frac{\partial\hat{\mathbf{x}}_n}{\partial\hat{\mathbf{X}}_n} = \hat{\mathbf{\Gamma}}^{-1} \tag{B.15}$$

If we define $\hat{\beta}_n = [\beta_{\mathbf{pm}}]_n = \hat{\mathbf{g}}_n\hat{\mathbf{\Gamma}}^{-1}$, the operation $\hat{\mathbf{\Gamma}}\hat{\beta}_n$ in (B.13) is nothing more than the Fourier transform of $\hat{\beta}_n$ and the NFFT can be used to efficiently accomplish

the transform. We note that a single column, $\hat{\beta}_{\mathbf{m},n}$, of the two dimensional matrix $\hat{\beta}_n$, is of the same size as the data vector $\hat{\mathbf{y}}_n$. So the premultiplication of $\hat{\beta}_{\mathbf{m},n}$ by $\hat{\mathbf{\Gamma}}$ in (B.13) corresponds exactly to the operation in (B.3), and the same transform and data structure used for the circuit variables can be used in determining the frequency domain derivatives. Thus (B.13) is accomplished for the $\mathbf{m}$ th frequency of $\mathbf{X}_n$ by use of the transform operator

$$\frac{\partial \mathbf{Y}_n}{\partial X_{\mathbf{m},n}} = \left[\frac{\partial Y_{\mathbf{p}}}{\partial X}\right]_n = \mathcal{F}\left(\beta_{\mathbf{m}}\right)_n \tag{B.16}$$

where $\partial \mathbf{Y}_n / \partial X_{\mathbf{m},n}$ is an N dimensional matrix from which the elements of the Jacobian can be extracted. Again, the matrix $\beta_{\mathbf{m},n}$ (and thus $\partial \mathbf{Y}_n / \partial X_{\mathbf{m},n}$) is the same size as the data matrices $\mathbf{x}_n$, $\mathbf{X}_n$, $\mathbf{y}_n$, and $\mathbf{Y}_n$.

When Newton's method is accomplished using strictly real quantities, the following four quantities must be computed

$$^{RR}\mathbf{j}_{\mathbf{m},n} = \frac{\partial \mathrm{Re}\left(\mathbf{Y}_n\right)}{\partial \mathrm{Re}\left(X_{\mathbf{m},n}\right)} \tag{B.17}$$

$$^{RI}\mathbf{j}_{\mathbf{m},n} = \frac{\partial \mathrm{Re}\left(\mathbf{Y}_n\right)}{\partial \mathrm{Im}\left(X_{\mathbf{m},n}\right)} \tag{B.18}$$

$$^{IR}\mathbf{j}_{\mathbf{m},n} = \frac{\partial \mathrm{Im}\left(\mathbf{Y}_n\right)}{\partial \mathrm{Re}\left(X_{\mathbf{m},n}\right)} \tag{B.19}$$

$$^{II}\mathbf{j}_{\mathbf{m},n} = \frac{\partial \mathrm{Im}\left(\mathbf{Y}_n\right)}{\partial \mathrm{Im}\left(X_{\mathbf{m},n}\right)} \tag{B.20}$$

but the procedure (B.16) produces the quantity

$$\mathcal{F}\left(\beta_{\mathbf{m},n}\right) = {}^{RR}\,\mathbf{j}_{\mathbf{m},n} + {}^{II}\,\mathbf{j}_{\mathbf{m},n} + j\left({}^{RI}\mathbf{j}_{\mathbf{m},n} + {}^{IR}\,\mathbf{j}_{\mathbf{m},n}\right) \tag{B.21}$$

and the individual components cannot be recovered. We form ${}^{R}\beta_{\mathbf{m},n} = \mathrm{Re}\left(\beta_{\mathbf{m},n}\right)$ and ${}^{I}\beta_{\mathbf{m},n} = \mathrm{Im}\left(\beta_{\mathbf{m},n}\right)$ as

$${}^{R}\beta_{\mathbf{m},n} = \mathbf{g}_n \mathrm{Re}\left(\mathbf{\Gamma}_{\mathbf{m}}^{-\mathbf{1}}\right) \tag{B.22}$$

and

$${}^{I}\beta_{\mathbf{m},n} = \mathbf{g}_n \mathrm{Im}\left(\mathbf{\Gamma}_{\mathbf{m}}^{-\mathbf{1}}\right) \tag{B.23}$$

Then following (B.16) we get

$$\mathcal{F}\left({}^{R}\beta_{\mathbf{m},n}\right) = {}^{RR}\mathbf{j}_{\mathbf{m},n} + j\,{}^{IR}\mathbf{j}_{\mathbf{m},n} \tag{B.24}$$

$$\mathcal{F}\left({}^{I}\beta_{\mathbf{m},n}\right) = {}^{RI}\mathbf{j}_{\mathbf{m},n} + j\,{}^{II}\mathbf{j}_{\mathbf{m},n} \tag{B.25}$$

from which the needed derivatives are available.

B.5 Discussion and Conclusion

Equations (B.24) and (B.25) can be efficiently implemented in a circuit simulator since no matrix multiplications are required. The operations in (B.22) and (B.23) are *scalar* multiplications. This results from the fact that the nonlinear constitutive relations are algebraic ($\hat{\mathbf{g}}_n = \partial\hat{\mathbf{y}}_n/\partial\hat{\mathbf{x}}_n$ is a diagonal two-dimensional matrix). The $\gamma^{-1}_{\mathbf{km}}$ are constants and need only be computed once per simulation. However, the values of $\mathbf{g}_n$ are dependent on the nonlinear constitutive relations and so they change from iteration to iteration. For each iteration they are computed once and are then used in determining all the $\beta_{\mathbf{m},n}$ in β_n. The major operation is the multidimensional Fourier transform which is performed once at each frequency of $\mathbf{X}_n$.

The method presented for evaluating the Jacobian permits use of the efficient NFFT algorithm in conjunction with Newton's method for the harmonic balance analysis of nonlinear analog circuits. This procedure has been implemented in FREDA, a general nonlinear circuit simulator. The MESFET amplifier circuit of Chang *et. al.* [70] was driven by two incommensurate input signals one at 0 dBm and the other at 5 dBm, and simulated using fourteen analysis frequencies. The time domain element response was oversampled [72] so that the transform contained 26 frequencies. The solution was obtained in 1.1 seconds after eleven iterations using a modified Sămanskii method on a DEC DS 3100 workstation. The equivalent simulation using a matrix multiplication based transform (APDFT) required 3.8 seconds.

Appendix C

Computational Methods

Several Mathematica programs were used for all computations in this dissertation. These programs have not been integrated into a single resonator model so computations were conducted manually. These programs are listed and are briefly described.

C.1 Spectral and Spatial Field Distribution

The modal resonant frequencies which enabled computation of figures such as 4.4 and 4.5 were calculated using the program *resonantf.m*, the function *fres* determines the resonant frequency of the { m,n,q } mode.

```
(* PROGRAM resonantf.m *)
mu0 = 4. 10^(-7) N[Pi]
eps0 = 8.854185 10^-12
clight = 1.0/Sqrt[mu0 eps0]
(* m,n = transverse mode order indicies
  q = longitudinal mode number
fx,fy = focal length for x-axis and y-axis curvature
  d = distance between plane and curved reflector
*)

fres[m_,n_,q_] := clight/(2. d) (q + (m + 0.5)/N[Pi]
  ArcTan[Sqrt[d/(2. fx -d)]] + (n + 0.5)/N[Pi]
  ArcTan[Sqrt[d/(2. fy - d)]])
```

The spatial distribution of field intensity as well as coupling coefficient for a single short antenna were determined using the program *field_profile.m*. The function *amn* determines the coupling coefficient to the *mn* th mode of a single small antenna having $\hat{\mathbf{a}}_\mathbf{x}$ polarization located at {*x,y,z*} with effective length *dx* and carrying current *i*, with resonator spacing *bigD* and operating frequency *f*.

The function *E2* computes the relative field strength at {x,y,z} of the *m,n* th mode when at frequency *f* and resonator spacing *bigD*.

```
(* PROGRAM field_profile.m *)

(* plotting of transverse (x,y) resonant field profile from
   a single current source in a plano-concave resonator
   using fixed frequency, mode number  and geometry.
   The field expressions
   are valid in the region d<z<D
```

```
*)

(* Set up Constants *)
npi = N[Pi]
ghz = 10^9
freq = 8.8 ghz
mu0 = N[4 10^-7 Pi]
eps0 = N[8.854185 10^-12]
mu = mu0
eps = eps0
clight = N[1.0/Sqrt[mu eps]]
lambda[f_] :=  clight/f
 k[f_] :=  2. N[Pi] /lambda[f]
 space =  0.620494   (* reflector separation distance *)
fx = 0.894308
fy = 0.953839  (* focal length *)
reflec = -0.9992 (* reflection coefficient due to conductor losses*)

(* include diffraction losses for a few modes *)
Rmn := reflec {{0.999928, 0.999371, 0.993656},
      {0.999377, 0.99887, 0.0000001},
      {0.994022, 0.000001, 0.000001}}

(* effective current, location and lenght of antenna *)
ip = 1.0
xp = 0.0270
yp = 0.0170
zp = 0.0019
delxp =  0.0026


nsource = 1 (* number of sources *)

(* function definitions *)

xbarsq[f_,bigD_] := N[Sqrt[(2 - bigD/fx) fx bigD] / k[f]]
ybarsq[f_,bigD_] := N[Sqrt[(2 - bigD/fy) fy bigD] / k[f]]
u[f_,bigD_,z_]   := N[z / (k[f] xbarsq[f,bigD])]
v[f_,bigD_,z_]   := N[z / (k[f] ybarsq[f,bigD])]
xz[f_,bigD_,z_]  := N[ Sqrt[xbarsq[f,bigD] ( 1 + u[f,bigD, z]^2)]]
yz[f_,bigD_,z_]  := N[Sqrt[ybarsq[f,bigD] ( 1 + v[f,bigD, z]^2)]]

(* modify Mathematica's Hermite polynomial definition to agree with
  the notation used in the dissertation.  *)
dissHermiteH[n_,arg_] := (1/Sqrt[2])^n HermiteH[n, arg / Sqrt[2]]

eplusjarg[f_,bigD_,m_,n_,x_,y_,z_]  := N[- I ( \
   k[f] z + 1/2 ( \
     u[f,bigD, z] (x/xz[f,bigD, z])^2 + v[f,bigD, z] \
     (y/yz[f,bigD, z])^2 )- (m + 1/2) ArcTan[u[f,bigD, z]] \
     - (n + 1/2) ArcTan[v[f,bigD, z]])]
```

```
eminusjarg[f_,bigD_,m_,n_,x_,y_,z_] :=  \
- eplusjarg[f,bigD, m, n, x, y, z]

erealarg[f_,bigD_,m_,n_,x_,y_,z_] := \
N[- 1/2 ( (x/xz[f,bigD, z])^2 + \
      (y/yz[f,bigD, z])^2 )]

ecommonarg[f_,bigD_,m_,n_,x_,y_,z_] := N[Sqrt[ Sqrt[ (mu / eps ) / \
   ( ((npi Factorial[m] Factorial[n]) ^2 xbarsq[f,bigD] \
   ybarsq[f,bigD]) (1 + u[f,bigD, z]^2) (1 + v[f,bigD, z]^2) ) ] ] \
  dissHermiteH[m, Sqrt[2] x / xz[f,bigD, z]] \
  dissHermiteH[n, Sqrt[2] y / yz[f,bigD, z]]]

emnPlus[f_,bigD_,m_,n_,x_,y_,z_] :=\
  N[ecommonarg[f,bigD, m, n, x, y, z] \
  Exp[ erealarg[f,bigD, m, n, x, y, z] + \
  eplusjarg[f,bigD, m, n, x, y, z]]]

emnMinus[f_,bigD_,m_,n_,x_,y_,z_] := \
      N[ecommonarg[f,bigD, m, n, x, y, z] \
 Exp[ erealarg[f,bigD, m, n, x, y, z] +  \
 eminusjarg[f,bigD, m, n, x, y, z]]]

emnPM[f_,bigD_,m_,n_,x_,y_,z_] := \
 N[-2.0 I ecommonarg[f,bigD,m,n,x,y,z]  \
Exp[ erealarg[f,bigD,m,n,x,y,z]] Sin[ I eplusjarg[f,bigD,m,n,x,y,z] ]]


(* the ratio E+/E- is ~ constant over the reflector for fixed z *)
psi[f_,bigD_,m_,n_] := N[Exp[ 2 eplusjarg[f,bigD, m, n, 0, 0,bigD] ]]

upsilon[f_,bigD_,d_,m_,n_] :=  \
N[Exp[ 2 eplusjarg[f,d, m, n, 0, 0,bigD] ]]

(* coupling coefficients, amn for a single source
   evaluate at {x,y,z}={xp,yp,zp}
   dx= effective length , i = current
 *)

amn[f_,bigD_,m_,n_,x_,y_,z_,i_,dx_] := \
N[  -0.5 i dx emnPM[f,bigD,m,n,x,y,z] /
  (1. + 1./(Rmn[[m+1,n+1]] psi[f,bigD,m,n]))]

(* fields in the range d<z<bigD  *)

oneplusepsilon[f_,bigD_,m_,n_] :=  \
N[-1./(Rmn[[m+1,n+1]] psi[f,bigD,m,n])]

E2[f_,bigD_,m_,n_,x_,y_,z_] := N[ emnMinus[f,bigD,m,n,x,y,z] -
        oneplusepsilon[f,bigD,m,n] \ emnPlus[f,bigD,m,n,x,y,z]]
```

C.2 Impedance Calculations

The following code was used to compute the two port impedance parameters for two inverted-L antennas within the cavity.

The resonant impedance matrix terms z_{pq} of Eqn. 4.12 impedance matrix term z_{pq} of Eqn. 4.12 are computed using the *C* program *hermite_2port.c*. The type complex is not defined, so all equations have been rationalized, then separated into real and imaginary parts for evaluation. These calculations can be performed using *z.m* but the *C* code allowed rapid evaluation of z_{pq} at several hundred points required for plots. The program *hermite_2port.c* reads input from a file named {hermite_parameters} and sends output to files named *data.z* and *data.f*. Input is also taken from the file *hermite_coeffs*.

```
2
2 2
0
-0.0000001
0.620494
8.5930000000
8.6030000000
0.894308
0.953839
1.0
1.0
-0.0906 0.0270
0.015   0.017
0.00254  0.00249
1.0     1.0
0.0     0.0
0.00318 0.00351


--------------------------------------------------------------------------
THIS IS THE FILE hermite_parameters, enter no text above this line
as hermite_2port.c does not parse input.
parameters appear in the following order;

nsource number of sources
nmax mmax how many modes
p which element.
R reflection coefficient of curved reflector
D reflector spacing (meters)
fmin scan start frequency (Ghz)
fmax scan stop frequency  (Ghz)
Fx focal length in x-direction (meters)
Fy focal length in y-direction (meters)
pscale scales xp, yp, zp, location of p th radiator (no units)
antennascale scales length of all antennas (no units)
```

```
xp[ii] vector of x-locations (meters)
yp[ii] vector of y-locations
zp[ii] vector of z-locations
ip_mag[ii] magnitude of the p th terminal current (amps)
ip_ang[ii] phase angle of the p th current (radians)
delxp[ii] effective length of the p th element.
```

This is the file hermite_coeffs which provides the coefficients for evaluation of the Hermite polynomials.

```
10
  1.0    0.0    0.0     0.0     0.0   0.0   0.0   0.0   0.0 0.0 0.0
  0.0    1.0    0.0     0.0     0.0   0.0   0.0   0.0   0.0 0.0 0.0
 -1.0    0.0    1.0     0.0     0.0   0.0   0.0   0.0   0.0 0.0 0.0
  0.0   -3.0    0.0     1.0     0.0   0.0   0.0   0.0   0.0 0.0 0.0
  3.0    0.0   -6.0     0.0     1.0   0.0   0.0   0.0   0.0 0.0 0.0
  0.0   15.0    0.0   -10.0     0.0   1.0   0.0   0.0   0.0 0.0 0.0
-15.0    0.0   45.0     0.0   -15.0   0.0   1.0   0.0   0.0 0.0 0.0
  0.0 -105.0    0.0   105.0     0.0 -21.0   0.0   1.0   0.0 0.0 0.0
105.0    0.0 -420.0     0.0   210.0   0.0 -28.0   0.0   1.0 0.0 0.0
  0.0  945.0    0.0 -1260.0     0.0 378.0   0.0 -36.0   0.0 1.0 0.0
-945.0   0.0 4725.0     0.0 -3150.0   0.0 630.0   0.0 -45.0 0.0 1.0
```

```
/* PROGRAM hermite_2port.c */
/* this program performs two port simulation for two small linear current
   elements radiating into a plano-concave resonator.  Input is taken from
   hermite_parameters, geometric information must be specified in this file
   for two radiators.  The output data is written as a frequency list and
   a list of Z-matrices (one for each frequency), in the files data.f and
   data.z respectively.
*/


#include <math.h>
#include <stdio.h>
/* some macro definitions to make things a little easier */
#define NPOINTS 401
#define mu    (1.25663706144E-6)
#define eps   (8.854185E-12)
#define pi    (3.14159265359)
#define sr2   (1.41421356237)
#define c_    (1.0/sqrt(mu*eps))
#define k_    (2.0*pi*f/c_)
#define Y2    (sqrt(Fy*D*(2.0 - D/Fy))/k_)
#define X2    (sqrt(Fx*D*(2.0 - D/Fx))/k_)
#define u     (z/(k_*X2))
#define v     (z/(k_*Y2))
#define xz2   (X2 * (1 + u * u))
#define yz2   (Y2 * (1 + v * v))
```

```
/* some global variables */
   double h_coeffs[11][11],xp[100], yp[100], zp[100], Fx, Fy;
   int  max_hermite_order;
   double xp[100], yp[100], zp[100], ip_mag[100],
ip_ang[100],delxp[100];

/* here is a cludge for quick results, attenuation parameters */
    double RR[3][3];
/*  provide the hermite polynomial function for order < = 10  */
main()
  {
   FILE *fopen(), *fp, *fp1;
   int ii, jj,m,n,nsource,p,nmax,mmax;
   double X, hermite(),fcommon(), beta(), zpmn_almost(), answer[4][2],
passanswer[2],x,y,z,f,D,R;
   double fmin, fmax, pscale,antennascale, zTp(),deltaf,xtmp,ytmp,ztmp,
delxptmp;

/* read in coefficients for the hermite polynomial function */
   if((fp=fopen("hermite_coeffs","r")) == NULL ) {
 printf("\t***err:input file error\n ");
         exit(0);
        }
   fscanf(fp,"%d",&max_hermite_order);

   for(ii= 0; ii <= max_hermite_order; ii++) {
    for(jj= 0; jj <= max_hermite_order; jj++)
          fscanf(fp,"%lf",&h_coeffs[ii][jj]);
    }
   fclose(fp);
/* read in the simulation parameters from a batch file
   called hermite_parameters */

  if((fp=fopen("hermite_parameters","r")) == NULL ) {
printf("\t***err:input file error\n ");
exit(0);
  }
 fscanf(fp,"%d",&nsource);
 if(nsource != 2) {
     printf("INPUT ERROR, TWO SOURCE ANTENNAS MUST BE SPECIFIED");
     exit(0);
 }
 fscanf(fp,"%d",&nmax);
 fscanf(fp,"%d",&mmax);
 fscanf(fp,"%d",&p);
 fscanf(fp,"%lf",&R);
 fscanf(fp,"%lf",&D);
 fscanf(fp,"%lf",&fmin);
 fscanf(fp,"%lf",&fmax);
 fscanf(fp,"%lf",&Fx);
 fscanf(fp,"%lf",&Fy);
```

```
 fscanf(fp,"%lf",&pscale);
 fscanf(fp,"%lf",&antennascale);
 for(ii=0; ii< nsource; ii++) fscanf(fp,"%lf",&xp[ii]);
 for(ii=0; ii< nsource; ii++) fscanf(fp,"%lf",&yp[ii]);
 for(ii=0; ii< nsource; ii++) fscanf(fp,"%lf",&zp[ii]);
 for(ii=0; ii< nsource; ii++) fscanf(fp,"%lf",&ip_mag[ii]);
 for(ii=0; ii< nsource; ii++) fscanf(fp,"%lf",&ip_ang[ii]);
 for(ii=0; ii< nsource; ii++) fscanf(fp,"%lf",&delxp[ii]);
 fclose(fp);

/* quick fix for attenuation, change later, RR[m][n] gives the effective
reflection coefficient for the mn-th mode including diffraction and
conductor losses.  The frequency range is the same as that used in the
data sets in cav1a-cav4 found in plh/paper.92/antenna/
These coefficients have been calculated on p.23 lab book#4 */
RR[0][0] =   0.999928 * R;
RR[1][0] =   0.999377 * R;
RR[0][1] =   0.999371 * R;
RR[2][0] =   0.994022 * R;
RR[0][2] =   0.993656 * R;
RR[1][1] =   0.99887  * R;


/* scale the array elements locations by pscale,  makes it easier to
   change locations scale the dipole lengths by antennascale  */
 for(ii=0; ii< nsource; ii++) {
  xp[ii] *= pscale;
  yp[ii] *= pscale;
  zp[ii] *= pscale;
  delxp[ii] *= antennascale;
 }

/*
printf(" \n \n input element# and freq, p,f:\n");
scanf("%d %lf",&p,&f);
*/
   fmax = 1.0E9 * fmax;
   fmin = 1.0E9 * fmin;
   deltaf = (fmax-fmin)/(double)NPOINTS;
   fp=fopen("data.z","w");
   fp1=fopen("data.f","w");
   fprintf(fp,"\n {");
   fprintf(fp1,"\n {");
/* here we go, calculate Z_1, Z_2,z_{11}, and z_{22} at each frequency,
   while calculating, load them into answer[][], then find
   z_{12} = Z_1 - z_11 and z_{21} = Z_2 - z_{22} and write to
   data.z in Mathematica format, a list of 2x2 matrices
*/

/* set currents equal */
   ip_mag[0] = 1.0; ip_mag[1] = 1.0;
```

```
   ip_ang[0] = 0.0; ip_ang[1] = 0.0;

   for(ii=0; ii<NPOINTS; ii++) {
      f = fmin + deltaf*(double)ii;
/* calculate Z_1, input impedance of antenna-1 with both active */
      p = 0;
      nsource = 2;
      zTp(nmax,mmax,p,nsource,D,f,R,passanswer);
      answer[0][0] = passanswer[0];
      answer[0][1] = passanswer[1];
/* calculate Z_2, input impedance of antenna-2 with both active */
      p = 1;
      zTp(nmax,mmax,p,nsource,D,f,R,passanswer);
      answer[1][0] =  passanswer[0];
      answer[1][1] =  passanswer[1];
/* calculate z_{11} */
      p = 0; nsource = 1;
      zTp(nmax,mmax,p,nsource,D,f,R,passanswer);
      answer[2][0] =  passanswer[0];
      answer[2][1] = passanswer[1];
/* calculate z_{22}, I need to move physical description of
   antenna-2 and it's location into the 1st position in the
   matrices that describe antennas
*/
      p = 1;
      xtmp = xp[0]; xp[0] = xp[1];
      ytmp = yp[0]; yp[0] = yp[1];
      ztmp = zp[0]; zp[0] = zp[1];
      delxptmp = delxp[0]; delxp[0] = delxp[1];
      zTp(nmax,mmax,p,nsource,D,f,R,passanswer);
      answer[3][0] = passanswer[0];
      answer[3][1] = passanswer[1];
/* now put the antenna description matrices back to order */
      xp[0] = xtmp;
      yp[0] = ytmp;
      zp[0] = ztmp;
      delxp[0] = delxptmp;
/* output z-matrix to data.z, frequency to data.f */

      fprintf(fp,"{ { %lf + %lf I,",answer[2][0],
answer[2][1]); /*z_{11}*/
      fprintf(fp,"%lf + %lf I},\n", answer[0][0] - answer[2][0],
answer[0][1] - answer[2][1]); /* z_{12} */
      fprintf(fp,"{%f + %f I,", answer[1][0]-answer[3][0],
answer[1][1]-answer[3][1]);  /* z_{21} */
      fprintf(fp,"%f + %f I}}", answer[3][0],answer[3][1]); /*z_{22}*/
      fprintf(fp1,"%lf ", f/1.0E9);
      if((ii%5) == 0)  fprintf(fp1,"\n  ");
      if(ii != NPOINTS-1) {
         fprintf(fp,",\n ");
         fprintf(fp1,", ");
```

```
      }
    }
 fprintf(fp,"} ");
 fprintf(fp1,"} \n");
 fclose(fp);
 fclose(fp1);
}

double zTp(nmax,mmax,p,nsource,D,f,R,answer)
int nmax,mmax,p,nsource;
double D,f,R,*answer;
{  double tmp1,tmp2,tmpA,tmpR,tmpI;
   int nn,mm;
   tmp1 = 0.0;
   tmp2 = 0.0;
   for(mm=0;mm<=mmax;mm++)
     for(nn=0;nn<=nmax;nn++) {
       zpmn_almost(mm,nn,p,nsource,D,f,R,answer);
       tmp1 += answer[0];
       tmp2 += answer[1];
     }
/* now include the delxp/(2 ip) factor   */
   tmpA = delxp[p]/(2.0*ip_mag[p]);
   tmpR = cos((double)ip_ang[p]);
   tmpI = sin((double)ip_ang[p]);
   answer[0] = tmpA*(tmp1*tmpR - tmp2*tmpI);
   answer[1] = tmpA*(tmp1*tmpI + tmp2*tmpR);
}


double hermite(n,X)
int n;
double X;
  {
     int count;
     double sum ;
  if(n > max_hermite_order) {
    printf("\n **** hermite order too high ****");
    exit(0);
   }
  sum = 0.0 ;
  for (count =0; count <= n; count++)
    sum += h_coeffs[n][count] * pow((double)X,(double)count);
  return(sum);
}
double fcommon(m,n,x,y,z,D,f)
 int m,n;
 double x,y,z,D,f;
{  double tmp1,tmp2,tmp3,tmp4,hermite();
   int FACT();
```

```
   tmp1 = 1.0/sqrt(pi*sqrt(X2*Y2*eps/mu)*FACT(m)*FACT(n));
   tmp2 = 1.0/pow((double)((1.0+u*u)*(1.0+v*v)),0.25);
   tmp3 =  hermite(m,sr2*x/sqrt(xz2))* hermite(n,sr2*y/sqrt(yz2));
   tmp4 = exp(-0.5*(x*x/xz2 + y*y/yz2));
   return(tmp1*tmp2*tmp3*tmp4);
}

double beta(m,n,x,y,z,D,f)
 int m,n;
 double x,y,z,D,f;
{ double tmp0,tmp1, tmp2;
tmp0 = fmod(k_ * z, 2.0*pi);
tmp1=  0.5*(u*x*x/xz2 + v*y*y/yz2);
tmp2 = ((double)m + 0.5)*atan((double)u) +
((double)n + 0.5)*atan((double)v);
return(tmp0 + tmp1 - tmp2);
}

double zpmn_almost(m,n,p,nsource,D,f,R,answer)
int m,n,p,nsource;
double D,f,R,*answer;
{
  double A1,A2,A3,R1,R2,R3,I1,I2,I3,
        fcommon(),beta_d,beta_p;
  int ii;
/* include diffraction losses */
beta_d = beta(m,n,0.0,0.0,D,D,f);
beta_p = beta(m,n,xp[p],yp[p],zp[p],D,f);
A1 = 1.0/(1.0 + RR[m][n]*RR[m][n] +
2.0*RR[m][n]*cos((double)(2.0*beta_d)));
A2 = fcommon(m,n,xp[p],yp[p],zp[p],D,f);
R1 = 1.0 + RR[m][n]*cos((double)2.0*beta_d);
I1 = RR[m][n]*sin((double)2.0*beta_d);
R2 = R*cos((double)(2.0*beta_d - beta_p)) + cos((double)beta_p);
I2 = -( R*sin((double)(2.0*beta_d - beta_p)) + sin((double)beta_p));
R3 = 0.0;
I3 = 0.0;
for(ii=0; ii<nsource; ii++) {
  A3 = 2.0*fcommon(m,n,xp[ii],yp[ii],zp[ii],D,f)*
    sin((double)beta(m,n,xp[ii],yp[ii],zp[ii],D,f))*delxp[ii];
  R3 += -A3*ip_mag[ii]*sin((double)ip_ang[ii]);
  I3 +=  A3*ip_mag[ii]*cos((double)ip_ang[ii]);
}
*answer = A1*A2*(-I2*I3*R1 - I1*I3*R2 - I1*I2*R3 + R1*R2*R3);
*(answer+1) = A1*A2*(-I1*I2*I3 + I3*R1*R2 + I2*R1*R3 + I1*R2*R3);
}


int  FACT(i) /* compute factorial */
int i;
{ int j;
```

```
  int prod;
   prod = 1;
   for(j=i; j>0; j--) {
     prod *= j;
   }
   return(prod);
}
```

The computation of the nonresonant portion of the two port impedance was performed by the program *greencomp.m*. The inverted-L antenna of fig. 4.8 is divided into three segments. Antenna current is assumed to be a maximum at the terminal and to taper linearly along the length of the antenna. A line integral is performed along the integral to determine the effective lengths of equivalent impulse sources. Potential theory is used to determine the induced potential at the recieving antenna. This is evaluated by the function *volt*.

```
(* PROGRAM greencomp.m *)

(* green's function calculation for z12 of two inverted-L antennas
   in resonator  see p.96 in lab book #4,
   all units are in MKS system  *)

(* h2 is the half-height of the sending antenna *)
pi = N[Pi];
p2m1 = (pi/2. - 1.)
piby4 = pi/4.;
h = 0.098 2.54/100.;  (* height of sending antenna *)
h2 = h/2.;
hr = 0.1 2.54 /100.; (* recieving antenna effective height *)
elr = .125 2.54 /100.; (* recieving antenna length *)
xr = 4.25 2.54/100.; (* location of base of recieving antenna *)
el = 0.138 2.54/100.;
(* length of sending antenna, see attachment p24 book#4 *)
mu =  4. 10^-7 N[Pi];
eps =  8.854185 10^-12;
clight = 1./Sqrt[mu eps];
k[f_] = N[2. Pi f/clight]; (* free-space wave number *)
ghz = 10.^9;
const = N[1./(4. Pi)];
(* some global distance measure definitions,
numbers represent region 1, 2,or 3.
        "i" means image charge *)
rr1[x_,z_,t_] = N[Sqrt[x^2 + (z-t)^2]]
(* distance to current source *)
rr1i[x_,z_,t_] = N[Sqrt[x^2 + (z+t)^2]]
(* distance to image current *)
rr2[x_,z_,t_]  = N[Sqrt[(x - h2 +Sqrt[t(h-t)])^2 +
(z-t)^2]] (* curved region *)
rr2i[x_,z_,t_] = N[Sqrt[(x - h2 +Sqrt[t(h-t)])^2 +
```

```
(z+t)^2]] (* curved region *)
rr3[x_,y_,t_] =  N[Sqrt[(x-t+h2)^2 + (z-h)^2]]
(* top region *)
rr3i[x_,y_,t_] =  N[Sqrt[(x-t+h2)^2 + (z+h)^2]]
(* top region *)

(* magnetic potential scalar Green's functions
   for the different regions *)

g1[x_,z_,t_,f_] = N[const Exp[-I k[f] rr1[x,z,t]]/rr1[x,z,t]];
g1i[x_,z_,t_,f_] = N[const Exp[-I k[f] rr1i[x,z,t]]/rr1i[x,z,t]];
g2[x_,z_,t_,f_] = N[const Exp[-I k[f] rr2[x,z,t]]/rr2[x,z,t]];
g2i[x_,z_,t_,f_] = N[const Exp[-I k[f] rr2i[x,z,t]]/rr2i[x,z,t]];
g3[x_,z_,t_,f_] = N[const Exp[-I k[f] rr3[x,z,t]]/rr3[x,z,t]];
g3i[x_,z_,t_,f_] = N[const Exp[-I k[f] rr3i[x,z,t]]/rr3i[x,z,t]];

(* use Block construct to evaluate the componants of the half-space
electric field Green's functions
(which also include the image current) *)

(* for lower vertical section, all z-current *)
gz1[x_,z_,t_,f_ ] = N[Block[{kk,g,gi,dz2,dz2i,ddg,ddgi,r,ri},
kk = k[f];
kk2 = kk kk;
g = N[g1[x,z,t,f]];
gi = N[g1i[x,z,t,f]];
dz2 = N[(z-t)^2.];
dz2i = N[(z+t)^2.];
r = N[rr1[x,z,t]];
ri = N[rr1i[x,z,t]];
    ddg = N[g/kk2 (3. dz2/r^4-(1.+ kk2 dz2)/r^2.+
   I (3. kk dz2/r^3.-kk/r))];
   ddgi = N[gi/kk2 (3. dz2i/ri^4-(1.+ kk2 dz2i)/ri^2.+
   I (3. kk dz2i/ri^3.-kk/ri))];
   g + gi + ddg + ddgi
   ]];

(* for the z-current componant on the curved section *)
gz2[x_,z_,t_,f_ ] = N[Block[{kk,g,gi,dz2,dz2i,ddg,ddgi,r,ri},
  kk = k[f];
  kk2 = kk kk;
   g = N[g2[x,z,t,f]];
   gi = N[g2i[x,z,t,f]];
   dz2 = N[(z-t)^2.];
   dz2i = N[(z+t)^2.];
   r = N[rr2[x,z,t]];
   ri = N[rr2i[x,z,t]];
 ddg = N[g/kk2 (3. dz2/r^4-(1.+ kk2 dz2)/r^2.+
       I (3. kk dz2/r^3.-kk/r))];
 ddgi = N[gi/kk2 (3. dz2i/ri^4-(1.+ kk2 dz2i)/ri^2.+
I (3. kk dz2i/ri^3.-kk/ri))];
```

```
 g + gi + ddg + ddgi
 ]];

(* for the x-current componant of the curved section *)
gx2[x_,z_,t_,f_] = N[Block[{kk,g,gi,dx2,dx2i,ddg,ddgi,r,ri},
  kk = k[f];
  kk2 = kk kk;
   g = N[g2[x,z,t,f]];
   gi = N[g2i[x,z,t,f]];
   dx2 = N[(x-h2+Sqrt[t (h-t)])^2.];
   dx2i = dx2;
   r = N[rr2[x,z,t]];
   ri = N[rr2i[x,z,t]];
 ddg = N[g/kk2 (3. dx2/r^4-(1.+ kk2 dx2)/r^2.+
       I (3. kk dx2/r^3.-kk/r))];
 ddgi = N[gi/kk2 (3. dx2i/ri^4-(1.+ kk2 dx2i)/ri^2.+
I (3. kk dx2i/ri^3.-kk/ri))];
 g - gi + ddg - ddgi (* minus sign for opposite current direction *)
 ]];


(* for the x-current (total) componant of the horizontal top section *)
gx3[x_,z_,t_,f_] = N[Block[{kk,g,gi,dx,dxi,ddg,ddgi,r,ri},
  kk = k[f];
  kk2 = kk kk;
   g = N[g3[x,z,t,f]];
   gi = N[g3i[x,z,t,f]];
   dx2 = N[(x-t+h2)^2.];
   dx2i = dx2;
   r = N[rr2[x,z,t]];
   ri = N[rr2i[x,z,t]];
 ddg = N[g/kk2 (3. dx2/r^4-(1.+ kk2 dx2)/r^2.+
       I (3. kk dx2/r^3.-kk/r))];
 ddgi = N[gi/kk2 (3. dx2i/ri^4-(1.+ kk2 dx2i)/ri^2.+
I (3. kk dx2i/ri^3.-kk/ri))];
 g - gi + ddg - ddgi (* minus sign for opposite image current direction *)
 ]];


(* now we need the parameterized componants of the vector current,
  see p89 of lab-book #4 *)

amp = 1.; (* source current amplitude *)

iz1[t_] = amp N[1.- t/(el +  h piby4)];
imag2[t_] = amp N[1. - h2 (1.+
    ArcTan[(t-h2)/Sqrt[t (h-t)]])/(el +  h piby4) ] ;
iz2[t_] = amp N[ 2./h Sqrt[t (h-t)]] imag2[t];
ix2[t_] = amp N[ (2. t/h - 1.)] imag2[t];
ix3[t_] = amp N[1. - (h2 p2m1 + t)/(el + h piby4)];
```

```
(* to integrate, we need differential path lengths
   for the three intervals *)

ds1 = 1.;
ds2[t_] = N[Sqrt[1. + (h2 - 1. t)^2./(t (h - t))]];
ds3 = 1.;


(* approximation for the electric field assuming the source to be one
   x-directed point source at {x=h/2, z=h} (along with it's image),
   and one z-directed point current source at (x=0,z=0).
   The strengths of the impulse sources are found by integrating
   the assumed current density over the source antenna, then
   finding the x and z componants.
*)

Ex[x_,z_,f_] = N[2. Pi f mu I 0.001145 gx3[x,z,h,f]];

Ez[x_,z_,f_] = N[2. Pi f mu I 0.0019 gz1[x,z,0,f]];


(* terminal voltage on antenna#2, using definition of voltage from
   p.102 of lab book#4.
*)
volt[f_] := N[( Pi f mu I)
    (0.001145 NIntegrate[gx3[x,hr,h,f],{x,xr,xr+elr}] +
            0.0019 NIntegrate[gz1[xr,z,0,f],{z,0,hr}])];
```

Experiments were conducted over fairly narrow frequency ranges. It can be shown that resonator modal diffraction losses and reflector conductor losses are almost constant over these narrow frequency ranges. Diffraction losses for each mode were assumed to be constant and were calculated using the program *truefields.m*. The function *eigenproblem* loads a complex matrix corresponding to Huygens principle applied to a two dimensonal resonator. Results are stored in *evalues* which are related to diffraction losses and *evectors* which give the modal field profiles. Results for a three dimensional resonator are obtained as the product of the results for two two-dimensional simulations as indicated in section 3.2.

```
(* PROGRAM truefields.m *)

(* mathematica file to solve the eigenproblem corresponding to fields
   diffraction losses and mode structure in a two dimensional  open
   resonator composed of two identical  reflectors with;

radius of curvature = b  (meters)
separation distance = d  (meters)
total aperture width = 2 a (meters)
operating at frequency = f (GHz)
```

```
  problem is solved by sampling the field at npts  discreet points,
  the integral equation then becomes a matrix eigenproblem.

number of sample pts = npts (must be an odd integer)
*)
 mu = (1.25664 10^-6)
 eps = (8.85418 10^-12)
 pi = (3.14159265359)
 srpi = N[Sqrt[pi]]
 sr2 = (1.41421356237)
 clight = N[1.0/Sqrt[mu*eps]]
 k[f_] = N[2. pi f/clight]
 ghz = 10^9

 eplot[i_] := ListPlot[evectors[[i]],PlotJoined -> True];
eigenproblem[npts_, f_, a_, b_, d_] :=
Block[{sqrtc, h, scale, argconst,tmp,i,j},
sqrtc = N[Sqrt[k[f ghz] a a/d]];
h = N[2. sqrtc/(npts-1)];
scale = N[h/(sr2 srpi)];
argconst = N[(d - b)/(2. b)];
X[i_] := N[-sqrtc + i h];
          arg[i_,j_] := N[X[i] X[j] +  \
   argconst (X[i]^2. + X[j]^2.)];
simpson[i_] := N[ 2./3. (1. + Mod[i,2])];
(* load the comples matrix... *)
cmatrix = Table[N[simpson[j]
                  Exp[I arg[i,j]]],{i,0,npts-1},{j,0,npts-1}];
(* fix up the end point Simpson's rule coefficients *)
For[j=1,j<npts+1,j++,
   cmatrix[[j,1]] = cmatrix[[j,1]]/2. ;
   cmatrix[[j,npts]] = cmatrix[[j,npts]]/2.  ;
        ];

        evalues = Abs[scale Eigenvalues[cmatrix]];
evectors = Abs[Eigenvectors[cmatrix]];
(* sort the evalues and evectors in order of decresing evalues *)
tmp = Table[Flatten[{evalues[[i]],evectors[[i]]}],{i,1,npts}];
tmp = Reverse[Sort[tmp]];
evectors = Table[Drop[tmp[[i]],1],{i,1,npts}];
evalues = Reverse[Sort[evalues]];
]
```

C.3 Data Manipulation

Many small programs were used to manipulate measured and simulated data. Two that were used often are *deembed.m* which removed the effect of the shunt discontinuity capacitances C_{D1} and C_{D2} from measured 2-port data, and *embed2port.m*

which embeds the two port simulated impedances as shown in Fig. 4.7.

```
(* PROGRAM deembed.m *)
(* 16 Dec. 92 (p.104 lab book 4) De-embed 2port cavity impedance data
   by removing shunt capacitors at the input and output.
*)
Print["READING AND FORMATTING DATA"]
(* read in HP8510 data, denormalize, put in arrays {freq,Zxx} *)
n2pi = N[2 Pi];
zcav = ReadList["/u0/users/MBS/plheron/paper.92/antenna/cav3_2port",
{Number,Number,Number,Number,Number,Number, Number,Number,Number}];
numpts = 401;
ghz = 10.^9.
   c11 = Table[{zcav[[i,1]]/ghz, 50.0 (zcav[[i,2]] + I zcav[[i,3]])},
         {i,1,numpts}];
(*
max =  Max[Abs[Part[Transpose[c11],2]]];
min = Min[Abs[Part[Transpose[c11],2]]];
ListPlot[Abs[c11], PlotRange->{min,max},
  PlotLabel->"|c11|"];
*)
   c12 = Table[{zcav[[i,1]]/ghz, 50.0 (zcav[[i,4]] + I zcav[[i,5]])},
       {i,1,numpts}];
(*
max = Max[Abs[Part[Transpose[c12],2]]];
min = Min[Abs[Part[Transpose[c12],2]]];
ListPlot[Abs[c12],PlotRange->{min,max},
  PlotLabel->"|c12|"];
  c21 = Table[{zcav[[i,1]]/ghz , 50.0 (zcav[[i,6]] + I zcav[[i,7]])},
         {i,1,numpts}];
*)

   c22 = Table[{zcav[[i,1]]/ghz, 50.0 (zcav[[i,8]] + I zcav[[i,9]])},
         {i,1,numpts}];
(*
max = Max[Abs[Part[Transpose[c22],2]]];
min = Min[Abs[Part[Transpose[c22],2]]];
ListPlot[Abs[c22], PlotRange->{min,max},
  PlotLabel->"|c22|"];
*)

zcav = .

(*
   it is easier to de-embed shunt capacitive reactance using
   admittance parameters, convert to admittance, de-embed, then
   transfrom back to z-parameters.
*)
Print["ALLOCATING SPACE FOR DE-EMBEDDED VARIABLES"]
(* allocate room for the de-embedded data *)
z11d = Table[{0,0}, {i,1,numpts}];
```

```
z22d = Table[{0,0}, {i,1,numpts}];
z12d = Table[{0,0}, {i,1,numpts}];
c1 = n2pi ghz 2.0  10.^(-14.);
c2 = n2pi ghz 2.0 10.^(-14.);
Print["PERFORMING DE-EMBED"]
For[i=1,i<numpts+1,i++,
   zdet = c11[[i,2]] c22[[i,2]] - c12[[i,2]]^2;
   freq = c11[[i,1]];
   y11 = c22[[i,2]]/zdet - I c1 freq;
   y12 = -c12[[i,2]]/zdet;
   y22 = c11[[i,2]]/zdet - I c2 freq;
   ydet = (y11 y22 - y12 y12);
   z11d[[i,1]] = freq;
   z12d[[i,1]] = freq;
   z22d[[i,1]] = freq;
   z11d[[i,2]] = y22/ydet;
   z12d[[i,2]] = -y12/ydet;
   z22d[[1,2]] = y11/ydet;
   ]


(* PROGRAM embed2port.m *)
(* embed the reciprocal cavity z-matrix by placing
   antenna circuit model at the input and output ports.
   Circuit values come from optimization
   of measured data.  see lab book#4 p40-41.
*)
Print["LOADING SIMULATION DATA"]
freq = << "data.f";
zdat = << "data.z";

numpts = 401;
n2pi = 2. N[Pi];
ghz = 10.^9.

Printf["DEFINING VARIABLES"]

R1 = 23.780;
L1 = n2pi ghz 8.103  10.^(-10.);
C1 = n2pi ghz 7.14606  10.^(-14.);
Cs1 = n2pi ghz 9.91535  10.^-(14.);

R2 = 21.857;
L2 = n2pi ghz 8.437 10.^(-10.);
C2 = n2pi ghz 7.66331 10.^(-14.);
Cs2 = n2pi ghz 9.10366 10.^(-14.);

zcs1[ii_] := N[-I/(freq[[ii]] Cs1)];
zcs2[ii_] := N[-I/(freq[[ii]] Cs2)];
z1[ii_] :=   N[R1 + I (freq[[ii]] L1 - 1./(freq[[ii]] C1)) +
zdat[[ii,1,1]] - zdat[[ii,1,2]] ];
```

```
zp1[ii_] := N[zdat[[ii,1,2]] (z1[ii] + zcs1[ii])/
           (zdat[[ii,1,2]] + z1[ii] + zcs1[ii])];

z2[ii_] := N[R2 + I (freq[[ii]] L2 - 1./(freq[[ii]] C2)) +
zdat[[ii,2,2]] - zdat[[ii,1,2]] ];
zp2[ii_] := N[ zdat[[ii,1,2]] (z2[ii] + zcs2[ii])/
           (zdat[[ii,1,2]] + z2[ii] + zcs2[ii])];

Print["EMBEDDING Z-MATRIX"]

z11e = Table[{freq[[i]],N[(zp2[i]+z1[i]) zcs1[i]/(zp2[i]+z1[i]+zcs1[i])]},
       {i,1,numpts}];

z22e = Table[{freq[[i]],N[(zp1[i]+z2[i]) zcs2[i]/(zp1[i]+z2[i]+zcs2[i])]},
       {i,1,numpts}];

z12e = Table[{freq[[i]],N[zcs1[i] zdat[[i,1,2]] zcs2[i]/
((zcs2[i]+z2[i]+zp2[i]) (zdat[[i,1,2]]+z1[i]+zcs1[i]))]},
      {i,1,401}];
Print["SCALING AND GRAPHING RESULTS"]
max = Max[Abs[Part[Transpose[z11e],2]]];
min = Min[Abs[Part[Transpose[z11e],2]]];
ListPlot[Abs[z11e],PlotLabel->"z11e",PlotRange->{min,max},PlotJoined->True];
max = Max[Abs[Part[Transpose[z12e],2]]];
min = Min[Abs[Part[Transpose[z12e],2]]];
ListPlot[Abs[z12e],PlotLabel->"z12e",PlotRange->{min,max},PlotJoined->True];
max = Max[Abs[Part[Transpose[z22e],2]]];
min = Min[Abs[Part[Transpose[z22e],2]]];
ListPlot[Abs[z22e],PlotLabel->"z22e",PlotRange->{min,max},PlotJoined->True];
```